VILNIUS UNIVERSITY

CENTER FOR PHYSICAL SCIENCES AND TECHNOLOGY

IEVA BALEVIČIŪTĖ

SPECTROSCOPIC ELLIPSOMETRY OF MULTILAYER NANOSTRUCTURES USED IN BIOSENSORS APPLICATIONS

Doctoral dissertation

Physical sciences, Chemistry (03 P)

Vilnius, 2014

Doctoral dissertation was prepared at Vilnius University, Faculty of Chemistry from 2010 to 2014.

Scientific supervisor:

Prof. Dr. Habil. Arūnas Ramanavičius (Vilnius University, physical sciences, chemistry – 03P).

VILNIAUS UNIVERSITETAS
FIZINIŲ IR TECHNOLOGIJOS MOKSLŲ CENTRAS

IEVA BALEVIČIŪTĖ

DAUGIASLUOKSNIŲ NANODARINIŲ BIOJUTIKLIAMS SPEKTROSKOPINĖ ELIPSOMETRIJA

Daktaro disertacija

Fiziniai mokslai, Chemija (03 P)

Vilnius, 2014

Disertacija parengta 2010 – 2014 metais Vilniaus universitete, Chemijos fakultete.

Mokslinis vadovas:

Prof. habil. dr. Arūnas Ramanavičius (Vilniaus universitetas, fiziniai mokslai, chemija – 03P)

ACKNOWLEDGMENTS

I would like to express my gratitude to Vilnius University, Faculty of Chemistry and the head of Department of Physical Chemistry, my supervisor Prof. Dr. Habil. Arūnas Ramanavičius, for giving me the possibility to do this work, for suggestion of interesting topic, his guidance and support during all dissertation preparing period.

I'm very thankful for assoc. prof. Dr. Almira Ramanavičienė, PhD student Asta Makaravičiūtė, dr. Arūnas Stirkė, Ms. Student Linas Tamošaitis for helping and support during preparation of proteins based biological monolayers.

I would like to thank Dr. Roman Viter from Odessa Mechnikov University (Ukraine) and Dr. Mikhael Bechelany from Institut Europeen des Membranes, Montpellier (France) for manufacturing of nanolaminates structures.

I'm great thankful for my family members for understanding and encouragement during all this years, especially for my father Prof. Dr. Habil. Saulius Balevičius for consulting of mathematical models applications and my brother assoc. prof. Dr. Zigmas Balevičius for helpful discussion and teaching about ellipsometry.

CONTENTS

Abreviations

AGID − agar gel immune-diffusion

AFM − atomic force microscopy

ALD − atomic layer deposition

BLV − bovine leukaemia virus

CTO − transparent conducting oxide films

DEZ − diethyl zinc

dGCSF − dimeric granulocyte colony stimulating factor

DLE − deep level emission

EBL − enzootic bovine leucosis

EDC − N-(3-dimethylaminopropyl)-N′-ethylcarbodiimide hydrochloride

EDX − energy dispersive X-ray spectroscopy

ELISA − enzyme linked immune sorbent assay

EMA − effective medium approximation

EIS − electrochemical impedance spectroscopy

FED − flexible electronic devices

frag-Ab − fragmented antibody

GCSF-R − granulocyte colony stimulating factor receptor

GIXRD − grazing incidence X-ray diffraction

HRP − horseradish peroxidase

HSA − human serum albumin

mGCSF − monomeric granulocyte colony stimulating factor

MIP − molecularly imprinted polymer

NBE − near band edge emission

NHS − N-Hydroxysuccinimide

intact-Ab − non fragmented antibody

PBS − phosphate buffer saline

PL − photoluminescence

Ppy − polypyrrole

QCM − quartz crystal microbalance

QD − quantum dot

RMS − root mean square

SAM − self- assembled monolayer

SE− spectroscopic ellipsometry

SEM − scanning electron microscopy

SPR − surface plasmon resonance

TC − texture coefficients

TIRE − total internal reflection ellipsometry

TMA − trimethylaluminum

VASE − variable angle spectroscopic ellipsometry

11-MUA − 11-Mercaptoundecanoic acid

Introduction
Preface

Ellipsometry is a conventional optical technique which measures changes in light polarization states. The spectroscopic ellipsometry (SE) makes it possible to obtain in ultra violet/visible region the bandgap (*direct and indirect transitions*), surface temperature, alloy composition, phase structure (crystal, amorphous, void) and grain size. In infrared region the charge carrier concentration, mobility, lattice vibration modes (*longitudial and transverse optical phonons*) and local structures (*such as Si–H, –OH*) of the material can be measured using this method. For this reason it is widely used for the investigation of dielectric function of thin films or multi-layered structures prepared from III–V, II–VI semiconductors, insulators and metals.

An exclusive feature of ellipsometric method is that largest changes in polarization state appear when light passes through the interface between medias having different optical properties. For this reason the ellipsometry can be used for sensing of nanometric thickness layers of biomolecules adsorbed on the surface of various materials. This technology allows highly sensitive detection of target biomolecules and is alternative to the existing chemical and biological detection schemes. It has sub-nanometer resolution for thickness determination (< 0.01 nm) and is able to detect very small concentration (1 ng/ml) of biomaterial markers. It is non-contact and not-destructive method and in contrary to the widely used atomic force microscopy or surface-enhanced laser desorption/ionization methods significantly decreases the effect of bioactivity.

In total internal reflection mode the ellipsometry can be used for *in-situ* sensing of nanometer size monomolecular layer formation process. For this purpose the real-time spectroscopic ellipsometry which starts in 1984 when Muller and Farmer [1] applied it for electrochemical studies is necessary. This technique makes it possible to obtain the full spectra of ellipsometric parameters Δ and Ψ consisting of 400 points from 410 nm to 700 nm in approximately 3 s. Sopra RTSE [2] having a rotating polarizer SE with a prism spectrometer/CCD array detector for high speed data acquisition allows data collection at a 1.8 s sampling rate. Modern J.A. Woollam Co. Spectroscopic ellipsometer M-2000 and Complete EASE software is able to collect data in the range of wavelenght from 193 nm to 1690 nm in time less than 1s. This opens new possibilities to measure with high accuracy the kinetics of biosensing process and to determine the kinetic coefficients of adsorption and surface dynamics of organic molecules, especially of proteins. The determination of these coefficients is very important because it gives possibility to characterize biomaterial layer not only by thickness and optical properties, but also by ability to interact with other organic and inorganic materials. However, the direct result of ellipsometry method is measurement of ellipsometric parameters Δ and Ψ which contains information about phase and amplitude of the reflected or transmitted light respectively. For quantitative evaluation the subsequent analysis of these parameters is necessary in order to obtain refractive index (n) and thickness (d) of the layer which could depend on layer reorganization process, density effects, molecular orientation, clustering, multilayering and various combinations of these phenomena [3]. The „decoding“of information stored in Δ and Ψ to the optical and structural parameters of the layer is performed by modelling procedure which usually is unique for different materials and structures. For this reason one of the objectives of the present thesis was to develop spectroscopic ellipsometry method for the investigation of protein-protein interaction using a models: (i) the interaction of Bovine leukaemia virus (BLV) surface glycoprotein *gp*51, which was acting as antigen with antibody and (ii) monomeric or dimeric granulocyte colony stimulating factor (GCSF) interaction with its receptor. The BLV is related to human leukaemia virus type and interaction of BLV surface *gp*51 antigen with antibody can served for study of oncological viruses and the development of vaccine against retroviruses. The choose of investigation of monomeric and dimeric GCSF interaction with its receptor was stimulated by the possibility to evaluate how spectroscopic ellipsometry method can be used for recognition of similar biomolecules having different structure and mass. That is very important for the development of selective biosensors.

The other type of thin film biosensors used for the rapid immunoassay detection is based on the appearance of a colour change when a specific biologic agent is present [4,5]. The detector is a substrate coated with an interference layer that reflects a particular colour. The reaction between antigen and specific antibody causes the precipitation of a layer whose optical thickness optically interferes with the thin film coating to cause the colour shift [6]. The interference layer has to satisfy optical performance criteria to generate interference patterns i.e. necessary effective refractive index and thickness. Very atractive way to design such layers is to use nanolaminates prepared by atomic layer deposition method. A key task here is to determine optical parameters of single layers and multi layered structures. The investigation of possibilities of spectroscopic ellipsometry method for this purpose was the other objective of the present thesis.

Objectives

The objectives of these efforts are to develop spectroscopic ellipsometry method for the investigation of optical properties: (i) of multi-layered nanostructures used for Bovine leukaemia virus glycoprotein *gp*51 (antigen) recognition, (ii) nanostructures consisting of monomeric (mGCSF) or dimeric (dGCSF) granulocyte colony stimulating factor and its receptor (GCSF-R) and (iii) Al_2O_3/ZnO nanolaminates designed by atomic layer deposition method. In particular, focusing on the investigation of:

- biological recognition layers of immunosensors by means of comparison of analytical sensitivities of ellipsometric parameters Δ and Ψ in order to estimate differences in orientation of immobilized intact and fragmented antibodies;
- the kinetics of biosensing layer formation, which was based on the immobilization of fragmented and intact antibodies, kinetics of antigen interaction with the immobilized antibodies and interactions of monomeric

(mGCSF) and dimeric (dGCSF) granulocyte colony stimulating factor and its receptor (GCSF-R) immobilized on a thin gold layer;

- kinetic coefficients of monomolecular biological layer formation process using model which takes into consideration partial reversibility (residence time) effect;
- optical constants of Al_2O_3 and ZnO monolayer as well as Al_2O_3/ZnO nanolaminates prepared by atomic layer deposition method in order to investigate possibilities to apply these nanolaminates for optical biosensors.

The goals of these efforts were the following:

1. to use total internal reflection ellipsometry (TIRE) technique for the investigation of biological recognition layers of immunosensors in order to estimate the orientation of immobilized intact and fragmented antibodies;
2. to compare analytical sensitivities of the Δ and Ψ parameters of TIRE in order choose which parameter is preferable to resolve differences in nanostructures of intact-Ab and frag-Ab layers;
3. using TIRE method to investigate the kinetics of biosensing layer formation, which was based on the Bovine leukemia virus glycoprotein *gp*51 (antigen) and specimen enriched with specifically interacting fragmented and intact antibodies;
4. to evaluate the sensitivity of Δ and Ψ parameters during different stages of biological monolayer formation process and to analyse kinetics of this monolayer formation using a model, which took into account partial reversibility of analyte;
5. to investigate the possibilities of spectroscopic TIRE method in its dynamic data acquisition mode for the *in-situ* study of the interactions of monomeric (mGCSF) and dimeric (dGCSF) granulocyte colony stimulating factor and its receptor (GCSF-R), which was immobilized on a thin gold layer;
6. to analyse the possibilities of spectroscopic dynamic TIRE data to detect small differences in association and dissociation times of monomeric (mGCSF) and

dimeric (dGCSF) granulocyte colony stimulating factor and its receptor (GCSF-R) through the precise determination of the refractive index dispersion;

7. using TIRE spectroscopy method to study optical constants for Al_2O_3 and ZnO monolayer in order to investigate the possibilities to tune optical and structural properties of Al_2O_3/ZnO nanolaminates designed by atomic layer deposition method (ALD).

Novelties of this effort are:

1. Demonstration that advandages of analytical sensitivity of the ellipsometric parameter Δ obtained from total internal reflection ellipsometry method enables to resolve differences in orientation of nanostructures of immobilized intact and fragmented antibodies.
2. Development of a new method based on single wavelength total internal reflection ellipsometry, which takes into consideration nonlinear change of Δ and Ψ parameters during various stages of biological layer formation process, was suggested for the analysis of antibody-antigen adsorption interaction kinetics.
3. Demonstration that spectroscopic total internal reflection ellipsometry in its dynamic data acquisition mode allows to study *in-situ* of the interactions of monomeric (mGCSF) and dimeric (dGCSF) granulocyte colony stimulating factor and its receptor (GCSF-R) and to detect small differences in kinetic coefficients through the precise determination of the refractive index dispersion.
4. The discover that during the synthesis ZnO single layer in the nanolaminates was not doped by Al and that it diffused into the interface of ZnO/Al_2O_3 bilayer, forming defect states which increased visible band of PL. Blue shift of band gap and excitonic peak position of ZnO single layers can be explained by quantum confinement effect and the improvement of crystalline quality of ZnO layer.

Statements to be defended

1. The total internal reflection spectroscopic ellipsometry enables to resolve differences in nanostructures of intact and fragmented *gp*51 antibodies layers used for Bovine leukemia virus protein *gp*51 sensing. The analytical sensitivity of the ellipsometric parameter Δ is significantly (5.89 times) better if compared to the sensitivity of the Ψ parameter, which is in fact similar to the sensitivity of surface plasmon resonance based immunosensors.
2. The ellipsometric parameter Δ shows much higher sensitivity at the initial phase of protein monolayer formation process, while the parameter Ψ is more sensitive at the final stage of biological layer formation. The immobilization rate of *gp*51 antibody layer formation is similar for both intact and fragmented antibodies. However, the residence time differs and is 25 times longer in case of intact antibody. In contrary, for antigen interaction with immobilized antibodies this time is about 8 times longer when in case of fragmented antibodies.
3. Total internal reflection ellipsometry in spectroscopic dynamic acquisition mode is able to reveal small differences in association and dissociation times of the interaction of monomeric and dimeric granulocyte colony stimulating factor and its receptor, which was immobilized on a thin gold layer. It can be achieved through the precise determination of the refractive index dispersion and elimination of signal non-linearity using regression analysis of spectroscopic ellipsometry data.
4. The optical properties of ZnO/Al_2O_3 nanolaminates prepared by atomic layer deposition method in which thickness of single layers is no less than 10 nm can be determined using regression analysis of ellipsometric response where the ZnO layer is characterized by one Psemi-MO and two Gausian oscillators and the Cauchy dispersion function is used for Al_2O_3 layer characterization. For nanolaminates having 2 nm thickness of single layers the Bruggeman effective media approach is preferable.

Validation of the results:

List of publications by the author of the disertation:

1*. Z.Balevicius, A. Ramanaviciene, I. Baleviciute, A. Makaraviciute, L. Mikoliunaite, A. Ramanavicius, Evaluation of intact- and fragmented-antibody based immunosensors by total internal reflection ellipsometry, *Sensors and Actuators B Chemical*, 160 pp. 555-562, 2011.

2*. I. Baleviciute, Z.Balevicius, A.Makaraviciute , A.Ramanaviciene , A. Ramanavicius, Study of antibody/antigen binding kinetics by total internal reflection ellipsometry, *Biosensors and Bioelectronics*, 39, pp. 170–176, 2013.

3*. Z. Balevicius, I. Baleviciute, S. Tumenas, L. Tamosaitis, A. Stirke, A. Makaraviciute, A. Ramanaviciene , A. Ramanavicius, Study of antibody/antigen binding kinetics by total internal reflection ellipsometry. *Thin Solid Films,* dx.doi.org/10.1016/j.tsf.2013.10.090, 2013.

4*. A. A. Chaaya, R. Viter, I. Baleviciute, M. Bechelany, A. Ramanavicius, Z. Gertnere, D. Erts, V. Smyntyna and P. Miele, Tuning Optical Properties of Al_2O_3/ZnO Nanolaminates Synthesized by Atomic Layer Deposition, *Journal of Physical Chemistry C*, 118, pp. 3811-3819, 2014.

5*. A. A. Chaaya, R. Viter, I. Baleviciute, M. Bechelany, A. Ramanavicius, D. Erts, V. Smyntyna and P. Miele, Tuning Optical Properties of Al2O3/ZnO Nanolaminates Synthesized by Atomic Layer Deposition, *Physica Status Solidi C,* DOI:10.1002/pssc.201300607, 2014.

List of conferences, where the results of the dissertation were presented:

1. Z. Balevičius, , A. Ramanavičienė, , I. Balevičiūtė, , N. Ryškevič, , A. Kaušaitė-Minkštimienė, , A. Makarevičiūtė, , Y. Oztekin, , J. Baniukevič, , A. Ramanavičius, Total internal reflection ellipsometry for immunosensor design,

„The magnet for scientific innovation: PITTCON conference and EXPO 2011“, Atlanta, Georgia, March 13-18, 2011: abstracts. art. no. 1720-10P.

2. I.Baleviciute, Z. Balevicius, A. Makaraviciute, A. Ramanaviciene, A. Ramanavicius, Study of Antibody-Antigen Binding Kinetics by Total Internal Reflection Ellipsometry, 14th international conference and summer school „Advanced Materials and Technologies“, August 27 – 31, 2012, Palanga. p. 32

3. A. Ramanavičienė, A. Kaušaitė-Minkštimienė, J. Kirlytė, Z. Balevičius, I. Balevičiūtė , A. Makarevičiūtė, Y. Oztekin, A. Ramanavičius, Evaluation of immobilization techniques on the efficiency of immunosensors, „The magnet for scientific innovation: PITTCON conference and EXPO 2011“, Atlanta, Georgia, March 13-18, 2011: abstracts. art. no. 2200-12P.

4. A. Ramanavičius, A. Ramanavičienė, Z. Balevičius, I. Balevičiūtė , A. Kaušaitė-Minkštimienė, R. Bubnienė, Surface plasmon resonance and elipsometry biosensor for direct detection of antibodies, „PITTCON conference and EXPO 2010“, February 28 - March 5, 2010, Orlando, Florida: abstracts. art. no. 2820-9.

5. I. Baleviciute, A. Makaraviciute, Z. Balevicius, A. Ramanaviciene, A. Ramanavicius, Study of bovine leukemia virus antigen growth kinetics by total internal reflection ellipsometry, „ERPOS-12“, July 11-13, 2011, Vilnius, Lithuania.

6. A. Ramanaviciene, A. Kausaite–Minsktimieme, A. Makareviciute, J. Kirlyte, I. Baleviciute, Y. Oztekin, A. Ramanavicius, J. Voronovic, N. German, Immunosensors Based on Surface Plasmon Resonance and Electrochemical Techniques, „PITTCON conference and EXPO 2012“, March 11-15, 2012, Orlando, Florida: abstracts. art. No. 550-10.

7. Z. Balevicius, I. Baleviciute, S. Tumenas , A. Stirke , A. Makaraviciute , A. Ramanaviciene, A. Ramanavicius, In situ study of ligand-receptor interaction by total internal reflection ellipsometry, „ICSE VI“, 26-31 May 2013, Kyoto research park, Japan.

8. A. A. Chaaya, R. Viter, I. Baleviciute, M. Bechelany, P. Miele, A. Ramanavicius, D. Erts and V. Smyntyna, Optical and structural properties of

Al2O3/ZnO nanolaminates, deposited by ALD method, E-MRS 2013 FALL MEETING**,** September 16-20, Warsaw University of Technology, Poland.

Author's contribution:

Author personally performed all ellipsometric measurements on biomolecule layers and nanolaminates, constructed and applied optical models, suggested improved methods of proteins interaction kinetics analysis based on single wavelength and spectroscopic measurements, suggested model of proteins kinetics analysis which takes into consideration residence time effect, calculated kinetics constants. Author also made a significant contribution during analysis of the results and preparation of scientific publications.

CHAPTER 1
(Literature review)

1. 1 Ellipsometry

Two waves of the same wavelength and amplitude can behave differently during their interaction with matter if their electric field vectors are pointed in different directions. The light which is emitted from the sun or from a simple lamp is an assembly of waves having various directions (polarizations) and is called unpolarised light. When the electric field vector of the light is oriented to oscillate in one special direction, such light is called polarized. During polarization, all the other orientations of its electric field vectors are removed except for one. Partially polarized light can be defined using the parameter called the *degree of polarization* (P). This is expressed as a ratio of the intensity of the polarized plane waves (I_{pol}) and the total intensity of the irradiation (I_{tot}). Thus: $P=I_{pol.}/I_{tot.}$. Fully polarized light is obtained when $P=1$.

Such polarized light is characterised by three states of polarization: *linear*, *circular* and *elliptical*. Actually elliptical polarization is the most common polarization state. When light interacts with different optical systems, the polarization state and the degree of polarization can be changed. The method which is used for the measurement of the polarization state or the degree of the change of polarization is called *ellipsometry*.

Figure 1.1 presents a schematic diagram of the change of the polarization state when light with linear polarization is reflected from a sample having dielectric constants ε. The electric field vector (E) at any instant of time can be expressed using the two components called *s* and *p* polarizations. The E_p is the component which oscillates in the plane of incidence whereas E_s is the component that oscillates in a direction perpendicular to the incidence plane. In ellipsometry, the change of the polarization state is described using the two ellipsometric parameters or ellipsometric angles Ψ and Δ.

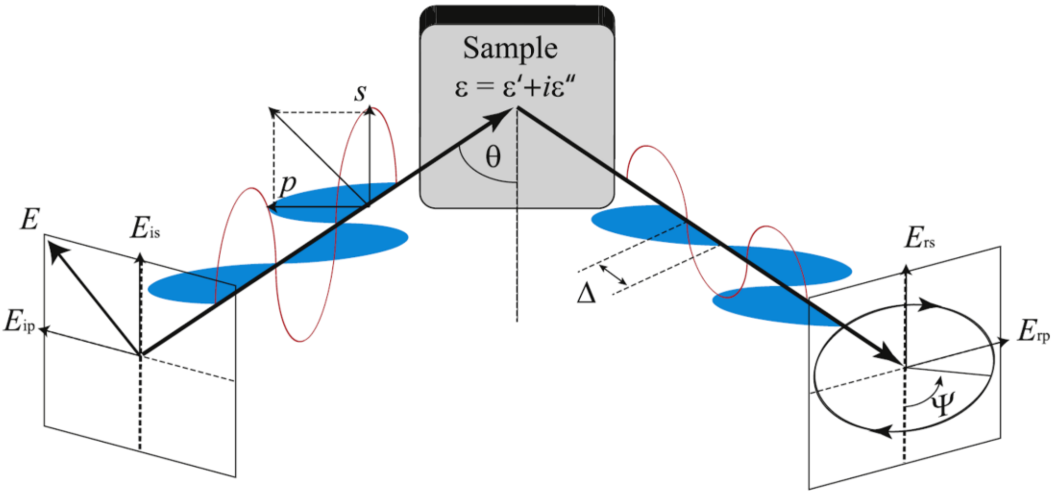

Fig.1.1 *Schematic diagram of the change of the polarization state after light reflection from the surface of a dielectric plate [T.W.H. Oates et al. / Progress in Surface Science 86 (2011) 328–376].*

Parameter Ψ describes the ratio between the amplitudes of the *s* and *p* polarized wave, while parameter Δ is the phase change $\Delta=\Delta_p-\Delta_s$, where Δ_p and Δ_s are the phases of the reflected light electric vector *p* and *s* components, respectively. The relation between the ellipsometric parameters Ψ and Δ and the change in polarization is expressed by the following equation:

$$\rho = \frac{r_p}{r_s} = \tan(\Psi)\cdot e^{i\Delta}; \qquad (1.1)$$

here $r_p = E_{rp}/E_{ip}$ and $r_s = E_{rs}/E_{is}$. Equation 1.1 is called *the main equation of ellipsometry*. Here tan (Ψ) is the amplitude ratio after reflection, while Δ shows the phase shift. difference.

Ellipsometry is very useful technique for the characterization of the surfaces and interfaces of thin films. It is mainly applied using the reflection mode and gives information about the parameters of the layers such as their thicknesses, refractive indexes (*n*) and their extinction coefficients (*k*). Ellipsometric measurements can be performed by changing the incident beam angle (α) or the wavelength (λ). In cases where both parameters α or λ are changed, method is called *variable angle spectroscopic ellipsometry* (VASE).

The ellipsometry data obtained for a wide range of angles and wavelengths, together with the known optical parameters or thicknesses of layers, allow one to “model” the single as well as the multiple layer samples. By comparing the observed data with the computer-generated “models” of the ellipsometer results, it is possible to deduce the thickness or the *n vs.* λ dependence of a specimen consisting of one or more overlaying layers made of different materials. The determination of the optical model and the appropriate thickness of such layer is the main task of ellipsometric measurements.

1.2. Optical models

The procedure for the determination of layer optical constants and thickness can be excluded only when the sample layer is very thick, homogeneous and does not have any surface roughness. For this purpose, different software is used. In many cases, however, the samples being examined have a layered structure and surface roughness. For these evaluation layered optical models are constructed in order to obtain a nominal sample structure. In these types of models, each layer is characterized using the values of their optical constants and their thicknesses. A fitting procedure using software has to be applied in order to obtain the dispersion function of each layer’s optical constant. If the fitted and the measured data correspond to each other and the obtained optical constants have physical meaning, the model is then considered to be correct. In all these optical models, the optical constants are calculated using different mathematical expressions called dispersion models.

1.2.1 Cauchy dispersion model

If the layer is considered to be transparent and is placed on a substrate having a known optical constant, the Cauchy dispersion [7] relation can be applied to each such type of layer.

The mathematical expression of the Cauchy dispersion is the following:

$$n(\lambda) = A + \frac{B}{\lambda^2} + \frac{C}{\lambda^4}, \qquad (1.2)$$

where $n(\lambda)$ is the refractive index and A, B, C are the analytical parameters used in the fitting procedure. The Cauchy dispersion function is a variant of the Sellmeier dispersion model [7]. This type of function is usually used for the study of biological and other organic layers which have dielectric properties. In the Cauchy dispersion model, the refraction index decreases toward the longer wavelength. This is the typical behaviour of transparent layers and only this shape of function can be accepted as having physical meaning.

1.2.2 The Lorentz dispersion model

The Lorentz model is based on a classical damped harmonic oscillator which assumes that the electron is harmonically bound to a fixed position on the nucleus [7]. The dielectric constant (ε) expressed using the Lorentz model is the following:

$$\varepsilon = 1 + \frac{e^2 N_e}{\varepsilon_0 m_e} \frac{1}{(\omega_0^2 - \omega^2) + i\Gamma\omega}, \qquad (1.3)$$

where e, N_e, ε_0, m_e, ω_0, i, ω, and Γ are the charge of electron, the number of electrons per unit volume, the vacuum permittivity, the mass of the electron, the resonant frequency, the incident light frequency and the damping coefficient, respectively. Many other optical models are derived from this classical model. Oscillator models are widely used in order to calculate the absorption of the different layers.

1.2.3 The Drude dispersion model

This model is used to describe how metals and semiconductor layers absorb light. It is usually used for the study of non-magnetic isotropic metal layers such as thin gold film (about 50 nm) and is derived from the Lorentz oscillator model [8]. It is assumed that the free carriers are equally distributed and oscillate at the same plasma frequency. The refractive index (*n*) and the extinction coefficient (*k*) of such metal layers can be express by the following equation:

$$n(\omega)=1-\frac{\omega_p^4}{\left(\omega^2+\gamma_f^2\right)^2},\ k(\omega)=\frac{\omega_p^4\gamma_f^2}{\omega^2\left(\omega^2+\gamma_f^2\right)^2}, \qquad (1.4)$$

Here ω - the frequency of light ω_p - the plasma frequency which is a function of the concentration of free electrons γ_f - the frictional force constant..

1.2.4 The Gaussian oscillator

The Gaussian shape of the absorption curves is typical for layers made of amorphous and polycrystalline materials [9].This type of function is usually used for the modelling of the refractive indexes of various glasses or other disordered materials such as polymers, etc. The equation provided by the Gaussian oscillator is the following:

$$\varepsilon = Amp_n\left[\Gamma\left(\frac{E-En_n}{\sigma_n}\right)+\Gamma\left(\frac{E+En_n}{\sigma_n}\right)+i\cdot\left(\exp\left[-\left(\frac{E-En_n}{\sigma_n}\right)^2\right]+\exp\left[-\left(\frac{E+En_n}{\sigma_n}\right)^2\right]\right)\right], \quad (1.5)$$

where $\sigma_n=\frac{Br_n}{2\sqrt{\ln 2}}$, Br is the broadening; Amp_n - the amplitude, Γ - the function which gives it a special shape based on the Kramers-Kroning relation [10], E , E_n the energy of light and the centre energy.

1.3 The effective medium approach

Effective medium approximation can be used to describe the heterogeneous optical properties of materials. Using this approach, the effective dielectric constants of such materials can be modelled. Heterogeneous materials consist of isotropic components which are macroscopically uniform.

1.3.1 The linear effective medium

The simplest form of such heterogeneous media consist of two components A and B and can be imagined as having two forms (Fig. 1.2). The first form is that all its boundaries are parallel to the applied electric field, in the second all boundaries are perpendicular to the electric field. The dielectric function of the microstructure, which is parallel to the electric field vector, is described by:

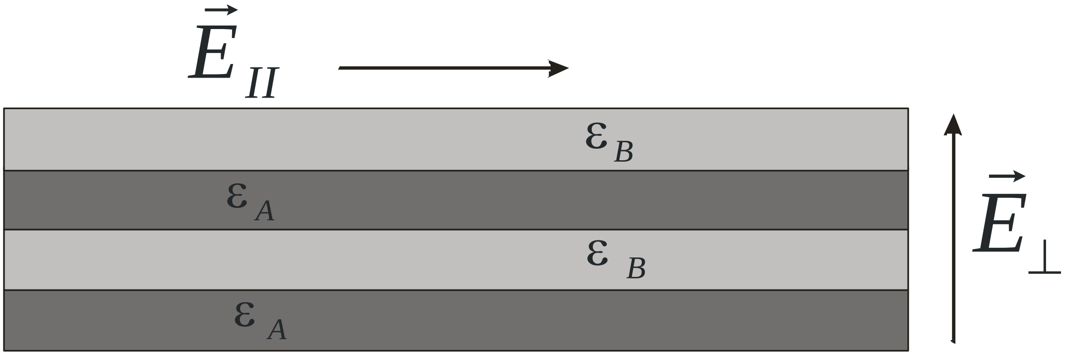

Fig. 1.2 *Heterogeneous media of two components having parallel boundaries. Linear effective medium approach.*

$$\varepsilon_{II} = f_A \cdot \varepsilon_A + f_B \cdot \varepsilon_B \qquad (1.6)$$

where f_A and f_B are the volume fractions and ε_A and ε_B are the materials' A and B dielectric functions, respectively. When all boundaries are oriented perpendicular to the applied electric field, the average dielectric function is:

$$\varepsilon_{\perp} = \frac{\varepsilon_A \varepsilon_B}{f_A \varepsilon_B + f_B \varepsilon_A} \qquad (1.7).$$

These values of the dielectric functions are scalar. Thus there are limitations in the effective use of such mediums. They cannot be used if their inclusions are too small because of their dielectric identity are close to the wavelength of the light. Such very small particles have dielectric functions which are different from those of normal size due to quantum effects and scattering, respectively. The larger the fill factor or the closer the particles are to a cluster structure, the bigger become the errors in applying EMA. To avoid this, a random unit cell needs to be constructed. The simplest case is when the particles are spherical. In such a case, it can be assumed that all the materials are heterogeneous because the dipoles are distributed in a lattice. This leads to the Clausius-Mossoti expression of ε. This means that these particles will scatter the light as dipoles [11].

1.3.2 The Lorentz-Lorenz effective medium

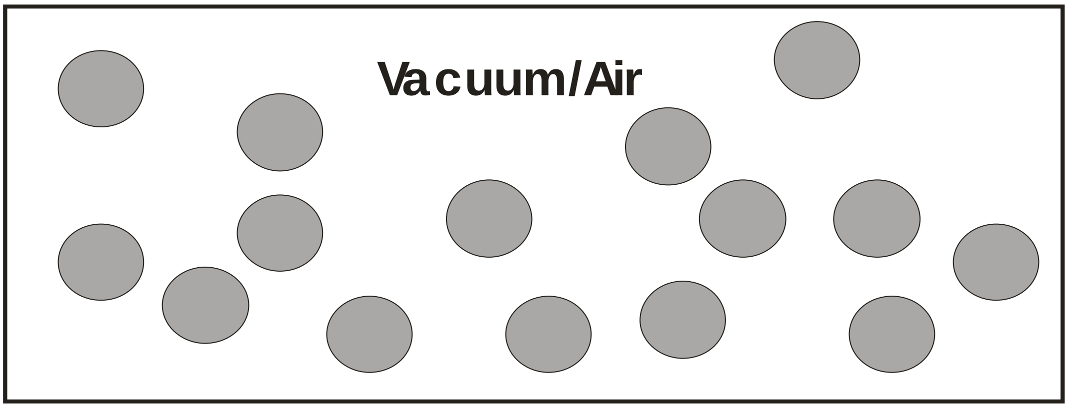

Fig. 1.3 *The Lorentz-Lorenz effective medium approach* **-** *spheres dispersed in a vacuum*

If the spheres are dispersed in a vacuum (Figure 1.3), they interact with the light in the same manner as dipoles. This approximation is called the Lorentz-Lorenz effective medium. The expression of this approximation is the following:

$$\frac{\varepsilon-1}{\varepsilon+2}=f_A\frac{\varepsilon_A-1}{\varepsilon_A+2}; \quad (1.8)$$

where ε is the dielectric function and $f_A = n\cdot V$ is the fraction of the volume occupied by the spheres [12]. This approximation can be used in the case of optical models created for obtaining the dielectric function of the interface between the air and a film having a rough surface.

1.3.3 The Maxwell Garnet effective medium

This approach is used in case when the dielectric constant of the mixed phase materials is unknown (Figure 1.4). Here one phase which consists of spheres having dielectric function ε_B is distributed in other phase having the dielectric function ε_A, which corresponds to the host material:

Fig. 1.4 *Mixed phase materialsof Maxwell Garnet effective medium model.*

$$\frac{\varepsilon-\varepsilon_A}{\varepsilon+2\varepsilon_A}=\left(1-f_A\right)\frac{\varepsilon_B-\varepsilon_A}{\varepsilon_B+2\varepsilon_A}; \quad (1.9)$$

The filling factor f_A is the ratio of the volumes $f_A=\left(a/b\right)^3$, where *a* and *b* are the radius of the spheres that are in and out, respectively [13].

This value corresponds to the simple case when only grains with one radius are distributed in a matrix with other particles having identical dielectric constants.

1.3.4 The Bruggeman effective medium

If there is a structure which has an equivalence of constituencies, it can be imagined as a sphere having two components where one has the dielectric function ε_A and other ε_B (Figure 1.5). The probability of a unit cell to have dielectric constant ε_A is f_A and $f_B = 1 - f_A$ for dielectric constant ε_B. [14].

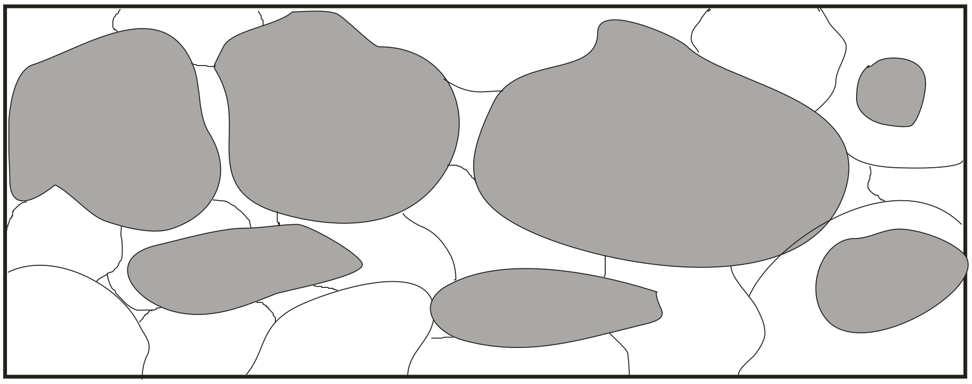

Fig. 1.5 *Two components with different dielectric function. Bruggeman effective medium approach.*

The dielectric constant of such a composite is expressed by the equation:

$$f_A \frac{\varepsilon_A - \varepsilon}{\varepsilon_A + 2\varepsilon} + (1 - f_A) \frac{\varepsilon_B - \varepsilon}{\varepsilon_B + 2\varepsilon} = 0; \qquad (1.10)$$

The Bruggeman effective medium theory is often used for the ellipsometric modelling of optical constants in aggregate microstructure materials where these two constituencies are randomly mixed.

1.3.5 Shape effects

All the effective medium approximation theories discussed above are used for the study of spherical particles. But the electric fields in and out of the particles will remain different and this will depend on the shapes of the particles. In the case where the optical constants of the EMA layers are being modelled, the depolarisation factor can be used to make corrections. If there are dipoles imagined as spheres dispersed in a symmetric crystal, the value of the depolarization factor is 1/3. But there are other limiting forms of particles such as thin slabs or circular cylinders. The depolarization factor of a thin slab pointed along the normal axis direction is equal to 1, but in a plane this is 0; for a circular cylinder, it is 1/2 in the transverse axis direction and 0 in the longitudinal. If the particles have ellipsoidal shape ε_j in the j ($j=x,y,z$) direction, the expression using Bruggeman effective medium approximation (for 2 constituencies), takes on the following form:

$$f_A \frac{\varepsilon_A - \varepsilon_j}{\varepsilon_j + L_j(\varepsilon_A - \varepsilon_j)} + (1 - f_A)\frac{\varepsilon_B - \varepsilon_j}{\varepsilon_j + L_j(\varepsilon_B - \varepsilon_j)} = 0 \qquad (1.11)$$

Here Lj is the depolarization factor. In this case, it is the same as for a randomly oriented ellipsoid.

There are additional difficulties if the Maxwell Garner EMA is used in the case of ellipsoids. The main difficulties arise from the shape of the random unit cell, depending on what type is the particle and the shell, because it can be that the sphere is in an ellipsoid or an ellipsoid in a sphere or an ellipsoid in an ellipsoid. For an ellipsoidal particle having dielectric function ε_A which is coated by an ellipsoidal with dielectric function ε_B, the equation is expressed as:

$$\varepsilon = \varepsilon_B \frac{L_j^A \varepsilon_A + \varepsilon_B(1 - L_j^A) + f_A(1 - L_j^B)(\varepsilon_A - \varepsilon_B)}{L_j^A \varepsilon_A + \varepsilon_B(1 - L_j^A) - f_A L_j^B(\varepsilon_A - \varepsilon_B)} \qquad (1.12)$$

1.4 Surface plasmon resonance

Among various layered systems such as a single dielectric layer surrounded by two discontinuous mediums or multi-layered structures consisting of layers having different dielectric constants, special attention has to be paid to the metal/dielectric interface. In such cases at total internal reflection and conditions when the incident light is directed at an angle higher than the critical Brewster's angle, a phenomenon called the *surface plasmon resonance* (SPR) occurs. If the boundary between glass and metal contains thin metal film, the light photons resonate with the free electrons in the metal and provide strongly localized electric fields whose change is very sensitive to the differences of the dielectric functions occurring in the surroundings [15]. For the excitation of such surface plasmons, noble metals such as gold, silver or copper are usually used. [16] There are other materials which can also be used such as the large band gap metal oxides like ZnO or SnO_2 [17].

SPR is produced when the *p*-polarized light component of the electric field vector directed perpendicular to the sample surface is propagating on it. Because the *s*-polarized component is always parallel to the surface, only the *p*-polarized light excites the surface plasmons. When SPR conditions are reached, the *p*-polarized light reflection is $r_p=0$ and the evanescent waves which the electric field decreases exponentially are exited. The typical decay of this field occupies about a 700 nm area from the surface of the metal. In a case where the metal layer is covered by dielectric layer having a thickness of a few tens of nm, the evanescent wave electric field in this layer can be imagined as being uniform and is very sensitive to the optical parameters of the dielectric layer. Thus changes of the evanescent wave electric field induce large changes in the polarization of the reflected light and for this reason, ellipsometry is a very effective method for studying the properties of the various layers deposited on the surface of the metallic layer.

1.5 Kinetics analysis models

The adsorption of big molecules such as proteins on a surface is a multistep process. The analysis and understanding of what is going on when these molecules interact with a surface is of great interest for the analysis of biocompatibility and for the development of biosensors. For this purpose, the mathematical models which take into account the most important processes during protein adsorption are used to obtain information about the interaction mechanisms.

1.5.1 Generalized Langmuir equation

There are five major steps which occur during the proteins' adsorption and should be taken into account in basic description of proteins adsorption mechanism: (i) the transport of the protein molecule to the adsorbing surface, (ii) the attachment step, (iii) the rearrangement of the conformation of the adsorbed molecule during to their adaptation to the 'microenvironment', (iv) the detachment step, and (v) diffusion away from the surface [18]. Such molecule transport mechanism was well analysed by Adamczyk et al., 1994; Rajagopalan and Kim, 1977; Matijevic et al., 1987. The contribution of each step to the kinetics of the biological layer formation depends on the experimental conditions, i.e. on the concentration of the analyte in the buffer solution, the time during which the kinetics are measured and the tendency of the adsorption: fully reversible, partially irreversible or completely irreversible. Usually the steps i and iii are not taken into consideration and the kinetics analysis can be performed using the standard Langmuir equation. Difficulties using this equation come about when it is applied to describe the adsorption of large molecules because it does not accurately represent all 'surface effects' of the protein layer which is formed. This can be seen as the result of a decrease of the adsorption rate. To make a more accurate analysis of such protein adsorption kinetics and to avoid this difficulty, a generalized Langmuir equation was proposed by Schaaf and Talbot, 1989; Jin et al., 1994. The general form of this equation is the following:

$$\frac{d\rho}{dt} = k_a c \phi(\rho) - k_d \rho \qquad (1.13)$$

where ρ is the surface density of the adsorbed molecules, c is the concentration of the solute immediately above the adsorbing surface, $\phi(\rho)$ is the available surface function, which shows the probability that molecule will find a free interaction place on the surface which is already covered by the other molecules and k_a and k_d are the adsorption and desorption constants, respectively.

In the case of a completely irreversible association process, $k_d = 0$ and only the first term of the equation (1.13) is important. The saturation of the monomolecular layer formation occurs when all the surface with target molecules is covered by the analyte. If desorption is present ($k_d \neq 0$), the formation of the layer stops when the equilibrium between the association and disociation processes is reached. In the case of the linear dependence of association and dissociation on the trapped molecule concentration, the equation (1.13) transforms to the standard Longmuir equation.

Typical for processes which can be described by this equation is that at steady state conditions, not all the sites of the target molecules are occupied and after the replacement of the buffer solution by analyte-free liquid, the formed monomolecular layer of analyte is completely dissociated. The kinetics of such association/dissociation cycle has characteristic analytical signals with rise and fall times which are associated with the adsorption and desorption times of the analyte, respectively. In such case, the surface function $\phi(\rho)$ is simply related to the chemical potential of the adsorbed species and the ratio between k_d and k_a gives the possibility to calculate the standard Gibbs energy of the reaction.

However, often the desorption rate during the formation of protein layer is a function of the residence time of the adsorbed molecule [19]. This could be viewed as some sort of „memory“phenomen. There are two most possible scenarios of such process: fully reversible adsorption and partial reversibility.

In the case of fully reversible adsorption *via* two ligands, each ligand of the analyte exists in one of two states: unbound or bound. An unbound ligand binds to the surface at a rate μ, while a bound ligand dissociates at the rate λ.

The reversible adsorption *via* two ligands cannot be simply deducted from an ellipsometric experiment. It is estimated by modelling of the biomolecular layer formation process and fitting calculated results with data. This modelling usually is not a trivial procedure because it requires additional confirmation that adsorption *via* two ligands is actually taking place in biomolecular layer formation process. This case is often observed if antibodies are applied in formation of sensitive layer or they are acting as analytes, because most of native antibodies have two ligands that are available for the interaction with antigen.

In case of partial reversibility, only a fraction of the adsorbed protein may desorb. When this effect takes place, the interaction between the proteins can be stronger due to the unfolding of the proteins and the optimisation of the interaction with the active surface. This means that at each time instant of the binding process, a part of the molecules which reached the targets are irreversibly bonded to these targets. The replacement of the solution with the analyte by a solution without the analyte only partially destroys the biomolecular layer. This can be detected from the ellipsometric measurements as a difference in the refractive index of the surface layer before and after the washing procedure.

1.5.2 The partial reversibility model

If partial reversibility takes place, the protein molecule can desorb from the surface at a rate μ or can be bounded irreversibly at a rate λ [18]. In this case $\phi(\rho)$ =1-ρ_1-ρ_2 , where ρ_1 and ρ_2 are the surface densities of the molecules bounded to the surface *via* one or two ligands, respectively. This process can be described by the following system of differential equations:

$$\begin{aligned} \frac{d\rho_1}{dt} &= k_a c \cdot (1-\rho_1-\rho_2) - (\mu+\lambda)\rho_1 \\ \frac{d\rho_2}{dt} &= \lambda\rho_1 \end{aligned} \qquad (1.14)$$

The solution of this equation in time units $k_a c$ is the following:

$$\rho_1(t) = \in^{-1} \exp\left(-\frac{1+\lambda+\mu}{2}t\right)\sinh(\in t), \qquad (1.15)$$

$$\rho_2(t) = 1 - \in^{-1} \exp\left(-\frac{1+\lambda+\mu}{2}t\right) \times \left(\in \cosh(\in t) + \frac{1+\lambda+\mu}{2}\sinh(\in t)\right) \qquad (1.16)$$

Here $\in^2 = \left(-4\lambda + (1+\lambda+\mu)^2\right)/4$

It has to be noted that this partial reversibility process essentially differs from the completely irreversible one, because even at steady state conditions in the case of partial reversibility, not all the sites of the target are irreversibly bonded with the analyte molecules.

1.6 Bovine leukemia virus and its detection

The bovine leukemia virus (BLV) is a retrovirus which affects cattle. This retrovirus usually has a long incubation period without exhibiting any visible symptoms and is very similar to the human leukemia T-lymphotropic type virus1_HTLV-I [20]. BLV can cause the enzootic bovine leucosis (EBL) disease and affects the B lymphocytes [21]. This BVL virus can be found in body fluids (nasal and bronchial fluids, saliva, milk) [22]. For this reason BLV

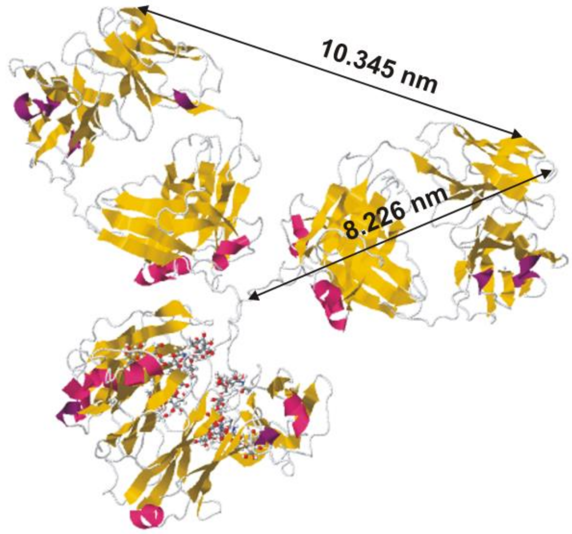

Fig. 1.6 *Typical structure of antibody [http://www.rcsb.org/pdb/explore/jmol.do?structureId=1IGY&bionumber=1].*

is very important in modeling studies of oncological viruses, such as HTLV-I or HTLV-II, and in the creation of vaccines against these retroviruses [23]. In figure1.6 is presented schematic diagram of typical structure of antibody.

If the cattle is infected by BLV an antibody response to an infection is generated; and after this 1IgY-class antibodies [24] that are formed during this response are found in both the serum and the milk of infected cattle. The routine diagnosis of BLV infection is thus based on this antigen-antibody reaction. For BVL detection, several methods based on the antigen-antibody interaction have been used.

The *amperometric method* was used in [24,25].Polypyrrole (Ppy) was applied as the matrix for the preparation of a molecularly imprinted polymer (MIP), which was suitable for the label-free detection of the bovine leukemia virus (BLV) glycoprotein *gp*51. The molecules of the *gp*51 were then removed from the polymeric backbone and the molecularly imprinted polypyrrole (mPpy) was made ready for the recognition of the *gp*51 in the aqueous solution. The pulsed amperometric method was then applied for the detection of the label-free *gp*51. The other new amperometric immune-sensor for the detection of antibodies against the bovine leukaemia protein (*gp*51) was demonstrated in [26]. The detection of the antibody-antigen complex formation was based on the application of secondary antibodies labeled with horseradish peroxidase. Ferrocenecarboxylic acid and tetramethylbenzidine were selected as suitable mediators for this immune-sensor. The sensitivity of the system was then compared with the results of the enzyme-linked immune-sorbent assay (ELISA) and the agar gel immune-diffusion (AGID) reaction and was found to be sufficient for the detection of the usual anti-*gp*51 antibody concentration present in the blood serum of BLV-infected cattle.

The electrochemical impedance spectroscopy (EIS) method was also used for determination of antibodies against BLV proteins *gp*51 (anti-*gp*51) [26]. This immunosensor was based on the bovine leukaemia virus (BLV) protein (*gp*51) entrapped within the electrochemically-synthesized polypyrrole (Ppy/*gp*51). This Ppy/*gp*51 layer interacted with the antibodies against *gp*51 (anti-*gp*51-Ab) which were present in significant concentrations in the blood serum of BLV infected cattle. After this interaction, the protein complex (Ppy/*gp*51/anti-*gp*51-Ab) was formed. The horseradish peroxidase (HRP) labeled secondary antibodies (Ab) against anti-*gp*51-Ab were then applied as agents interacting with the Ppy/*gp*51/anti-*gp*51-Ab and forming the large protein complex (Ppy/*gp*51/anti-*gp*51-Ab/Ab). An EIS study was performed for electrodes modified with different Ppy layers and an optimal equivalent circuit was adopted for the evaluation of the EIS spectra.

A piezoelectric affinity sensor based on the immobilized bovine leukaemia virus (BLV) envelope protein *gp*51 was described in [27].In this research a quartz crystal microbalance (QCM) was used to register the interaction of the *gp*51 with specific antibodies from the blood serum of BLV-infected cattle. The protein *gp*51 was cross-linked with the glutaraldehyde on the platinized surfaces of the quartz crystals to prevent fast desorption. The behavior of the coating containing the *gp*51 was studied in a pure glycine buffer (pH 7.3) as well as in a glycine buffer (pH 7.3) mixed with blood serum from BLV-infected and not infected cattle.

The *surface plasmon resonance* (SPR) method was applied in several researches which were intended for determination of anti-*gp*51 [28,29,30]. In [29], a SPR sensor was used for the detection of the level of anti-*gp*51 in the blood serum. The minimal dilution of the serum should be 1:500. Later the same authors in [30] demonstrated a sensor which was used for the detection of the level of anti-*gp*51 present in milk serum. It was shown that this immunosensor is more sensitive, rapid and simple when compared to the traditional AGID test. It was stated that this immunosensor can be used for the screening for bovine leucosis. The minimal dilution of the milk serum should be 1:20. In [30], an immune-sensor for the determination of the bovine leukaemia virus antigen (*gp*51) was developed using the surface plasmon resonance (SPR) technique. In this work, a SPR-chip coated with gold was used in the immune-sensor design. Different strategies of antibodies immobilization were investigated such as oriented immobilization of specific antibodies fragments (fraganti-*gp*51) on a gold surface obtained after chemical reduction and random immobilization of the intact antibodies (anti-*gp*51) on a gold surface[30, 64]. Immobilization based on the application of frag-anti-*gp*51 was found to be the most suitable for the design of a SPR-immuno-sensor to be used for *gp*51 detection. The SPR sensor created using frag-anti-*gp*51 was tested along a range from 0.01 to 0.5 mg/mL of *gp*51 antigen concentration. This immune-sensor exhibited sufficient antigen binding capacity, simplicity and low cost when compared to the currently evaluated techniques [68, 72].

1.7 Granulocyte colony stimulating factor (GCSF)

The granulocyte colony stimulating factor (GCSF) is a type of protein produced in body immune cells as a grow factor. These glycoproteins are able to bind proteins to receptors on the bone marrow produced stem cells and to transfer them to the blood [31]. GCSF is often used as a drug for the treatment of neutropenia disease. This disease is able to be diagnosed when a very low number of neutrophils is detected [32].When the number of these neutrophils decreases, the organism can be infected. To keep the neutrophils number normal becomes especially important after chemotherapy treatment because this stops the bone marrow from making white blood cells. This protein selectively stimulates the differentiation as well as the proliferation of committed progenitor cells and the activation of mature neutrophils [33].

Such biological drugs have become very important in drug treatment. Cytokine GCSF is one of the most common proteins used in such biological pharmacology [34]. To provide effective treatment against neutropenia, a series of injections of GCSF cytokine are needed because of the fast removal from the body which is caused by the neutrophil cleaning processes [35]. An important pharmacokinetic parameter is the pharmacokinetic (PK) profile which indicates its half-life from a single infusion. Most of the research of the last decade has been focused on the problem of extending the half-life of proteins such as GCSF. Such prolonged half-life gives the possibility of using a lesser amount of GCSF as well as making the drug more active [36]. Such extensions of its half-life are based on processes such as genetic fusion using a linker amino acid replacement, which results in the reduction of immunogenicity, proteolytic instability and conjugation with natural or synthetic polymers (polysialylation, HESylation and PEGylation) [37]. Figure 1.7 shows the GCSF receptor (a), monomer (b) and dimer (c) which were developed using the genetic fusion method. The final stage of the monomer interaction with the receptor is the creation of a dimer molecule consisting of two monomers bonded onto one receptor. The other possibility can be the direct association of the dimer molecule onto the receptor. One of the key tasks in this area of research is the comparison of the effectiveness of the monomer and dimer to react with the GCSF receptor. This requires a sufficiently sensitive, non-destructive method which would enable the study of the kinetics of the binding process in both cases i.e. when the receptor reacts with the monomer and the dimer molecules. Spectroscopic ellipsometry can be used for this purpose. However, more detail analysis of the application of this method needs to be investigated.

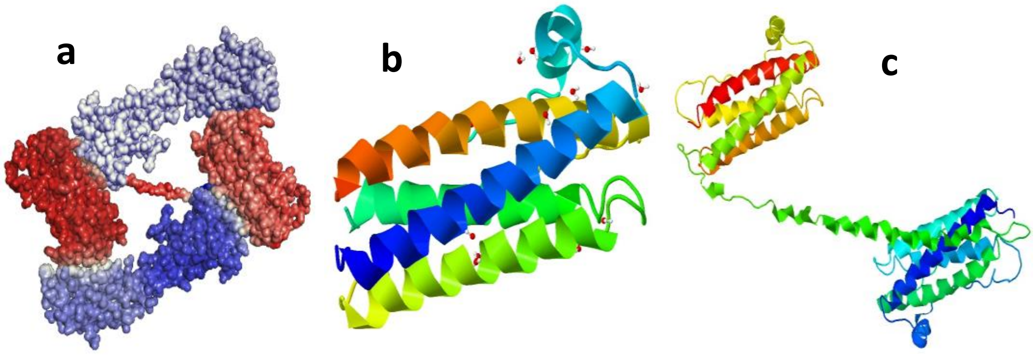

Fig. 1.7 *Structure of the GCSF receptor (a), monomer (b) and dimer (c): [http://pdb.org/pdb/explore/explore.do?structureId=2D9Q], VU IBT Department of bioinformatics.*

1.8 Nanolaminates

Nanolaminates are new generation nano-scale multi-layered materials which have unique properties, such as high dielectric constants and improved electrical, optical and mechanical properties. These properties depend on the materials from which such nanolaminates are formed and the thicknesses of each layer. Usually these multi-layered structures are made by adding altering layers having nanometer thicknesses (less than 50 nm). Nanolaminate materials are fully dense, ultra-fine grained solids, which exhibit a high concentration of interface defects. For the preparation of such nanolaminates, different materials such as ZnO, Al_2O_3, Ta_2O_5, TiO_2, ZrO_2, HfO_2 oxides can be used [38,39,40]. Of particular interest is the n-type semiconductor ZnO because of its individual properties such as a wide band gap, high conductivity, room temperature photoluminescence, hexagonal crystal structure and the fact that it is transparent in the visible spectral range. Transparent conducting oxide films (CTO) are widely used in electronic devices as well as in flexible electronic devices (FED), optoelectronics and solar cells. Thus the fabrication of such ZnO nanolayers is easy, non-toxic and not expensive. They also have good heat stability [41]. The electrical and optical properties of ZnO can also be tuned by doping. For this purpose, Al and Al_2O_3 are used. In the case of ultra-thin films, the dielectric, electric and optical properties of these Al_2O_3/ZnO multilayer structures can be changed by means of quantum confinement. For the preparation of such nanolaminates, different methods such as atomic layer deposition (ALD), DC magnetron sputtering, RF magnetron sputtering [42], chemical vapor deposition [43], pulsed laser deposition [44] and the sol–gel process [45] are used. The refractive index of ZnO can differ, depending on the layer nanostructure [46]. Nanolaminates formed using the ADL method when ZnO is grown onto Al_2O_3 exhibit different growing directions compared to those made of pure ZnO layers [47]. When amorphous Al_2O_3 layers are used for the formation of the nanolaminate bilayers, they stop the ZnO crystal from growing [48].

Materials such as metal oxide nanolaminates can be used in biosensors based on the colour change of the reflected light. The biomolecules being detected usually are far smaller than the resolution of the human eye. This creates the main problem for the visual detection of specific molecular interactions. However, the unaided eye can detect changes in thicknesses of the same order as the sizes of the biomolecules if the means of detection exploits the interference conditions of reflected white light [49]. Isolated molecular interactions are generally not sufficient to generate visual signals. However, if these specific molecular interactions are amplified and transduced into thin films layered on an optically coated surface, the increased mass deposited on the surface can be detected visually as a consequence of the increased pathlength taken by the reflected light waves. Thus if the optical film has a thickness which in terms of its optical length is ¼ of the wavelength λ_0 of the visible light or odd multiples (such as $\frac{3}{4}\lambda_0$), the optical film functions as an antireflection film. When the intensity of the reflected light in a direction perpendicular to the optical film becomes 0 at wavelength λ_0, the sensor produces an interference colour. In a case when optical film is covered by a few nm thick biochemical substance, such as a protein having the same refractive index as the optical film, the reflection spectrum changes. The effective refractive indexes as well as the thicknesses of these nanolaminates can be changed during preparation so that they satisfy the best sensitivity requirements for sensing the selected biomaterials. For this reason, the spectroscopic ellipsometry method can be very useful for the determination of the effective refractive indexes of such nanolaminates.

CHAPTER 2

Materials and methods

In this chapter the technologies of preparation of multi-layered structures used for investigation of Bovine leukaemia virus antibody-antigen (*gp*51) interaction and granulocyte colony stimulating factor (GCSF) interaction with its receptor is presented. It also contains the description of synthesis of Al_2O_3/ZnO nanolaminates using atomic layer deposition (ALD) method, structural properties of these laminates and ellipsometric parameters measurement technique.

2.1 Preparation of multi-layer structures used for Bovine leukaemia virus antibody-antigen interaction investigation

Materials. The 2-Mercaptoethanol and albumin were purchased from Carl Roth (Germany), N-hydroxysuccinimide (NHS) and N-(3-dimethylaminopropyl)-N-ethyl-carbodiimide hydrochloride (EDC) from AlfaAesar (Karlsruhe, Germany). Ammonium sulphate, 11-mercaptoundecanoic acid (MUA) and all other chemicals were obtained from Sigma–Aldrich Chemie Gmbh (Steinheim, Germany) and were of analytical-reagent grade or better. Bovine leukaemia virus protein *gp*51 and bovine blood serum containing antibodies specifically interacting with *gp*51 (anti-*gp*51) were obtained from BIOK (Kursk, Russia). All aqueous solutions were prepared in HPLC-grade water purified in a Purator-B Glas Keramic (Berlin, Germany).

Antibody against BVL precipitation using ammonium sulphate. Serum containing immunoglobulin fraction including anti-*gp*51 (2 ml) was mixed and continuously stirred with an equal amount of saturated solution of ammonium sulphate, which was added drop wise to prevent local precipitation of proteins. The resulting mixture was kept at 4° C temperature overnight. Then the solution was centrifuged at 5000 rpm for 20 min. The supernatant was decanted and the pellet was dissolved in 2 ml 0.01 M phosphate buffer saline (PBS) (pH 7.4). The purification procedure was performed twice. The solution was dialyzed against the PBS at 4° C overnight. Finally, the immunoglobulin concentration was estimated using UV-Vis spectrophotometer (Lambda 25, PerkinElmer, USA) at $\lambda = 260$ nm and $\lambda = 280$ nm. Determined immunoglobulin concentration after purification was of 3.55 mg/ml.

Antibody against BVL fragmentation by reduction with 2-mercaptoethanol. Antibody solution (37.5 ul) was mixed with 0.1 M 2- mercaptoethanol solution (210 ul) and 0.01 M PBS (pH 7.4, 52.5 ul); final concentrations of immunoglobulin and 2-mercaptoethanol in prepared solution were 0.44 mg/ml and 70 mM, respectively. The mixture was incubated at 37 °C temperature for during 90 min. The 2-mercaptoethanol reduces disulphide bridges in the hinge region of the antibody molecule which holds two heavy chains together and from one immunoglobulin molecule (H–L) 2 two reduced antibody fragments (H–L) are formed. After treatment with 2-mercaptoethanol the mixtures were dialyzed against the sodium acetate buffer, pH 4.5, for 4 h using tubes for dialysis with molecular weight cut-off membrane of 6–8 kDa. The tubes were purchased from Novagen (Darmstadt, Germany). Prepared solution of frag-Ab was used immediately after preparation. Other additional purification procedures were avoided because according to the published results by other authors [50], reducing agents have only minor effect on efficiency of fragmented antibody binding on gold efficiency, but they significantly reduce the binding of blocking agent (e.g. BSA). Therefore, reducing agent can act as an additional blocking agent, which binds to gold through the thiol group and it blocks uncovered gold surface. Therefore, complete removal of 2-mercaptoethanol from the solution is not always relevant.

2.2 Formation of monomeric (mGCSF) and dimeric (dGCSF) granulocyte colony stimulating factor and its receptor (GCSF-R) layers

Materials The 11-Mercaptoundecanoic acid (11-MUA), human serum albumin (HSA), N-(3-dimethylaminopropyl)-N′-ethylcarbodiimide hydrochloride (EDC), N-Hydroxysuccinimide (NHS), 30% hydrogen peroxide solution, and protein G were purchased from Sigma Aldrich. Granulocyte colony stimulating factor (mGCSF) at 1 mg/ml and dimeric GCSF [51] at various concentrations in 10 mM acetate, 5% D-sorbitol, 0.0025% Tween 80, pH 4.0 buffer were obtained from Profarma UAB. The GCSF receptor (GCSF-R) fused with antibody fragmented crystallisable (Fc) was purchased from Abcam, 96%. All aqueous solutions were prepared in type I ultrapure water purified by a Direct-Q 3 Ultrapure Water System from Millipore.

Substrate surface preparation. Two similar gold sensor disks (Sample A and B) were prepared by chemically cleaning with piranha solution (1/3 peroxide, 2/3 sulphuric acid) for 2 min and then rinsing with ethanol and type I water. A self-assembled monolayer (SAM) of 11-MUA was formed by immersing the prepared chip in a 1 mM 11-MUA solution in ethanol for 12 h. Afterwards, it was rinsed with ethanol and type I water, and dried with argon gas. For the activation of the carboxyl groups of the 11-MUA SAM, a solution of 0.1 M NHS and 0.4 M EDC was used. The solution was prepared on the spot by mixing 0.1 M NHS and 0.4 M EDC solutions of equal volume in water and then injected into the cell for 300 s. Both samples are then rinsed with acetate buffer pH = 4. From this point, the protocols differ for each sample. In the case of sample A layer of covalently immobilized protein was treated during 900 s with 1 M, pH = 8.5 ethanolamine hydrochloride to block the remaining unbound activated carboxyl groups of the SAM for 900 s. For regeneration of non-specifically bound protein it was rinsed with a 10 mM, pH = 3 solution of glycine. The cell buffer is then switched from acetate to 140 mM NaCl, 2.7

mM KCl, 10 mM Na_2HPO_4, 1.8 mM KH_2PO_4, pH = 7.4 phosphate buffered saline (PBS). In the case of sample B, a layer of non covalently (oriented) bound GCSF-R was formed on a layer of covalently immobilized protein G which specifically binds to the Fc subunit of the GCSF-R fusion protein to form an oriented layer of GCSF-R. To accomplish receptor layer this receptor was injected into the cell for 2000 s, and after that rinsed with PBS buffer solution. In the case of covalently bound receptor, regeneration of the receptor was possible by injecting glycine for 300 s, whereas the non-covalently bound GCSF-R was washed away and the layer of protein G was regenerated instead.

2.3 Synthesis of Al_2O_3/ZnO nanolaminates by atomic layer deposition (ALD) method

The diethyl zinc (DEZ) (Zn (CH2CH3)2, 95% purity, CAS: 557-20-0) and trimethylaluminum (TMA) ((CH3)3Al) 98% purity, CAS: 75-24-1) used for synthesis were purchased from Sigma Aldrich. Silicon wafer p-type (100) was from MEMC Korea company and glass substrates from RS France. Substrates were precleaned in acetone, ethanol, and deionized water for 5 min to remove organic contaminants. A custom-made atomic layer deposition (ALD) reactor was used for the synthesis of Al_2O_3/ZnO multilayers. ALD was performed using sequential exposures of TMA (DEZ) and H2O separated by a purge of nitrogen with a flow rate of 100 sccm. The deposition regime for ZnO and Al_2O_3 consisted of a 0.1 s pulse of DEZ (TMA), 30 s of exposure to DEZ (TMA), 30 s of purge with nitrogen followed by 2 s pulse of H_2O, 30 s of exposure to H_2O, and finally 40 s purge with nitrogen. ZnO thin films as well as Al_2O_3/ZnO nanolaminates with different numbers of cycles were deposited on both Si substrates and glass substrates by ALD. During the deposition temperature was fixed to 100 °C. The ALD cycling and parameters of nanolaminates are summarised in Table 2.1.

Table 2.1 *ALD ZnO single thin film and Al_2O_3/ZnO nanolaminate synthesis.*

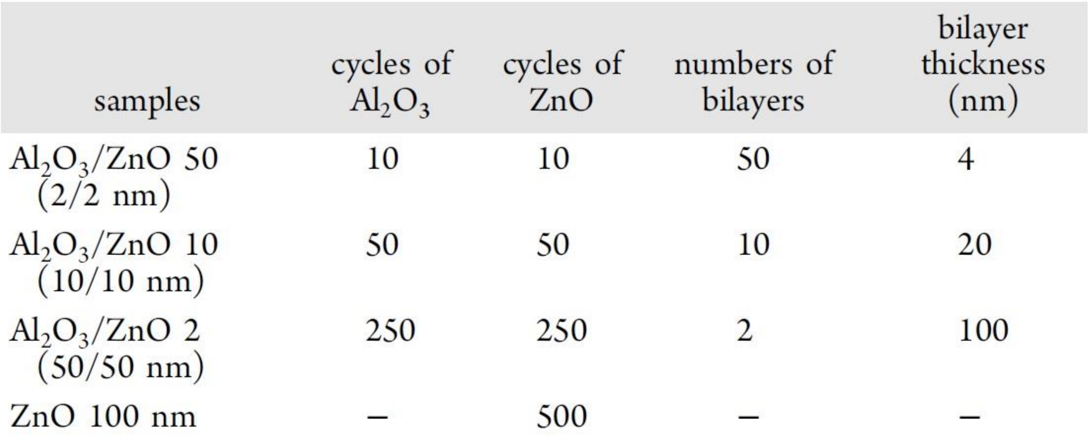

samples	cycles of Al_2O_3	cycles of ZnO	numbers of bilayers	bilayer thickness (nm)
Al_2O_3/ZnO 50 (2/2 nm)	10	10	50	4
Al_2O_3/ZnO 10 (10/10 nm)	50	50	10	20
Al_2O_3/ZnO 2 (50/50 nm)	250	250	2	100
ZnO 100 nm	–	500	–	–

2.4 Structural properties of Al_2O_3/ZnO nanolaminates

The structure of nanolaminates was characterized by scanning electron microscopy (SEM; Hitachi S-4800 microscope), energy-dispersive X-ray spectroscopy (EDX) and grazing incidence X-ray diffraction (GIXRD; Bruker D5000). The thicknesses of ZnO and Al_2O_3 layers were measured using SEM and ellipsometry technique.

2.4.1 EDX and GIXRD of Al_2O_3/ZnO nanolaminates

The EDX and GIXRD patterns (Fig. 2.1 a,b) of Al_2O_3/ZnO 10 (10/10 nm) consisting of alternating ZnO and Al_2O_3 films grown at 100 °C by ALD showed the presence of Al, Zn. The Al_2O_3/ZnO 50 (2/2 nm) nanolaminates with the thinnest bilayer thickness showed weak broad X-ray diffraction peak at 34.26° which can result from their amorphous structure or their crystalline size below 2 nm [52]. An increase of the bilayer thickness in the nanolaminates, Al_2O_3/ZnO 10 (10/10 nm), led to the appearance of XRD peaks at $2\theta = 31.82°$ and 34.35° and a weak peak at $2\theta = 36.1°$. It correspond to (100), (002), and (101) reflections of ZnO, respectively. For thicker bilayer thickness, Al_2O_3/ZnO 2 (50/50 nm), strong peaks at $2\theta = 31.74°$ and 34.35° have been observed.

The XRD peak at 36.1− 36.2° appeared in both spectra for thick bilayers in the nanolaminates, but with rather low intensity. A change in the preferential growth orientation (strong (002) and negligible (101) XRD peaks) was observed in the thicker nanolaminate Al_2O_3/ZnO 2 (50/50 nm) comparing to the single ZnO film (100 nm). No peaks related to Al_2O_3 were observed. From these XRD spectra, lattice constants and *d*-spacing between the atomic planes

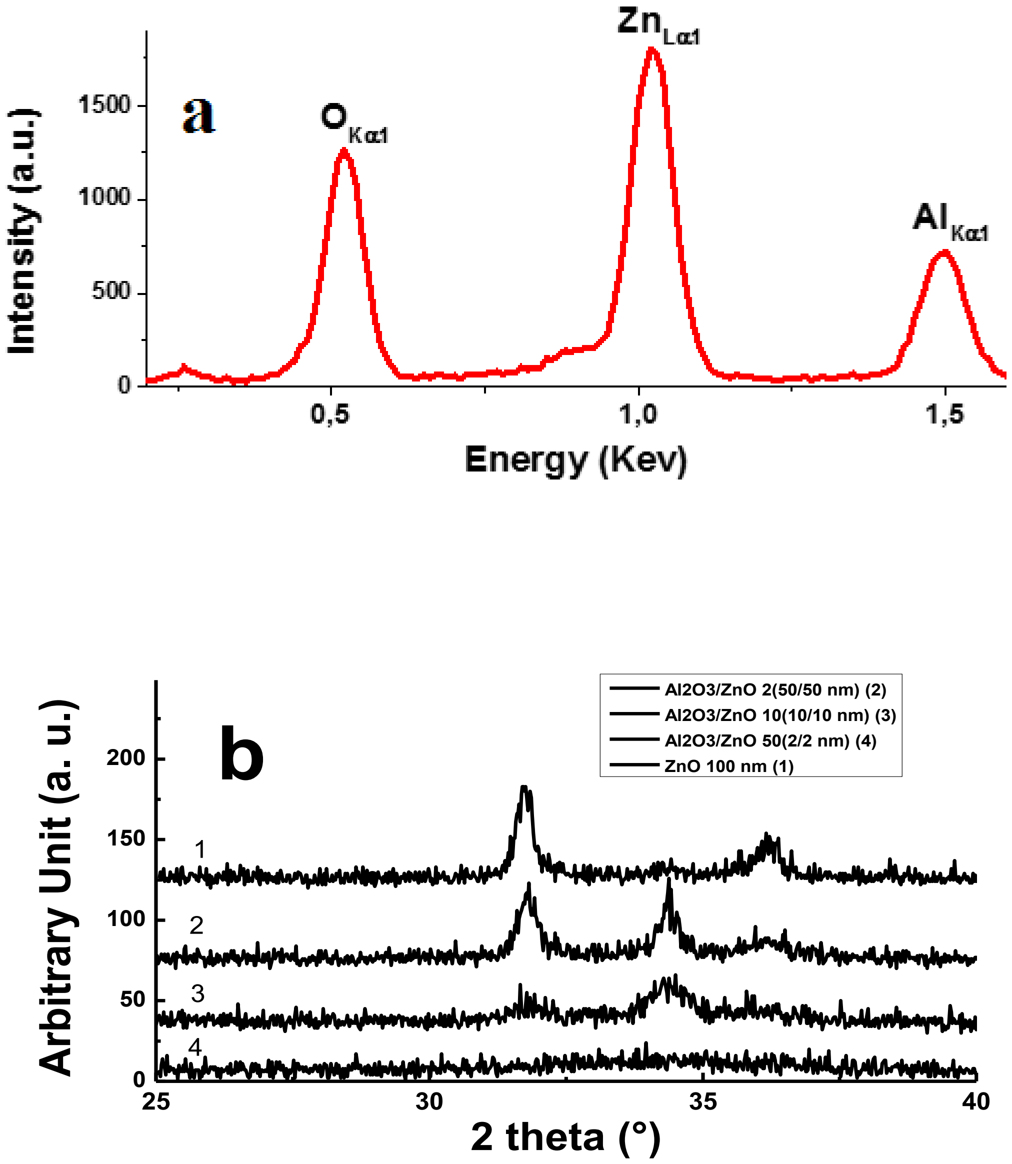

Fig. 2.1 *EDX of Al_2O_3/ZnO nanolaminates (a) and GIXRD of ZnO thin film (b) of 100 nm thickness and Al_2O_3/ZnO nanolaminates with different sequences.*

for ZnO single films and Al_2O_3/ZnO nanolaminates with different sequences were calculated. The lattice constant (a) increased when the bilayers thickness in the nanolaminates enhanced, whereas the lattice constant (c) decreased at the same time. The lattice constant (a) was lower than the similar value for ZnO (i.e., 100 nm thick), but the lattice constant (c) was higher than for ZnO (i.e., 100 nm). As a result, for Al_2O_3/ZnO 2 (50/50 nm) and Al_2O_3/ZnO 10 (10/10 nm). The *d*-spacing (100) is lower than for ZnO single layer (i.e., 100 nm), whereas for the *d*-spacing (002), it is a bit higher than for ZnO single layer. It has to be noted that the *d*-spacing (101) was lower for Al_2O_3/ZnO 2 (50/ 50 nm) and Al_2O_3/ZnO 10 (10/10 nm) than for ZnO i.e., 100 nm thick [53].

Texture coefficients (TC) calculated for the nanolaminates samples with different sequences, according Marquez et al. [53] match the preferred growth orientation in the (002) direction. In thicker bilayers (Al_2O_3/ZnO 2 (50/50 nm)) the lateral growth in (100) direction was observed (TC = 1.28). Grain size was estimated for thick bilayers Al_2O_3/ZnO 10 (10/10 nm) and Al_2O_3/ZnO 2 (50/50 nm) using Scherer’s equation [54, 55]:

$$D = \frac{0.9 \cdot \lambda}{\beta \cos(\theta)} \qquad (2.1)$$

where λ, β, and θ are X-ray wavelength, full width at half- maximum (fwhm), and diffraction angle, respectively. The grain size of Al_2O_3/ZnO 50 (2/2 nm) nanolaminates has been estimated from TEM measurement reported elsewhere [56]. The obtained grain size values were ~2.7, and 14 nm for Al_2O_3/ZnO 50 (2/2 nm), Al_2O_3/ZnO 10 (10/10 nm), and Al_2O_3/ZnO 2 (50/50 nm), respectively.

From these observations, it was concluded that in the first stage, vertical growth of ZnO on amorphous Al_2O_3 is initiated. At low bilayer thickness Al_2O_3/ZnO 50 (2/2 nm), wurzite ZnO with low crystalline quality was observed. The lattice parameter (c) increased, matching possible interstitial Al incorporation in ZnO structure at least at the interface between ZnO and Al_2O_3. [57] The thickness of doped ZnO layer might be in the range of 0.1−1 nm as the increase of the bilayer thickness from 4 to 100 nm in the nanolaminates turned back the lattice constants of the ZnO to the values which characterize single ZnO film.

2.4.2 Surface morphology of Al_2O_3/ZnO nanolaminates

Surface morphology of the Al_2O_3/ZnO nanolaminates was studied using the AFM technique. Samples with low bilayer thickness Al_2O_3/ZnO 50 (2/2 nm) and Al_2O_3/ZnO 10 (10/10 nm) showed smooth surface with insignificant surface roughness. Well-shaped hill-shaped features with average lateral dimensions 50−100 nm have been observed on the Al_2O_3/ZnO (50/50 nm) sample surface. The mean square roughness, calculated from AFM data, showed linear behaviour then thickness of bilayer increased (Figure 2.2). The obtained results are in agreement with that published in.[58] Al_2O_3 layer blocks the ZnO crystal growth and forces the ZnO to renucleate on the Al_2O_3 surface.

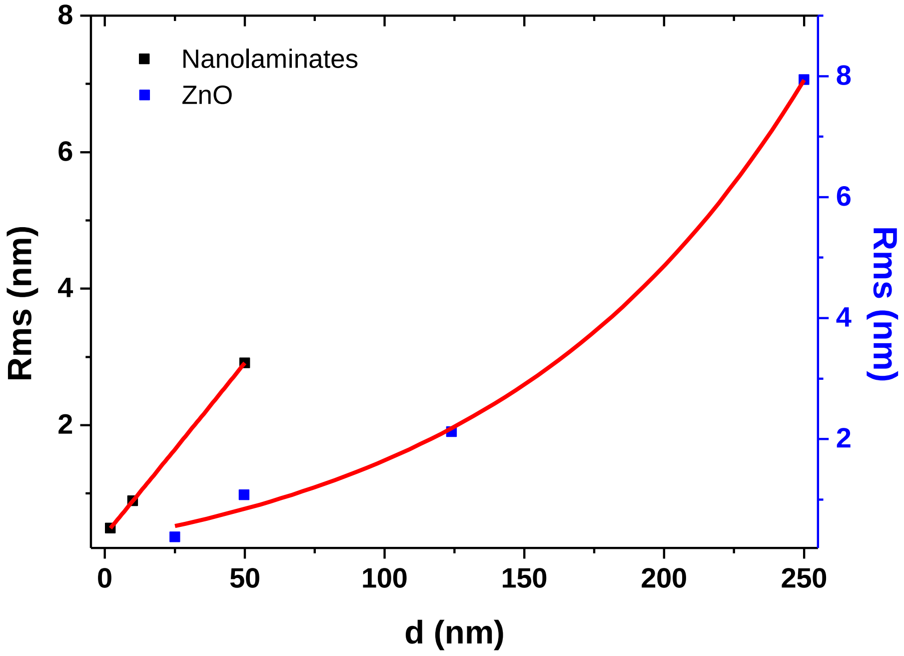

Fig. 2.2 *Blue squares show roughness vs. film thickness dependence for single ZnO layer; black squares show roughness vs. thickness dependence for top ZnO layer in the Al_2O_3/ZnO nanolaminates.*

It has to be note that surface roughness of nanolaminates was lower than that for 200 nm thick ZnO [59]. The results based on AFM measurements are in good agreement with those obtained by TIRE-based analysis.

Texture coefficients (TC) calculated for the nanolaminates samples with different sequences, according Marquez et al.[54] match the preferred growth orientation in the (002) direction. In thicker bilayers (Al_2O_3/ZnO 2 (50/50 nm)), lateral growth in the (100) direction was observed (TC = 1.28). Grain size was estimated from the Scherer equation for thick bilayers thicknesses Al_2O_3/ZnO 10 (10/10 nm) and Al_2O_3/ZnO 2 (50/50 nm) [55, 56].

2.4.3 SEM imaging of Al_2O_3/ZnO nanolaminate

Figure 2.3 shows cross-sectional SEM images of ZnO thin film of 100 nm thickness (a) and two illustrative examples of Al_2O_3/ZnO nanolaminates with different sequences. The SEM images indicate a conformal coating by ALD of the Si substrate in both cases. The SEM cross section proves as well that the sequence of alternating Al_2O_3 and ZnO interlayers was achieved throughout the total film thickness of the nanolaminates. In all nanolaminates, the first

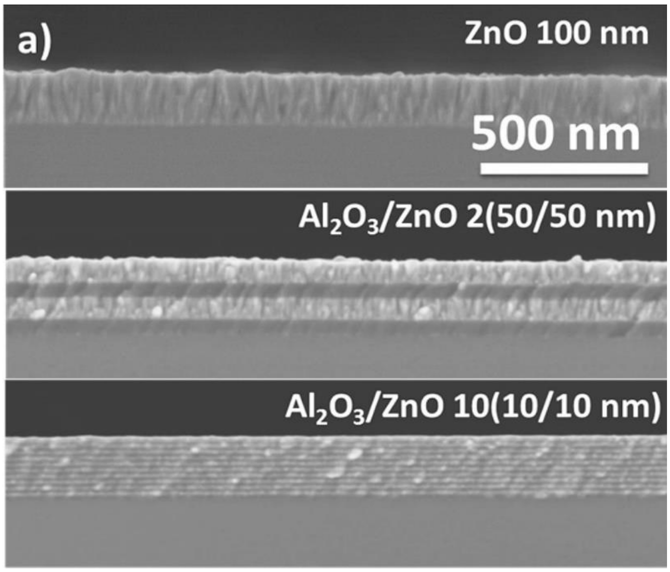

Fig. 2.3 *SEM images of ZnO thin film of 100 nm thickness and Al_2O_3/ZnO nanolaminates with different sequences.*

layer on Si substrate was Al_2O_3, and the top layer of the nanolaminate was ZnO. The SEM images show that the single layer of ZnO developed a rough surface with columnar structure and the nanolaminates consist of alternating layers of amorphous Al_2O_3 and nanocrystalline ZnO [57,60]. The growth rates of Al_2O_3 and ZnO in the nanolaminates vary from 1.4 to 2 Å per cycle and 1.8 to 2 Å per cycle, respectively, as it has been determined elsewhere [57].

2.5 Measurement technique

AFM imaging. The surface morphology of Au layers was characterized by atomic force microscopy (AFM), Scanning Probe Microscope Bioscope II Veeco (Santa Barbara, USA) and profilometer DEKTAK 32 Veeco (Santa Barbara, USA). The taping mode was used for imaging of biological recognition layers as the most suitable mode for imaging of soft biological samples. The soft MicroMash silicon probes CSC17/AIBS with nominal elasticity constant of 0.5 N/m and nominal curvature radius of 7 nm were used. AFM imaging and measurements were performed according to protocol performed in liquid environment published [61]. The surface morphology of Al_2O_3/ZnO nanolaminates was studied by Asylum Research MFP-3D atomic force microscope, operating in tapping mode and equipped with a commercial silicon tip. The size of the AFM images was 3 μm × 3 μm.

Spectroscopic ellipsometry. The experimental setup used for investigations of antibody and antigen *gp*51 interaction consisted of a spectral ellipsometer SOPRA GES-5 (see Fig.2.4 left) with rotating polarizer and 70° BK7 glass prism connected with a glass-slide by the fluid matching the refraction index (Cargille, USA). The glass-slide covered with the gold-film was fixed into a custom-made cell (Figure 2.4 right) filled with buffer solution of pH 4.5 or pH 7.4. The radius and thickness of the glass-slide was 7 mm and 1 mm respectively. The BK7 glass-slides with 48 nm thick polycrystalline Au films with 1.5 nm thick chromium underlayer exhibiting the same surface roughness were obtained from XanTec bioanalytics GmbH (Duesseldorf, Germany) and were used as substrates for further investigations. The TIRE measurements were performed in the spectral range from 400 nm to 850 nm. The optical constants of Au films for each sample were determined from the analysis of the TIRE data. The schematic diagram of TIRE experimental set-up for BVL antigen-antibody interaction investigations is presented in Figure 2.5.

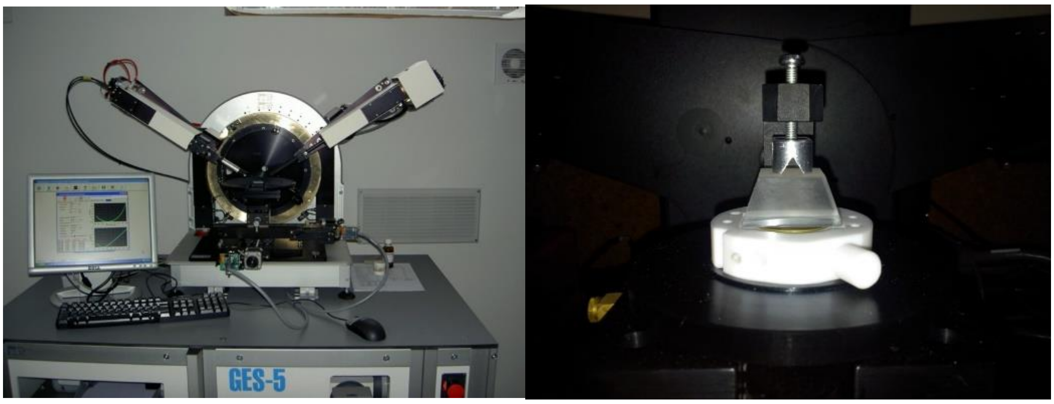

Fig. 2.4 *Outside view of SOPRA GES-5 ellipsometer (left) and custom-made cell for protein-protein interaction in-situ investigation (right).*

During the TIRE measurements all steps of binding were recorded by injecting solutions in the cell with a syringe pump. The experimental ellipsometric data was analyzed by “SOPRA Winelli” data acquisition program Sopra (Paris, France).

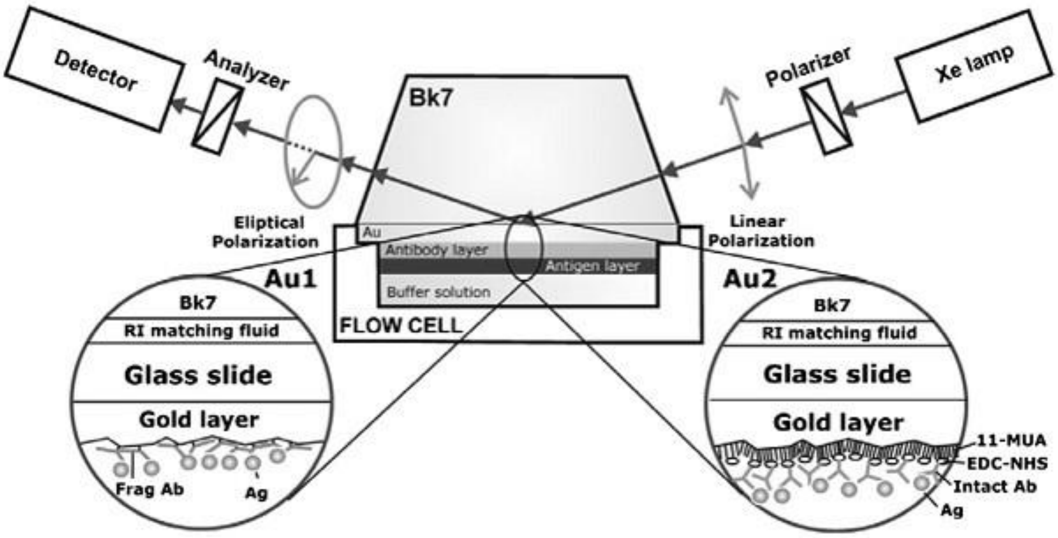

Fig. 2.5. *The schematic diagram of TIRE experimental set-up; PMT – photomultiplier tube, BK7 – glass prism, 11-MUA – SAM of mercaptoundecanoic acid, EDC-NH-antibody linking groups that were formed by the EDC/NHS activation, frag-Ab fragmented antibody based layer, intact-Ab – intact antibody based layer, Ag – antigen involved in the formation of the Ab–Ag complex.*

For the investigations of monomeric and dimeric GCSF interaction with its receptor the experimental setup presented in Figure 2.6 and Figure 2.7 was used. It was based on a spectral ellipsometer M-2000X, J.A.Woollam (USA) with a rotating compensator. Glass prism BK7 70°(deg.) connected via the refraction index matching fluid (Cargille, USA) with a 1 mm thickness BK7 glass slide covered by a layer of Cr–Au from XanTec bioanalytics GmbH (Duesseldorf, Germany) was installed into the optical pathway of ellipsometer. The prism with the gold film was placed into a custom cell made from Teflon and filled with buffer solution of PBS.

Fig. 2.6 *The outside view of spectral ellipsometer M-2000X, J.A.Woollam*

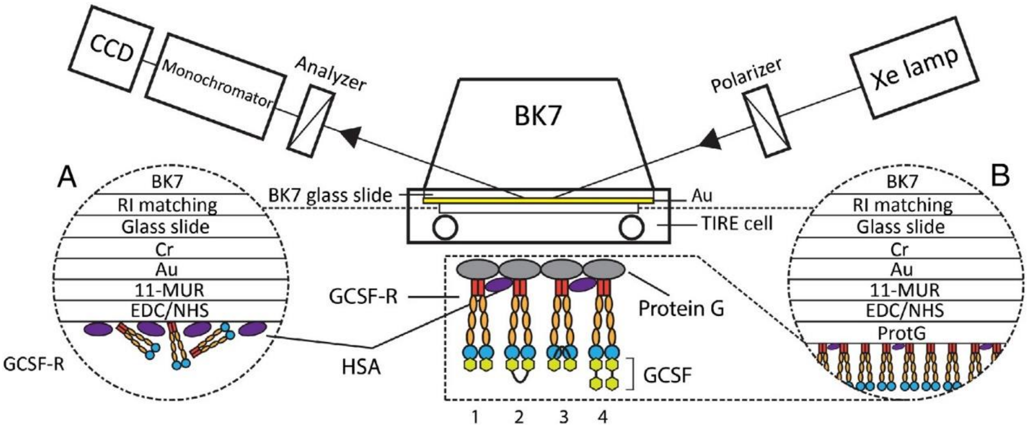

Fig. 2.7 *The schematic diagram of TIRE experimental setup used for monomeric and dimeric GCSF interaction with its receptor investigation.*

Two samples of thin gold films A and B with very similar values of layer thickness and surface roughness were used for further immobilization of protein biomolecules. Both gold layers under investigation were polycrystalline. The thickness and surface roughness of the gold layers were measured by using scanning probe microscope D3100, Nanoscope IVa

(Veeco). The layer thickness and root mean square (RMS) values of surface roughness for both samples was d = 47.6 ± 0.3 nm, RMS = 0.7 ± 0.3 nm and d = 48.7 ± 0.3 nm, RMS = 0.9 ± 0.3 nm, respectively. The optical constants of gold films for both samples were determined from the analysis of TIRE data and layers thicknesses were fixed parameters during fitting procedure. The B-Spline function was used to evaluate the optical constants of gold.

The results were compared with the data presented in [62,63]. The contribution of surface roughness (RMS ≈ 0.7–0.9 nm) was taken into account in the calculations of ellipsometric parameters Ψ (λ) and Δ (λ) in order to develop an adequate model [64]. The TIRE measurements were performed in the spectral range of 300 nm to 1000 nm and experimental ellipsometric data was analysed by J.A. Woollam Co., Inc., data acquisition program “Complete Ease”.

CHAPTER 3

3.1 Evaluation of intact and fragmented antibody based BLV immunosensors by total internal reflection ellipsometry (TIRE)

Introduction. Proper immobilization of antibody on solid–liquid interfaces plays an important role in the development of immunosensors [64]. The sensitivity of immunosensor depends on the surface concentration of immobilized antibodies, their remaining antigen binding ability and appropriate site specific orientation of these molecules on the substrate. The main advantage of properly oriented antibody based immunosensors is good steric accessibility of binding sites for analyte molecules and it leads to higher binding efficiency. The covalent attachment of intact antibodies or their fragments on the substrate surface using a number of intermediate linking layers including lipid layers, organosilanes, plasma polymerized films, thiol based monolayers polymer matrices has been investigated [65,66,67]. The selection of the optimal antibody immobilization method strongly depends on the presence and location of functional groups (mainly $–NH_2$ and $–COOH$) suitable for immobilization. The main immobilization strategy is based on formation of covalent bonds with the lysine residues that are randomly distributed in the antibody molecule.

Unfortunately, some cases of immobilization of intact antibodies usually result in a random orientation of these molecules on the sensing surface. Antigen binding sites of some of the immobilized antibodies can face towards the immobilization substrate; therefore not all of them are accessible for antigen molecules. A significant decrease in antigen binding activity was registered as a result of random antibody immobilization on the sensor surface [68,69,70]. The immobilization strategy also affects the specific antigen binding constants because the apparent affinity constants depend on the orientation of biomolecules on the surface of solid support [71]. Proper orientation of antibodies is preferable to increase the sensitivity of immunosensors, therefore oriented immobilization of antibody fragments was proposed as a possible way to overcome this problem [72,73]. Oriented immobilization of fragmented antibodies does not cause substantial decrease or significant distribution of the apparent affinity constants constants. Application of fragmented antibodies reduces random orientation of antibodies on the transducer surface, consequently increasing the antibody–antigen binding capacity [69,74,75]. Moreover, high operational stability of gold electrodes modified by fragmented antibodies makes them very attractive and applicable for immunoanalytical purposes [74, 76].

In order to better understand biological recognition layers based on intact and fragmented antibodies, total internal reflection ellipsometry (TIRE) studies are particularly interesting. These measurements represent the spectroscopic ellipsometry carried out in conditions of total internal reflection, which is enhanced by SPR [77]. It was shown that TIRE is suitable for the precise analysis of protein based structures and monitoring of kinetic parameters of protein binding to surfaces [78].

In this section the characterization of fragmented antibodies against BVL surface layer by the spectroscopic ellipsometry is presented.

3.1.1 Preparation and characterization of intact and fragmented antibody layers.

Two types of sample used for investigation of BLV imunosensor effectiveness evaluation were designed. First type (sample Au_1) was prepared by direct immobilization of frag-Ab onto Au thin film surface. Second type (sample Au_2) was prepared by indirect immobilization via 11-MUA self-assembled monolayer of mercaptoundecanoic acid and EDC-NH antibody linking group’s layer that were formed by the EDC/NHS activation.

3.1.2 AMF images of Au films

Before the immobilization of protein layer the investigation of optical properties and surface roughness of the Au film was performed. The morphology studies have shown that the surface roughness of Au layers prepared by magnetron sputtering was quite similar for both Au modified substrates used for preparation of samples Au$_1$ and Au$_2$. The RMS values (root mean square) of surface roughness were 0.5 nm and 0.4 nm with peak values of 2.3 nm and 2.0 nm for Au$_1$ and Au$_2$, respectively. According to the profilometric data, the thicknesses of Au layers over the substrates used for Au$_1$ and Au$_2$ were 45.4 nm and 47.9 nm, correspondingly. The AFM studies of nanostructure have shown that Au layers consisted of the same crystallites of ~20 nm size in both samples (see Figure 3.1 A).

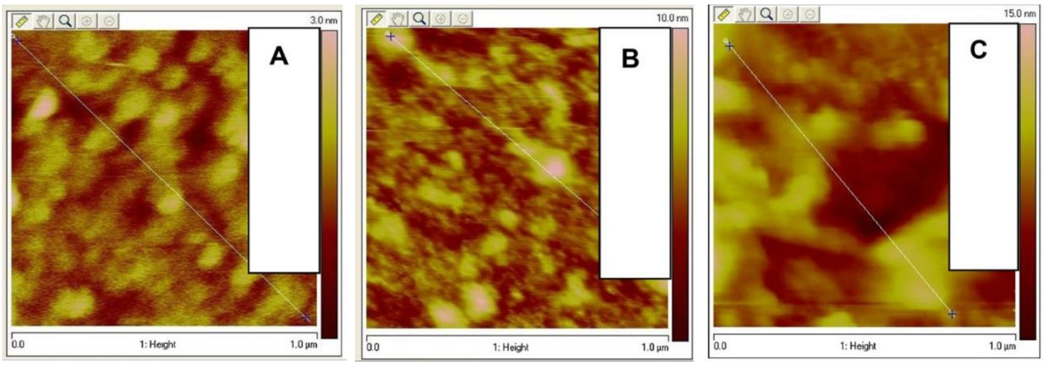

Fig. 3.1 *The AFM images: pure gold layer (d = 48 nm) on BK7 glass substrate (A), gold layer (d = 48 nm) modified with fragmented antibodies (B), gold layer (d= 48 nm) modified with 11-MUA/EDC-NHS/intact antibodies (C). All AFM measurements were performed in PBS, pH 7.4.*

3.1.3 Modification of gold film with reduced antibody fragments

To form the fragmented antibody layer (sample Au$_1$) the frag-Ab (0.44 mg/ml) dissolved in the PBS (pH 7.4) were injected into the cell with fixed BK7 glass substrate with deposited Au layer. The kinetics of fragmented antibody binding reaction via –SH group to the gold surface was recorded for 25 min. at fixed wavelength (*λ*). Spectra of ellipsometric parameters *Δ* (λ) and *Ψ* (λ) before and after the immobilization of frag-Ab and after the following interaction of immobilized frag-Ab with *gp*51 antigens present in 0.5 mg/ml solution were measured (see Figure 3.2).

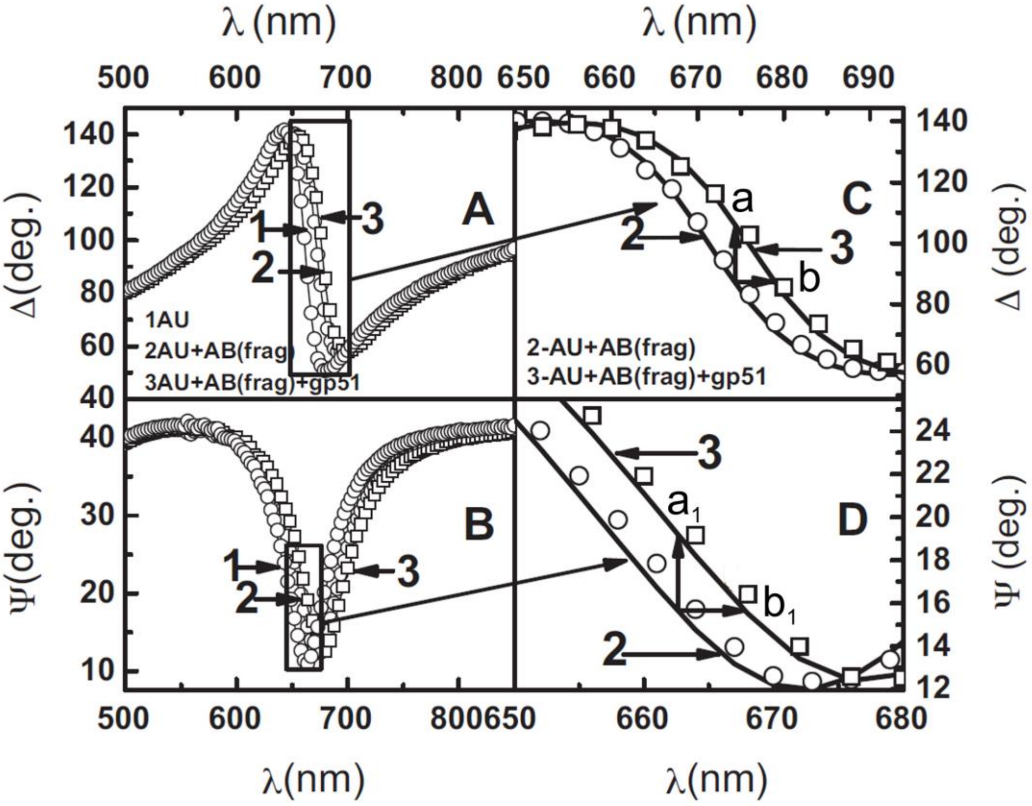

Fig. 3.2 *Spectra of ellipsometric parameters Δ(λ) (A and C) and Ψ(λ) (B and D) of the sample* Au_1*. 1 – Au layer; 2 – Au layer after the modification by fragmented antibodies; 3 – Au layer modified by fragmented antibodies after the specific interaction with antigen. The image (C) is an enlarged part of image (A) indicated by rectangle; the image (D) is enlarged part of image (B) indicated by a rectangle.*

Each experiment was repeated four times and the average values of parameters were calculated. In all experimental runs the spectral shift to higher wavelengths was 10 nm and deviation from average shift value was less than 1 nm.

3.1.4 Modification of gold film with self-assembled monolayer and covalent immobilization of intact antibodies

A self-assembled monolayer (SAM) of 11-mercaptoundecanoic acid molecules was formed on the surface of Au deposited over the BK7 glass substrate (sample Au_2). The sensor disk was incubated in 1 mM of MUA dissolved in ethanol at a room temperature for 18 h. For covalent immobilization of intact antibodies, activation of the SAM using a mixture of 0.1 M of EDC and 0.1 M of NHS in water was performed. During this

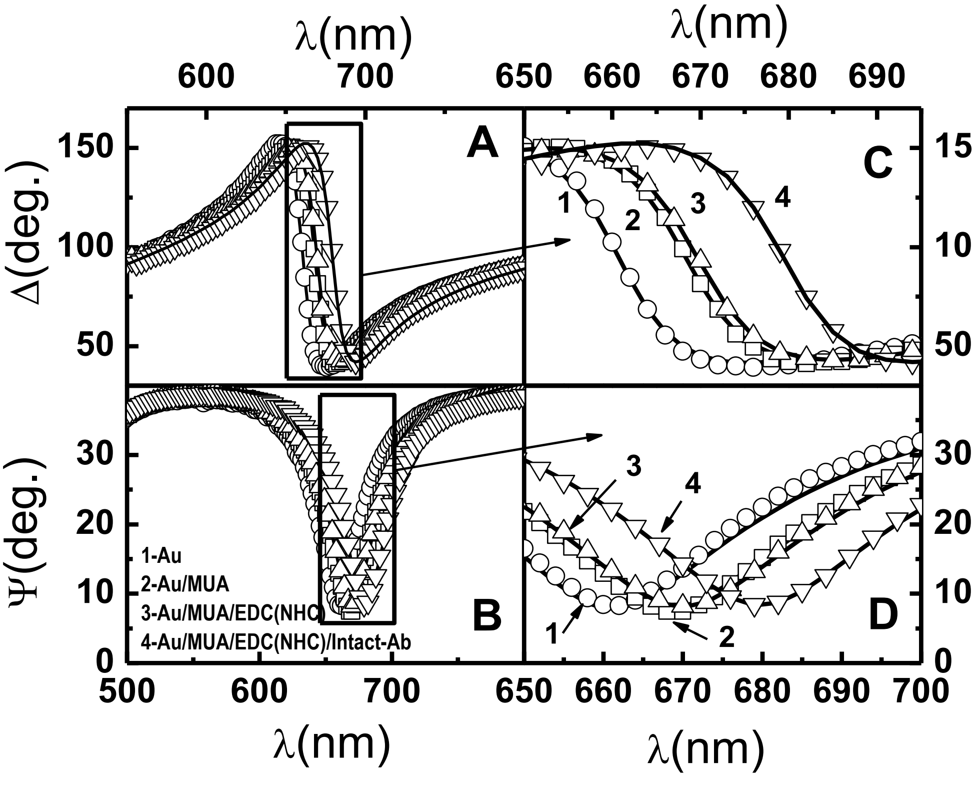

Fig. 3.3 *Spectra of ellipsometric parameters Δ(λ) (A) and Ψ(λ) (B) of the sample* Au_2. *1 – Au layer; 2 – Au layer after the modification by 11-MUA; 3 – 11-MUA modified Au layer after treatment by EDC/NHS; 4 – the same layer as in the previous plot (3) after the modification by intact-antibodies. The image (C) is an enlarged part of image (A) indicated by rectangle; the image (D) is enlarged part of image (B) indicated by a rectangle.*

procedure functionally active NHS esters were obtained by the reaction of MUA carboxyl groups with a mixture of EDC and NHS. The ellipsometric spectra were recorded and optical constants of self-assembled monolayer before and after the activation were estimated (Figure 3.3). Injection of 0.44 mg/ml antibody solution into the cell formed an antibody layer consisting of intact antibodies and optical properties of this layer were determined.

Analyte detection was performed as a last step of surface modification. It was performed by the injection of bovine leukaemia virus antigen *gp*51 solution (0.5 mg/ml). Due to immobilized antibody interaction with antigen *gp*51 and formation of corresponding complex changes in refractive index of protein based layer were registered. These changes were evaluated as an influence of additionally formed antigen layer. Antibody-antigen interaction kinetics was estimated from changes of ellipsometric parameters Δ (λ) and Ψ (λ). In addition ellipsometric spectra of the formed layer were measured. During all TIRE experiments the washing was performed in the cell by the injection of washing buffer described below. Buffer solutions from pH 7.4 to pH 4.5 were tested, due to optimization of antibody-antigen interaction in both cases. The same pH solutions were used for the surface washing procedure.

3.1.5 The roughness of gold layers modified by fragmented and intact antibodies layers

The roughness of differently modified gold layers was estimated by the calculation of root mean square of height values (RMS). The RMS of pure gold layer, gold modified by fragmented antibodies and gold modified by intact antibodies were 0.33 nm, 1.55 nm and 2.95 nm, respectively. The AFM data clearly showed that the RMS values of gold surface modified by intact and fragmented antibodies are different: the RMS value for the sample based on intact antibodies was approximately two times larger in comparison to that of frag-Ab. The surface profile of pure gold (curve 1), gold modified with fragmented antibodies (curve 2) and with intact antibodies (curve 3) is presented in Figure 3.4.

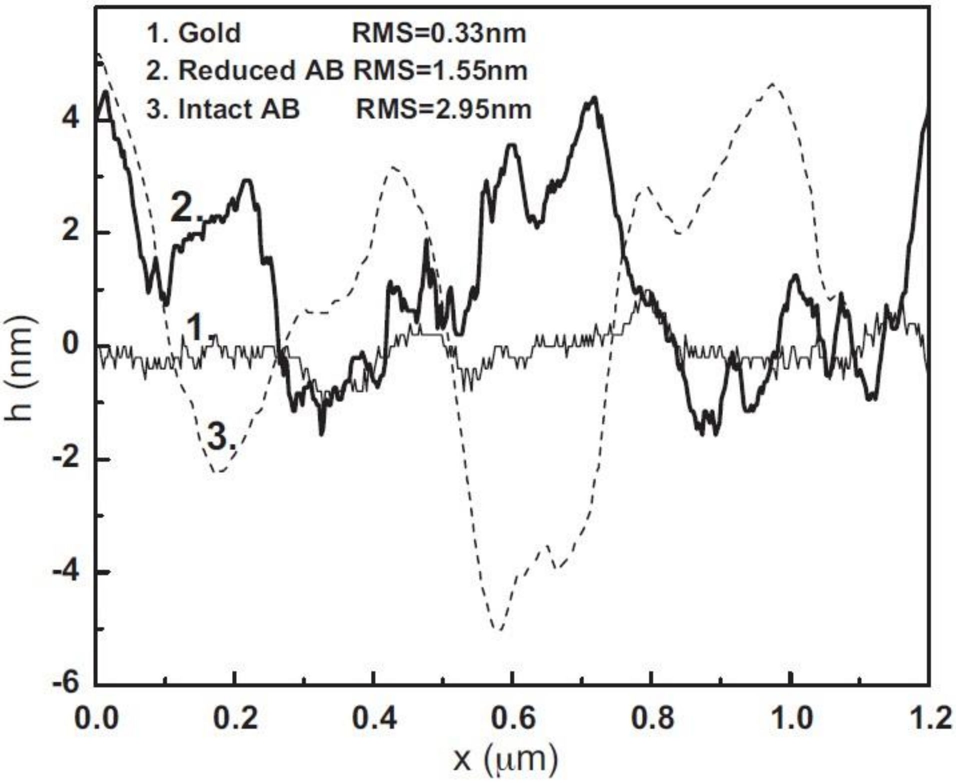

Fig. 3.4 *The surface profile of pure gold (curve 1), gold modified with fragmented antibodies (curve 2) and with intact antibodies (curve 3) in buffer solution.*

3.1.6 Characterization of formed layers, development of multi-layer model

The TIRE measurements have shown that the surface plasmon waves were excited at an external angle of incidence equal to 70° for both samples. In the SPR spectra the dip was observed correspondingly at 661 nm and 670 nm for pure gold in PBS (pH 7.4). The TIRE data was analysed by applying the multilayer-model. For both samples surface of gold layer was accepted as a surface layer due to measurable thickness of this layer. The effective media approximation (EMA) was used to model the contribution of surface roughness

[79] to the optical response of real surfaces. The thickness of the surface layer was assumed to be equal to the RMS values determined from the AFM studies. The Bruggeman's EMA model was applied for considering the proportion of Au and other materials in this layer. Fitting of TIRE results indicated that the calculated surface layers consisted: (i) of frag-Ab and Au at a ratio of 1:9 for Au1 sample (Figure 3.5, curve 2), and (ii) of 11-MUA and Au at a ratio of 1:2 for Au$_2$ sample (Figure 3.5, curve 4).

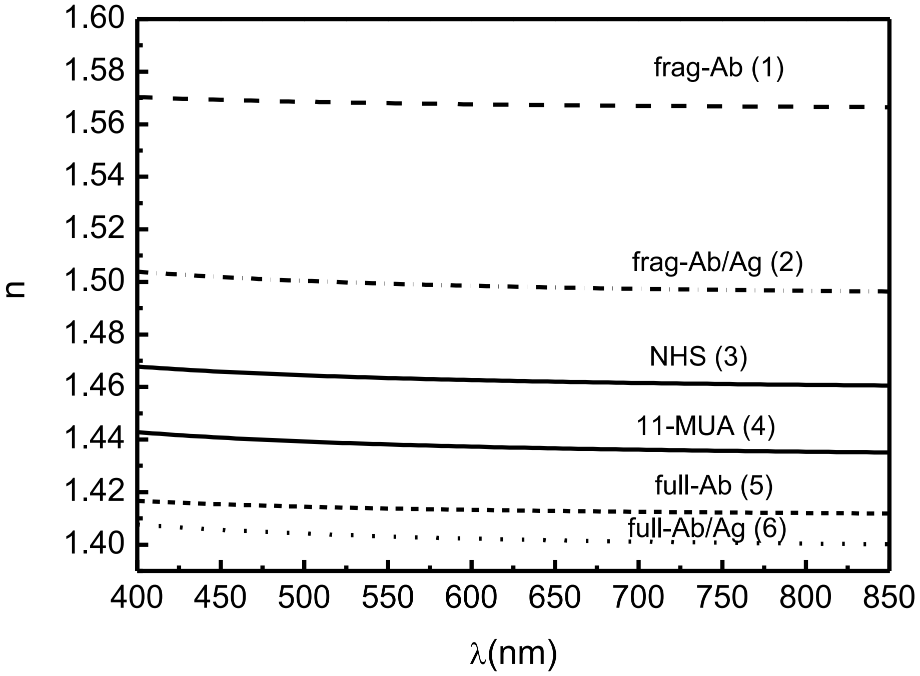

Fig. 3.5 *The spectra of refraction indexes of following layers: 1–Au layer modified by frag-Ab, 2–Au layer modified by frag-Ab after treatment with antigen (frag-Ab/Ag), 3–11-MUA modified Au layer after treatment by NHS-EDC, 4–Au layer after the modification by 11-MUA, 5–11-MUA modified Au layer after the covalent immobilization of intact-Ab and 6 – the same layer as in the previous plot (5) after treatment with antigen (intact-Ab/Ag).*

The thickness of 2 nm Cr-based under layer used to achieve a better adhesion between the glass substrate and Au-based layer was also taken into account in the evaluation of TIRE results presented in Figure 3.2, curve 1 and Figure 3.3, curve 1. Our previously published results [63, 64] illustrate that the application of surface layer in the multilayer model is very useful to obtain an adequate model to describe bonding between biomaterials and gold surface. As it is noted above the multilayer model was used for analysis of all formed structures. Estimated thickness of each monolayer in most cases was equal to the dimension (length) of molecules forming this layer and it was used as a fixed parameter in the regression analysis. This assumption allows calculation of the dispersion curves through the fitting procedure. Obtained dispersion curves were independent from the thickness of the monolayer. The calculated refractive index depends only on the surface concentration of molecules immobilized on the surface [80], as it is presented in Figure 3.5. Applied multilayer model was well suited to describe real experimental data with mean square error (MSE) of ∼1.5 to 6.7×10^{-3} for all investigated layers.

3.1.7 Evaluation of biological recognition layer based on fragmented antibodies

The surface modified with reduced antibody fragments (Au_1 sample) before and after interaction with antigen was investigated (Figure 3.2, curve 3). The width of the intact antibody is 14.5 nm, with antigen binding sites separated by 13.7 nm [81]. Therefore, after the reduction the width of the fragmented antibody might become lower than 7.25 nm. According to our best knowledge it is still poorly addressed in the scientific literature how the immobilization process might affect the distance of antigen binding sites from the surface. The regression analysis has shown that the calculated spectra for the fragmented antibody layer are well fitting with the TIRE data only when the thickness of the layer is rather close to the dimensions of fragmented antibodies (d = 4 nm). So, the value of the layer thickness could carry the information about the distance of antigen binding site from the surface if an appropriate model is applied. The thickness d = 4 nm was a fixed parameter during the fitting of results, thus all changes in the binding layer were related to changes in the refractive index, which was a function of the surface concentration of the materials deposited on the surface. Cauchy dispersion function was used to describe all organic material based layers investigated in this experiment [82]. Obtained values of refractive index for fragmented antibodies were close to those found in the literature for bovine serum albumin and γ-globulin [83]. The values A = 1.565, B = 7.867×10^{-3} μm^2 were determined from regression analysis applied for the fragmented antibody monolayer (Figure 3.5, curve 1). From the obtained dispersion curve the 0.24 $\mu g/cm^2$ surface concentration of immobilized fragmented antibodies was calculated. Accordingly, it was assumed that fragmented antibodies covered about 98% of the sensing surface, thus a very efficient sensor surface could be created by methodology based on the application of fragmented antibodies. Multilayer model used in this study shows that the distance between the fragmented antibody active sites and gold surface after the immobilization process is less than theoretical dimension of fragmented antibodies. Moreover, in other studies similar theoretical physical dimensions [75] or molecular weight values [74] of fragmented antibodies were used.

During the next step of data evaluation the antigen layer was analysed by fitting of the experimental curves of Δ (λ) and Ψ (λ) parameters. The regression analysis has shown that the calculated spectra of the antigen layer could be fitted well when the thickness of the layer is close to the dimensions of the antigen molecule (3 nm×3.5 nm×4 nm) [84]. Moreover, fitted dispersion curve is close to the ellipsometry [84] and refractometry [85] data obtained by other authors. During regression analysis the thickness of the layer (d = 3.5 nm) was fixed while the parameters A and B in Cauchy function were used as free values. The calculated values of the dispersion curve were A = 1.494, B = 1.550×10^{-3} µm2 for the antigen layer and the resulting antigen surface concentration was 0.12 $\mu g/cm^2$. Estimated sensitivity of parameters (Δ (λ) and Ψ (λ)) that were measured before (Figure 3.2 C and D, curve 2) and after (Figure 3.2 C and D, curves 3) the immobilized fragmented antibody interaction with antigen was evaluated (see Figure 3.2 C and D): (sensitivity of Δ) = a/b = 18.6/4.57 = 4.07; (sensitivity of Ψ) = a_1/b_1 = 3.54/5.11 = 0.69. It was found that by the measurement of Δ (λ) a 5.89 times higher sensitivity could have been achieved, since the sensitivity of the parameter Δ (λ) was 5.89 times higher if compared to the sensitivity of parameter Ψ (λ).

The presented investigations illustrate that the modification with fragmented antibodies seems to be a simple and reliable method to immobilize antibodies on the surface. Theoretically active sites of fragmented antibodies immobilized through the –SH groups are closer to the metal surface if compared to that of not fragmented antibodies immobilized via SAM's. Due to short distance from the metal surface some of them can be denatured. From our investigation, we can state that the distance between the metal surface and active sites of frag-Ab is closer than it was expected. Evaluation of results presented in this and the next chapter shows that frag-Ab modified surfaces more efficiently interact with antigens in comparison with that modified by intact-Ab.

3.1.8 Evaluation of biological recognition layer based on intact antibodies

The biological recognition layer based on intact antibodies was formed by the SAM based immobilization methodology. It is known that the rapid phase of chemisorption of the 11-MUA molecules occurs within ~20 min and it is followed by a slower phase of assembly reorganization, which reaches the steady-state conditions within 2 h [86]. Therefore, the incubation time (18 h) was long enough for the formation of the self-assembled monolayer (SAM) consisting of 11-MUA assembled on the surface of the Au_2 sample (Figure 3.3, curve 2). Immobilization of antibodies on the self-assembled monolayer *via* linking layer of NHS ester was performed on the Au_2 sample. The analysis of TIRE data of the Au_2 sample with the 11-MUA layer on the top of Au films has been performed by a similar fitting procedure as it is described in Section 3.1.4. It is known that the length of the 11-MUA chain is ~1.24 nm. The thiol-groups of 11-MUA molecules bind to the Au surface and the tail groups are leaning by 30° from the vertical axis [80]. Therefore, in the present analysis it was assumed that the thickness of the 11-MUA SAM was 1.1 nm.

Early some other authors [87, 88] investigated self-assembled monolayers of 11-MUA SAM and reported that SAM thickness values are slightly higher (*d* is about 1.7 nm) than that reported in our recent study. However, these investigations were performed using single wavelength ellipsometry and they did not include surface roughness as a parameter applied for calculations in the optical model. In our research we have used spectroscopic ellipsometry, which provides a possibility to separate the thickness *d* and dispersion of refraction index *n* during the regression analysis, which is not possible in single wavelength ellipsometry. Moreover, optical model applied in our research includes surface roughness of gold layer. It was shown that surface roughness [80] has a significant contribution to the optical response and as a result to the determination of thickness of monolayer. Moreover, spectroscopic ellipsometry provides a possibility to obtain more precise values of thickness *d* and optical constants in comparison with single wavelength ellipsometry. These calculated values of optical constants ($A = 1.433$, $B = 1.589\times10^{-3}$ μm^2) of the SAM based on the 11-MUA is very close to SAMs investigated by other authors [80, 89, 90].

The TIRE spectrum of 11-MUA after the treatment with the EDC/NHS (Figure 3.3, curve 3) was also fitted. As noted above, several assumptions have been accepted: by considering length of the chemical bonds in NHS ester was assume that the dimension of the NHS ester molecule is close to 0.5 nm, so this value defines the thickness of 11-MUA monolayer, which is activated by the NHS ester. The parameters A and B in Cauchy function of refraction index were used as free parameters. Unfortunately, the knowledge about optical properties of the NHS ester is limited. To overcome this lack of scientific knowledge the regression analysis of optical constants attributed to the additional layer formed by the treatment of 11-MUA with the NHS ester was performed. We have found that $A = 1.459$, $B = 1.488\times10^{-3}$ μm^2 (Figure 3.5, curve 3) and that the concentration of materials (11.5 mg/ml of NHS and 76.68 mg/ml of EDC) was optimal to modify almost 100% of the sensing surface.

Further, the intact antibody layer was analysed by the fitting procedure. Layer formation from these covalently immobilized antibodies was realized by injecting the same concentration of proteins (0.44 mg/ml) as in the previously described and analysed case of the fragmented antibody layer formation. In this case the regression analysis was more complicated due to uncertainty attributed to random binding of antibodies (Figure 3.3, curve 4). The dimensions of the IgG molecule are approximately 14.5 nm×8.5 nm×4 nm [82]. Results of the TIRE experimental data fitting analysis show that 0.21 $\mu g/cm^2$ surface concentration of antibodies was formed on the surface. Refractive index values obtained from the regression analysis ($A = 1.494$, $B = 1.550\times10^{-3}\ \mu m^2$) were very small (Figure 3.5, curve 5) in comparison to the values registered for the layer of fragmented antibodies (Figure 3.5, curve 2). During the regression analysis the thickness of the intact antibody layer was applied as an average value (9 nm) of antibody dimensions and it was used as a fixed parameter [91]. From the results of the regression analysis the surface concentration of intact antibodies on the surface was determined. It shows that the surface concentration of immobilized intact antibodies has a slightly smaller value than that of fragmented antibodies, 0.21 $\mu g/cm^2$ and 0.24 $\mu g/cm^2$, respectively. Expecting that intact antibodies were attached to the surface randomly [69], it is reasonable to predict that the immunoassay with fragmented antibodies that are well oriented on the sensor surface will be more sensitive for corresponding antigens as compared to the surface modified with intact antibodies.

The last step of this investigation was the determination of optical properties of randomly immobilized intact antibodies (Figure 3.5, curve 1) and the estimation of antigen binding capacity of this biological recognition layer by the evaluation of the corresponding TIRE data (Figure 3.5, curve 2). The thickness of the formed antigen layer was the same ($d = 3.5$ nm) as in the case of fragmented antibodies. The values of parameters of Cauchy dispersion function obtained from the regression analysis for antigen were $A = 1.395$, $B =$

1.552×10^{-3} μm^2 (Figure 3.5, curve 6). The regression analysis has shown that the efficiency of antigen binding (0.115 μg/cm^2) for fragmented antibodies was 2.5 times greater if compared to that (0.047 μg/cm^2) for intact antibodies (Figure 3.6). This effect is the result of random orientation of intact-Ab, while fragmented antibodies are bind to the Au surface via thiol groups in the hinge region of the antibody molecule. Thus, our experiments and calculations indicate that fragmented antibodies are more efficiently oriented on the Au surface. Moreover, in order to confirm the provided analysis and the conclusions on the orientation of antibodies the AFM investigations were carried out on the same SPR chip surface in buffer solution.

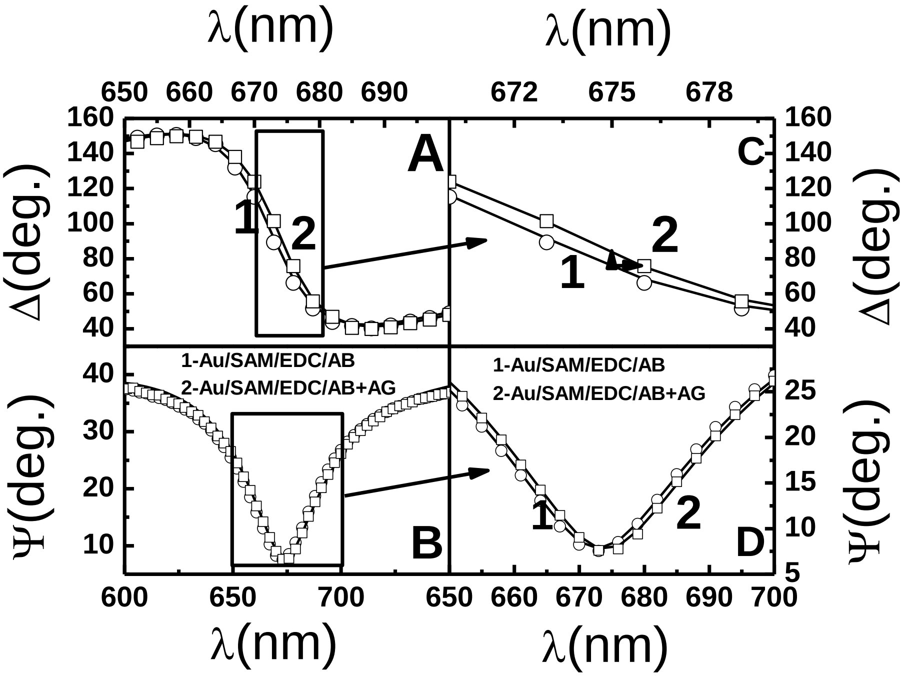

Fig. 3.6 *Spectra of ellipsometric parameters Δ (λ) (A) and Ψ (λ) (B) of the sample Au*$_2$*. 1–Au layer modified by Au/11-MUA/EDC-(NHS)/intact-Ab; 2–the same layer as in the previous plot after treatment by antigen (gp51). The image (C) is an enlarged part of image (A) indicated by rectangle; the image (D) is enlarged part of image (B) indicated by a rectangle.*

3.1.9 Application of TIRE for analysis of Ab–Ag interaction kinetics

In order to estimate the efficiency of antigen interactions with fragmented and intact antibodies the Ab–Ag complex formation kinetics was studied. It should be noted that formation kinetics of all previously discussed layers was recorded. However, in this study these steps were not evaluated in detail, since the most important interactions from the bioanalytical point of view is kinetics of the Ab–Ag complex formation. The evaluation of ellipsometric parameters *Δ* (λ) and *Ψ* (λ) was performed at a selected wavelength (λ= 670 nm for both samples), which was chosen in a such way that both *Δ* (λ) and *Ψ* (λ) varied in the linear part of ellipsometric curves, close to the SPR minimum. In Figure 3.7 evolution of the ellipsometric parameter *Δ* (λ) during the interaction period for both samples is shown, because parameter *Δ* (λ) offers better sensitivity

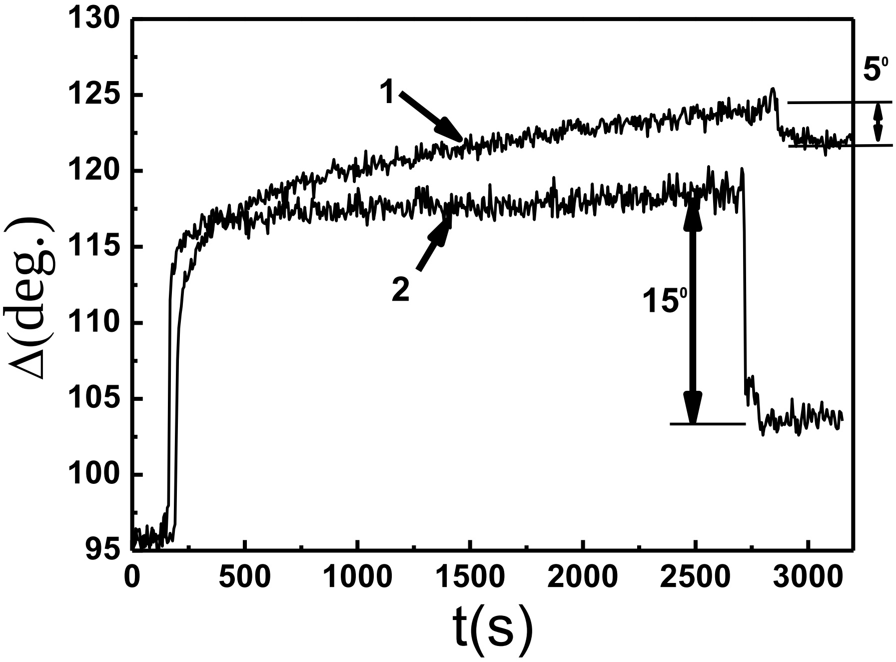

Fig. 3.7 *Interaction kinetics of immobilized fragmented antibody (1) and intact antibody (2) with antigen gp51; the ellipsometric parameter Δ (λ) vs. time is presented.*

towards the changes of the refractive index in comparison to the ellipsometric parameter $\Psi(\lambda)$ [78].

In the case of antigen interaction with the frag-Ab layer the interaction was slower at the beginning, but at the time when the interaction was interrupted the signal was higher by about 5% in comparison to the intact-Ab layer. Surprisingly, the most interesting information appeared during the washing step, which was performed with buffer (pH 4.5). In the case of the intact-Ab kinetics the Δ (λ) parameter drops down by about 15° from the initial value of 118°, meanwhile for the fragmented antibody the signal decreases just by 5° from the initial value of 124° (Figure 3.7 curve 1). For the fragmented antibody layer the signal after washing was three times higher in comparison to the intact-Ab based layer (Figure 3.7). The study of the Ab–Ag complex formation kinetics clearly shows differences in sensitivity and coating quality between the intact-Ab and frag-Ab based layers. *In-situ* measurements of antigen interaction with intact and fragmented antibody were monitored by TIRE and evaluated by the conventional Langmuir kinetic equation [92], which was applied for the determination of affinity constants. The concentration of injected antigen *gp*51 for intact and fragmented antibody cases was $c = 0.5$ mg/ml $= 9.8\times10^{-6}$ mol L^{-1}.

In the case of intact-Ab monolayer interaction with antigen *gp*51 the association and dissociation rate constants were $k_a \cdot c = 8.781\times10^{-2}$ s^{-1}; $k_d = 4.36\times10^{-3}$ s^{-1}, respectively, $k_a = 8.96\times10^{3}$ s^{-1} mol^{-1} L. As a result association and dissociation constants for antigen *gp*51 interaction with intact antibody monolayer were $K_a = 2.055\times10^{6}$ mol^{-1} L; $K_d = 4.86\times10^{-7}$ mol L^{-1}. For the antigen *gp*51 interaction with fragmented antibody monolayer the association and dissociation rate constants were $k_a \cdot c = 8.5\times10^{-2}$ s^{-1}; $k_d = 7.849\times10^{-2}$ s^{-1} and $k_a = 8.67\times10^{3}$ s^{-1} mol^{-1} L affinity constants $K_a = 1.1\times10^{5}$ mol^{-1} L; $K_d = 9\times10^{-6}$ mol L^{-1}, respectively. The values of calculated constants are of the same order as that calculated for polyclonal antibodies against some mycotoxins [93].

Conclusions: section 3.1

The analysis of TIRE parameters has shown that the immobilized frag-Ab layer can specifically interact with a 2.5 times higher amount of antigen if compared to the randomly oriented intact-Ab layer. The TIRE method has been proved to be a good and sensitive tool, which is suitable for detailed analysis of the biological recognition layer structure, including the evaluation of antibody orientation, average distance of antigen binding sites from the support surface, and the evaluation of interaction efficiency of immobilized antibody with the corresponding antigen. High sensitivity of TIRE method and multilayer model, which was applied for the evaluation of experimental data, enabled to estimate the structure of such protein based layers. The obtained results allowed the evaluation of an average distance between the active sites of fragmented antibodies and gold surface. It was confirmed that fragmented antibodies are well orientated on the Au surface. Moreover, it was calculated that the analytical sensitivity for the Δ (λ) parameter of TIRE was 5.89 times better if compared to the sensitivity for the Ψ (λ) parameter, which is in fact similar to SPR measurement. Sensing layer based on well oriented frag-Ab shows a qualitatively better signal in comparison to intact-Ab, which are expected to be randomly oriented on the Au surface. Therefore, it could be concluded that frag-Ab modified Au surface seems to be very suitable for immunosensor design.

3.2 Study of antibody-antigen binding kinetics TIRE

Introduction. As it was noted in Chapter 1 the total internal reflection ellipsometry (TIRE) has been successfully applied for the evaluation of protein-protein interaction. TIRE combines the assets of both spectroscopic ellipsometry and surface plasmon resonance (SPR) techniques [78, 79, 94]. Therefore, it has a significant advantage due to simultaneous measurements of two ellipsometric parameters Δ and Ψ, which are related to the amplitude and phase shift of *p*- and *s*-components of polarized light respectively. This gives the possibility to analyze time-dependent changes of amplitude Ψ (t) and phase Δ (t) during the immobilization of biomolecules on the solid-liquid interfaces and/or interaction of immobilized biomolecules with ananalyte present in the solution. TIRE is the most suitable method to obtain a precise refractive index and thickness of the formed layers. For this reason TIRE appears to be a powerful tool for *in-situ* monitoring of protein adsorption process [92, 94, 95]. Very high sensitivity has been achieved using surface plasmon resonance (SPR) biosensor based on the Mach–Zehnder interferometer where phase quantities of *p*- and *s*- polarized waves were interrogated simultaneously. However, nonlinear behavior of phase curve requires calibration curve of the system with a well defined refractive index [96]. Some publications have been dedicated for studies of both phase and intensity information in order to extend the dynamic range of the analytical signal. The avidin-biotin model system has been applied in order to evaluate the efficiency of analytical signals based on simultaneous monitoring of phase and intensity and only intensity based SPR biosensors [65, 97,98]. The main advantage of TIRE is considered to be the higher sensitivity of this method in comparison with the SPR technique. This is achieved due to high susceptibility of Δ parameter to changes of the refractive index (n) and thickness (d) of the layer in the defined range of wavelengths around the surface plasmon resonance wavelengths ($\lambda_{R\Delta}$ or $\lambda_{R\Psi}$) corresponding to Δ and Ψ spectrums. It has been shown that Δ can be about 10 times more sensitive to n and d changes than Ψ, which is equivalent to the SPR response. Thus measurement of Δ is usually more preferable, especially when small changes of optical parameters are investigated. It has been also noted that the spectral shift of Δ is also slightly larger in comparison with that of Ψ [99]. This gives another possibility for kinetics study by measuring the spectral shift of Δ during different chemical and biochemical reactions and interactions taking place on the surface. The linear dependence between the shift in $\lambda_{R\Delta}$ and change of the refractive index or thickness of the film is the main advantage of this method. However, the highest sensitivity is achieved when kinetics study is performed by measuring Δ at a fixed wavelength [100] in the spectral range corresponding to the highest change of Δ vs λ dependence around $\lambda_{R\Delta}$. Nevertheless, this way is effective only if the shift in $\lambda_{R\Delta}$ induced by changes of $n \cdot d$ is smaller than the linear range of Δ vs λ, which is determined by surface plasmon conditions. In the case of larger shifts, which exceed surface plasmon conditions, the sensitivity of the method sharply decreases. As a result, the sensitivity of TIRE exploiting only Δ measurement is high at the beginning and low at the end of biomolecular layer formation process, because at the final phases of interaction a large number of biomolecules is adsorbed which significantly changes the thickness and refractive index and, therefore, the evaluation of Δ parameter could be complicated. Studies of biomolecular interaction kinetics are very important for the design of sensors with advanced selectivity [101]. Moreover, usually the detection of various biological substrates, such as different antigens, is realized in the presence of interfering species, therefore, high selectivity of the sensor is also required. In order to improve the selectivity, the advantage of ellipsometry, which offers measuring the changes of both ellipsometric parameters Ψ (t) and Δ (t) at the same time, should be exploited. Different sensitivities of Ψ (t) and Δ (t) in time at different phases of layer formation give a possibility to study the adsorption of proteins in more detail. Therefore, the investigation of residence time, if it is based on the evaluation of both ellipsometric parameters, enables to determine the selectivity of the studied sensing surface more exactly and gives additional information about the nonspecific interactions. It should be noted that inspite of smaller changes of parameter Ψ in comparison with that of Δ registered during n and d changes, the shift of resonance wavelength $\lambda_{R\Psi}$ corresponding to the highest changesof Δ and Ψ vs. λ is several times higher than the shift of $\lambda_{R\Delta}$ [96]. This means that the sensitivity of Ψ parameter remains the same within a larger $n \cdot d$ range while the sensitivity of Δ decreases significantly if this parameter is out of Δ vs. λ linear range, which is determined by surface plasmon conditions. Therefore, the sensitivity of Ψ parameter can be larger at the final phases of the binding of large biomolecules compared with Δ

parameter. For this reason simultaneous measurements of kinetics of both ellipsometric parameters enable to reach advanced sensitivity in a wide range of the binding process, even up to the complete formation of a biomolecular layer. Therefore, the assessment of both parameters enables to obtain more precise association and dissociation constants as well as residence time values.

In this section the investigation of immobilization kinetics of fragmented and intact antibodies against bovine leukaemia virus glycoprotein *gp*51 using TIRE method is presented. It demonstrates the advantage of simultaneous measurements of Ψ (t) and Δ (t) for the evaluation of parameters characterizing the kinetics of *gp*51 antigen interaction with immobilized antibodies.

3.2.1 Studies of antibody immobilization

The immobilization kinetics of intact and fragmented antibodies has been investigated. Fragmented antibodies were immobilized directly on the gold surface while intact antibodies were immobilized *via* 11-MUA based self-assembled monolayer formed on the gold surface in advance. Before the formation of antibody based layers the Δ and Ψ parameters vs. wavelength (λ) were measured for the two systems: (i) BK7 glass slide/Cr–Au layer and (ii) BK7 glass slide/Cr–Au layer/11-MUA monolayer. Figure 3.8 show typical results of these measurements obtained for system BK7 glass slide/Cr–Au layer.

After that the kinetics of antibody layer formation process was registered by TIRE. The measurements were performed at a fixed wavelength ($\lambda_{R\Psi}$), which corresponded to the minimal value of Ψ parameter established at surface plasmon resonance conditions. At the end of this process the measurement of Ψ as a function of wavelength $\Psi=f(\lambda)$ and Δ as a function $\Delta= f(\lambda)$ were performed (Figure 3.8).

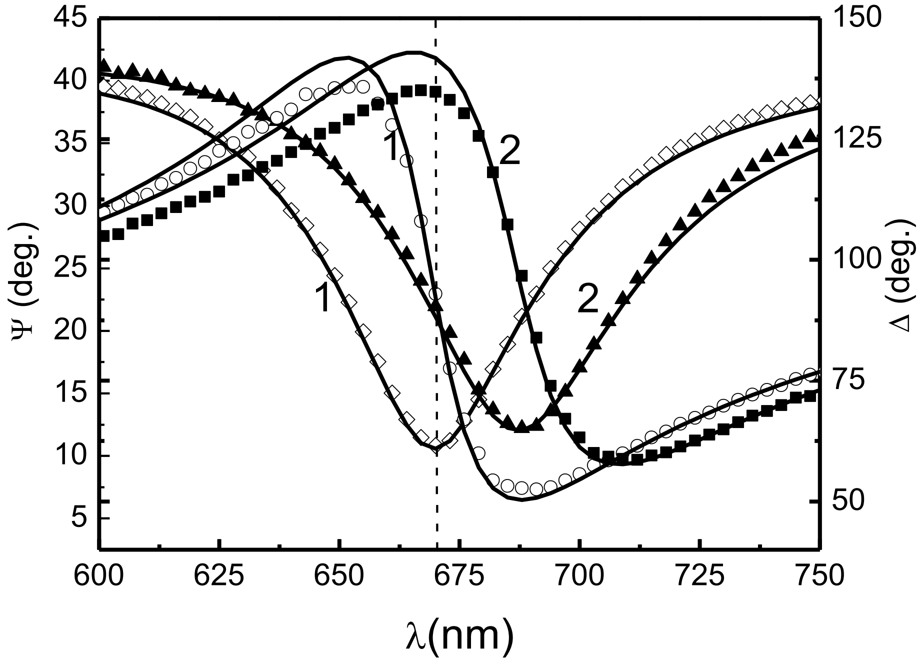

Fig. 3.8 *Spectra of ellipsometric parameters Ψ(λ) and Δ(λ) before and after the immobilization of fragmented antibodies onto gold surface; 1 – Au layer; 2 – Au layer after the modification by fragmented antibodies, points – experimental data, lines – fitting obtained by regression analysis.*

Assuming that the thickness of a biological monolayer is fixed at the value equal to the average antibody molecule diameter and that the shifts of resonance wavelengths $\lambda_{R\Psi}$ and $\lambda_{R\Delta}$ are directly proportional to the change of effective refractive index (n_e), the $\delta\Psi=f(\delta n_e)$ and $\delta\Delta=f(\delta n_e)$ dependences can be calculated using data from Figure 3.9. Here $\delta\Psi$ and $\delta\Delta$ are the changes of ellipsometric parameters at the beginning and the end of biomolecular monolayer formation process and δn_e is the difference between n_e and buffer solution refractive index (n_b). As it can be seen from Figure 3.9, the sensitivity ($S_{n\Delta}=\delta\Delta/\ \delta n_e$) of Δ parameter to the change of the refractive index was much larger at the beginning of monolayer formation (at small and medium δn_e values) in comparison with that at the end of this process (when δn_e value became much larger). However, the $\delta\Psi$ vs δn_e dependence was more abrupt at large δn_e showing that sensitivity ($S_{n\Psi}=\delta\Psi/\ \delta n_e$) of the Ψ parameter to n_e change increased at middle and final stages of the monolayer formation. In the case of fragmented antibody based layer formation, the ratio $S_{n\Delta}$ / $S_{n\Psi}$ varied from 25.5 to 0.726.

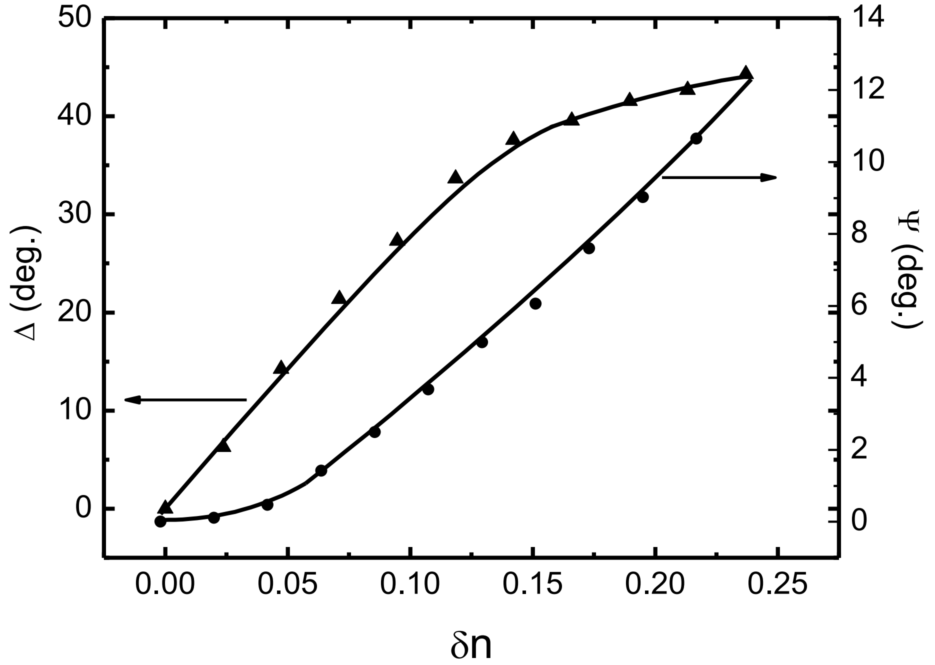

Fig. 3.9 *The calibration curves of ellipsometric parameters* Δ *and* Ψ *vs changes of effective index of refraction (*$\delta n = n_e - n_b$*).*

The sensitivity of Δ to the refractive index change is higher at initial phase of the monolayer formation (small and medium δn values) while the Ψ vs. δn dependence is more abrupt at large δn showing that sensitivity of this parameter increases at the final stage of monolayer formation. The total change of n_e was 0.2375 demonstrating that Δ parameter was more sensitive to n_e change at the beginning of antibody layer formation while Ψ was more sensitive at the end of this process.

The results of *in-situ* evolution of ellipsometric parameters as functions of Δ (t) and Ψ (t) were obtained during the formation of fragmented (Au_1) and intact (Au_2) antibody based layers (Figure 3.10). As it can be seen from Figure 3.10 in both cases the total change of the value of ellipsometric parameters was higher for the Δ parameter in comparison with the Ψ parameter. However, the change of Δ parameter in time saturated and became constant in a shorter time frame than that observed for the saturation of Ψ parameter. For the fragmented antibody based layer the Δ parameter saturated within ~175 s, meanwhile the change of Ψ parameter remained significant even up to 1500 s. For the intact antibody based layer these values were 250 s and 3000 s correspondingly.

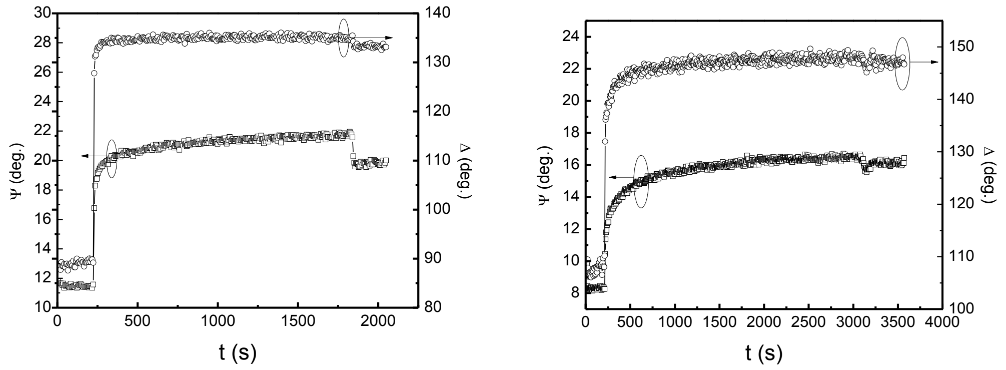

Fig. 3.10 *Monitoring ellipsometric parameters a functions* $\Psi(t)$ *and* $\Delta(t)$ *at* $\lambda=670$ *nm wavelength and 70° angle of light incidence during fragmented antibody binding to the gold surface (left) and intact antibodies binding to the 11-MUA self-assembled-monolayer (right).*

The small decrease of Ψ and Δ at the end of kinetics demonstrates how these parameters changed after the elimination of not bound antibodies by washing the surface of biological layer with 0.01M PBS, pH7.4. The relative decrease of Ψ in comparison with the maximal value of Ψ change obtained during antibody layer formation was 22.7% and 18.75% for fragmented and intact antibody based layers respectively. For Δ parameter this decrease was only 4% and 2%, respectively.

In order to investigate the effectiveness of the fragmented and intact antibody based layers in the binding of BLV glycoprotein *gp*51, TIRE study was performed *in-situ* for both Au_1 and Au_2 samples by injecting into the cell the same (0.5 mg/ml) antigen concentration. In the case of antibody based layer formation, the $\Psi=f(\lambda)$ and $\Delta=f(\lambda)$ curves were determined within the complete antigen layer formation process including the initial and the final phases. Using the functions of ellipsometric parameters Ψ (t) and Δ (t) the change of the effective refractive index n_e in time was determined by applying effective medium approach. According to the averaged results from both Ψ (t) and Δ (t) measurements, the different sensitivities of both ellipsometric parameter in time was obtained (Figure 3.11).

Assuming that n_e is directly proportional to the surface concentration of BLV glycoprotein *gp*51 adsorbed on the antibody-based layers the relative

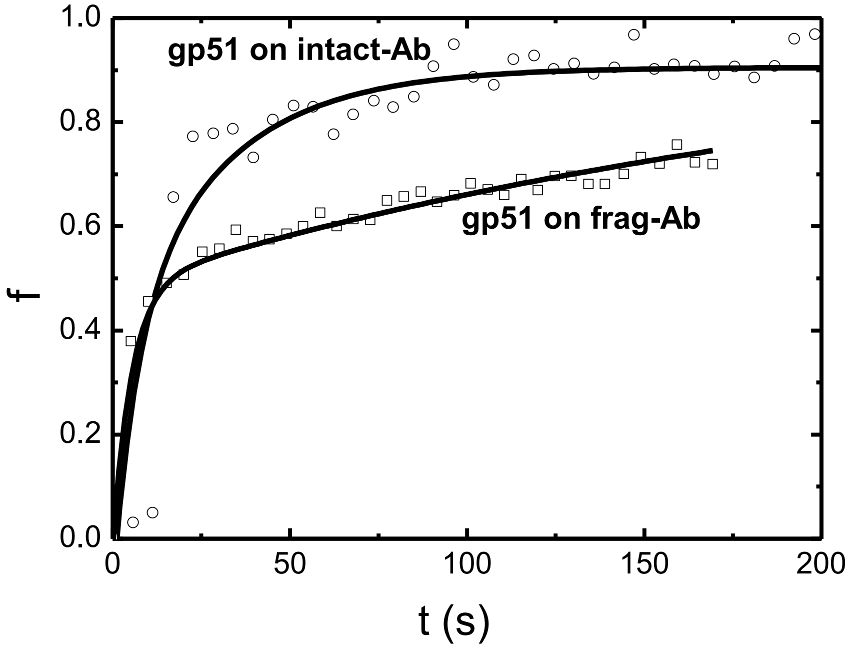

Fig. 3.11 *Evolution of ellipsometric parameters Ψ (t) and Δ (t) in time for antigen interaction with frag-Ab and intact-Ab (at λ=670 nm wavelength and 70^0 angle of light incidence).*

saturation (fill factor) of the formed layer, which was determined by the ratio of N/N_t (where N is the number molecules trapped on a surface square unit containing totally N_t traps, while the number of traps is proportional to the surface concentration of immobilized antibodies) was obtained. The fill factor is a time function for both sensing layers based on fragmented and intact antibodies (Figure 3.11). At the final stage of antigen monolayer formation process the changes of the refractive index became small and then the sensitivity of the measurements strongly depended on the signal to noise ratio. For this reason additional assessments of ellipsometric parameters as functions of time Ψ (t) and Δ (t) during the antibody-antigen dissociation process and during rinsing with 0.01M PBS, pH7.4 were performed. The results of Ψ and Δ parameter changes in time are presented in Figure 3.12 (A, B).

The Figure 3.12 (A, B) shows that the absolute change in degrees after rinsing was higher in the case of Δ in comparison with Ψ, however, the signal to noise ratio ($R_{s/n}$) was 3.14 and 1.50 for Ψ and Δ respectively. Thus at the final stage of interaction the change of Ψ was 2 time more sensitive than the change of Δ as can be easily calculated from $R_{s/n}$ values. It should be noted that such behaviour of ellipsometric parameters was caused by a rotating polarizer ellipsometer (RPE) measurements features. In the RPE measurement errors strongly increase in specific measurement regions, such as $\Delta \cong 0°$ and and $\Delta \cong 180°$ $2\Psi \cong 90°$. RPE measures cos Δ instead of Δ. In this case, the value of Δ is obtained from the conversion of cos Δ to Δ. However, cos Δ is not a linear function of Δ and measurement error varies according to the absolute value of cos Δ [7]. As shown in Figure 3.12 (A) and (B), Ψ and Δ values in the final stage of layer formation were about 15.51° and 123.51° respectively. As we can see from Figure 3.10 and Figure 3.12 (A and B), at the initial stage of *in-situ* dynamic measurements our device works in the most sensitive region for delta ($\Delta \cong 90°$), meanwhile at the final stage Ψ parameter is in the linear region and with lower signal to noise ratio than Δ in the high error region near $\Delta \cong 180°$. From the measurements of features presented above it is reasonable to assume that the noise in our experiment at the initial stage of interaction mainly depended on the investigated system, while at the final stage of the measurement a significant fraction of noise is generated due to specific features of a rotating polarizer ellipsometer.

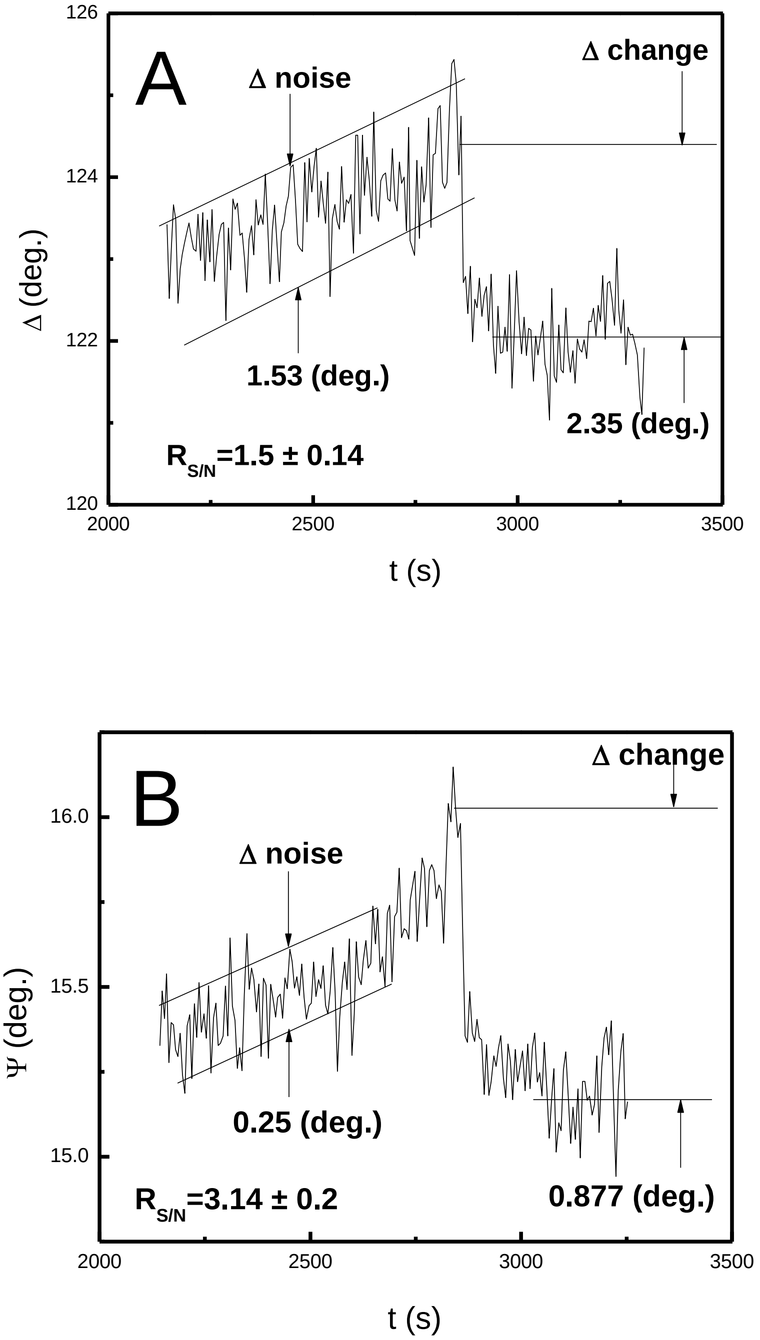

Fig. 3.12 *(A, B). Dissociation kinetics as a function of ellipsometric parameter Ψ(t) of BLV glycoprotein gp51 after the interaction with fragmented antibody based sensing layer (A). Dissociation kinetics as a function of ellipsometric parameter Δ(t) of BLV glycoprotein gp51 after interaction with the fragmented antibody based sensing layer (B).*

Therefore, in order to minimize the errors of measurements the type of ellipsometer should be taken into account and ellipsometric measurements should be performed in such a way that the highest sensitivity of ellipsometric parameters would be adjusted for the most important stages of experiment, especially when *in-situ* measurements are performed.

3.2.2 Protein adsorption kinetic analysis and modelling

In order to analyse the kinetic processes of protein adsorption, the simplest Langmuir equation with one exponential function, which considers just direct and simultaneous interaction of analyte with the sensing layer, is mostly applied [101, 102, 103, 104]. Moreover, in most TIRE application cases only one ellipsometric parameter Δ (t) or Ψ (t) is evaluated [104,105]. In order to gain some additional accuracy, differently from many other authors, in present research the assessment of both ellipsometric parameters Δ (t) or Ψ (t), which characterize the formation of the layer based on biomolecules was performed. The model used for this analysis was constituted by assuming following approaches: (i) monolayer was characterized by the constant thickness (d) and effective refractive index (n_e), which varied during the monolayer formation; (ii) the number of molecules (N) trapped on a surface square unit containing N_t traps (the number of the traps is proportional to the surface concentration of immobilized antibodies) was considered to be proportional to the n_e and could be calculated using the effective medium approach for 2D objects:

$$\frac{N}{N_t} = \frac{n_e^2 - n_b^2}{n_l^2 - n_b^2}; \quad (3.1)$$

The indexes *e*, *b* and *l* correspond to the effective refractive index of the layer, buffer solution and completed monolayer, respectively. As it was mentioned in Section 3.2.2, the value of n_e can be obtained by the calibration of Δ or Ψ

values using Δ (λ) or Ψ (λ) dependences for systems without and with a completely formed monolayer respectively, as it was demonstrated in Figure 3.9 The calibration procedure was performed assuming that the shift of parameters Δ or Ψ vs. wavelength (λ) during the formation of the monolayer was directly proportional to the change in the effective refractive index. Moreover, for the calculation of N/N_t vs. time an average d value of $n_e(t)$ was obtained using both kinetic curves of Δ (t) or Ψ (t). Additionally, Figure 3.12 (A) and (B) shows that after the rinsing of the completely formed antibody-antigen layer with 0.01M PBS, pH7.4 corresponding variations of ellipsometric parameters were relatively small. This fact demonstrates that the formation of monolayer was mainly caused by their reversible interaction of molecules in 0.01 M PBS, pH 7.4. In the case when only a fraction of the adsorbed molecules desorbs, a generalized Langmuir equation, which takes into account the residence time effect [7], should be used for calculation.

$$\frac{dN_1}{dt} = k_a \cdot c \cdot (N_t - N_1 - N_2) - (k_d + k_r) \cdot N_1; \quad (3.2.)$$

$$\frac{dN_2}{dt} = k_r \cdot N_1; \qquad (3.3)$$

Here k_a is the association coefficient, c is the concentration of antibody solution over the bondable surface, k_d is the dissociation coefficient, k_r is the rate of molecules, which bound irreversibly to the binding sites, N_1 and N_2 are the surface concentrations of molecules which are reversibly or irreversibly bonded to the binding sites. Eqs. (3.2) and (3.3), taking into consideration Eq. (3.1), yield to the following solution:

$$\frac{N}{N_t} = \frac{k_1}{r_1 - r_2}\left[\left(\frac{k_3}{r_1} + 1\right) \cdot \exp(r_1 \cdot t) - \left(\frac{k_3}{r_2} + 1\right) \cdot \exp(r_2 \cdot t)\right] + \frac{k_1}{k_2}; \quad (3.4)$$

Here $k_1 = k_a$c; $k_2 = k_d + k_r$ and $k_3 = k_r$;

$$r_1 = -\frac{k_1 + k_2}{2} + \sqrt{\frac{(k_1 + k_2)^2}{4} - k_1 \cdot k_3}\ ; \quad r_2 = -\frac{k_1 + k_2}{2} - \sqrt{\frac{(k_1 + k_2)^2}{4} - k_1 \cdot k_3}\ ; \qquad (3.5)$$

It should be noted that according to Eq. (3.4), the ratio $k_1/k_2 \approx 1$. This is due to the fact that the number of molecules (N), which are bound to a square unit of the surface, has to be not higher than the number of traps (N_t). The N_t is proportional to the surface concentration of places suitable for interaction with proteins or formation proteins complex, e.g., it should be proportional to the surface concentration of the immobilized antibodies. It gives the following requirement for the kinetic coefficients $k_1 \leq k_2 > k_3$, which should be taken into the account during fitting of experimental data. Using Eq. (3.4) kinetic coefficients were determined for the intact and fragmented antibodies and antigen monolayer formation process. The results are summarized in Table 3.1. The data presented in Table 3.1 show that the association rate of fragmented antibody adsorption on Au was slightly higher (≈4 times) than the rate of intact antibody interaction with 11-MUA monolayer formed onto the Au layer. However, the residence time of the monolayer formation process was much shorter (≈25 times) in the case of fragmented antibodies in comparison to the intact ones. This shows that the formation of the monolayer, which was based on fragmented antibodies adsorbed on Au, was significantly faster than the formation of the intact antibody layer on the 11-MUA based monolayer. Differences in residence time discussed above were most probably related to the different nature of interactions and formation of complexes characterized by different dissociation constants. On the contrary, the association rate of antigen was the same for the fragmented and intact antibody based layers, but the residence time was significantly longer (≈ 8 times) for interaction between antigen and the fragmented antibody based layer in comparison with the case where antigen was interacting with the intact antibody based monolayer. Obtained results demonstrate that the preparation of the immunosensor developed using the fragmented antibody based sensing layer is faster than using the intact antibody based layer. The preparation of the sensor based on intact antibody based layer takes minimum 1.5 min. Moreover, the results presented in Table 3.1 illustrate that the residence time of antigen interaction with the fragmented antibody based monolayer was significantly longer than calculated from the antigen interaction with the intact antibody based layer.

Table 3.1 *Kinetic constants determined by partial reversibility model for the immobilization of antibodies (fragmented and intact) and for the evaluation of antigen binding on appropriate layers: (i) fragmented antibodies (Frag-Ab) were immobilized on bare gold surface, (ii) intact antibodies (Intact-Ab) were immobilized on SAM formed over gold surface, (iii) BLV glicoprotein gp51 binding to immobilized fragmented antibody by formation of corresponding complex (gp51/frag-Ab), (iv) BLV glycoprotein gp51 binding to immobilized intact antibody by formation of corresponding complex (gp51/intact-Ab).*

Sample	$k_1(s^{-1})$	$k_2(s^{-1})$	$k_3(s^{-1})$	$k_a(s^{-1}mol^{-1}L)$	$\tau_r(s)$
Frag-Ab	0.3252	0.3943	0.2869	$5.42 \ast 10^4$	3.5
Intact-Ab	0.1164	0.1165	0.0113	$3.88 \ast 10^4$	88.4
*gp*51/frag-Ab	0.085	0.086	0.0075	$8.67 \ast 10^3$	133
*gp*51/intact-Ab	0.088	0.097	0.0586	$8.96 \ast 10^3$	17,1

This difference is an evidence of the fact that to establish strong interactions in the antigen/antibody complex between the antigen and the fragmented antibody based monolayer longer time is required in comparison with the formation of antigen complex with intact antibodies. This fact could be explained by the ability of some intact antibodies to interact with antigen *via* two binding sites (it should be noted that only well-oriented intact antibodies, which expose both binding-sites towards the solution, are subjected to this kind of interaction) instead of one binding site available in the fragmented antibodies. This single interaction place might be the reason of significantly weaker antigen binding, subsequently making the probability of dissociation of weakly bonded antigen-antibody complex much higher. Therefore, more such complexes dissociate before the formation of advanced interactions in antigen-antibody complexes. This fact is well demonstrated by the increased residence time, which indicates that in the case of fragmented antibodies, a longer time is needed for the establishment of advanced interactions in the antigen-antibody complex. Weaker interactions are requested in the design of reusable immunosensors. Therefore, due to slower and weaker antigen interaction with the fragmented antibody based layer, this kind of layer is more preferable for reusable immunosensors. Meanwhile, the intact antibody layer based system offers the faster analytical signal and formation of stronger antibody-antigen complex [75, 106].

Conclusions: section 3.2

In-situ total internal reflection ellipsometry has been applied for the study of immobilization of fragmented and intact antibodies and for the evaluation of immobilized antibodies interaction with antigen BLV glycoprotein *gp*51. The optical response of ellipsometric parameters in TIRE method has shown that the sensitivities of Ψ (t) and Δ (t) were different at different stages of biomolecular layer formation. At experimental conditions Δ (t) showed a larger sensitivity at the initial phase of the process, while at conditions that are near to the steady-state equilibrium it decreased significantly. On the contrary, Ψ (t) was less sensitive at the initial phase and it significantly increased after the establishment of conditions that are near to the steady-state equilibrium. Therefore, this fact should be taken into account during the evaluation of biomolecular layer formation kinetics. Analysis based on partial reversibility model has shown that the residence time effect had a significant role in both cases: (i) the determination of affinity constants of fragmented and intact antibodies, (ii) the characterization of immobilized antibody interaction with antigen, which was present in the sample. In the case of fragmented antibody interaction with the gold layer, the residence time was relatively short if compared with that calculated for the interaction of intact antibodies with the 11-MUA based self-assembled monolayer. However, the residence time of antigen interaction with the fragmented antibody based monolayer was longer than that calculated for antigen interaction with the intact antibody based layer. It means that in order to establish strong interactions in the antigen/antibody complex more time is required. Therefore, due to slower association of the fragmented antibody based layer with antigen, this kind of layer is more preferable for multifold use immunosensors and even for implantable sensors, while the intact antibody based layer, due to a much faster association with antigen, is more suitable for the development of immunosensors with advanced selectivity and sensitivity.

3.3 *In-situ* study granulocyte colony stimulating factor (GCSF) interaction with its receptor

Introduction. Spectroscopic ellipsometry in dynamic mode is able to perform *in-situ* measurements in a wide spectral range with a sub-second data acquisition rate. Such advantages of fast spectral measurements make it possible to study the dynamics of interactions between biomolecules with better accuracy than single wavelength dynamic ellipsometry. Higher accuracy is obtained with the ability to determine the dispersion of the refractive index from spectroscopic ellipsometry. In order to show the advantages of spectroscopic dynamic *vs.* single wavelength ellipsometry, experiments were performed in spectroscopic dynamic TIRE mode meaning that data during all *in-situ* measurements were recorded in the spectral range from 300 nm to 1000 nm simultaneously.

In this part of the doctoral dissertation the dynamic TIRE has been applied in order to develop an ellipsometric methodology to evaluate the association and dissociation parameters of the kinetic interactions between various biomolecules through the determination of the refractive index dispersion and layer thickness from spectroscopic dynamic ellipsometry data.

Secondly, the advantages of spectroscopic ellipsometry dynamic measurements have been demonstrated by the characterization of the *in-situ* interactions of monomeric (mGCSF) and dimeric (dGCSF) granulocyte colony stimulating factor with its receptor (GCSF-R), which was immobilized on a thin gold layer.

3.3.1 Characterization of GCSF receptor layer formation

Two samples of thin gold films (A) and (B) with very similar values of layer thickness and surface roughness were used for further immobilization of protein biomolecules. Both gold layers under investigation were polycrystalline. The thickness and surface roughness of the gold layers were measured by using scanning probe microscope D3100, Nanoscope IVa (Veeco). The layer thickness and root mean square (RMS) values of surface roughness for both samples was $d = 47.6 \pm 0.3$ nm, RMS = 0.7 ± 0.3 nm and $d = 48.7 \pm 0.3$ nm, RMS = 0.9 ± 0.3 nm, respectively. The optical constants of gold films for both samples were determined from the analysis of TIRE data and layers thicknesses were fixed parameters during fitting procedure. The B-Spline function was used to evaluate the optical constants of gold. The obtained dispersion curves agreewellwith data in [16, 80]. The contribution of surface roughness (RMS ≈ 0.7–0.9 nm) was taken into account in the calculations of ellipsometric parameters $\Psi(\lambda)$ and $\Delta(\lambda)$ in order to develop an adequate model [80].

The TIRE measurements were performed in the spectral range of 300 nm to 1000 nm have shown that the surface plasmon waves were excited at an external angle of incidence equal to 70° for samples A (Bk7 glass prism/Cr–Au/11MUA) and B (Bk7 glass prism/Cr–Au/11MUA/(EDC/NHS) + ProteinG) respectively. In the SPR spectra, the dip for $\Psi(\lambda)$ and strong changes for $\Delta(\lambda)$ were observed correspondingly at 660 nm and 658 nm (Figure 3.13).

.

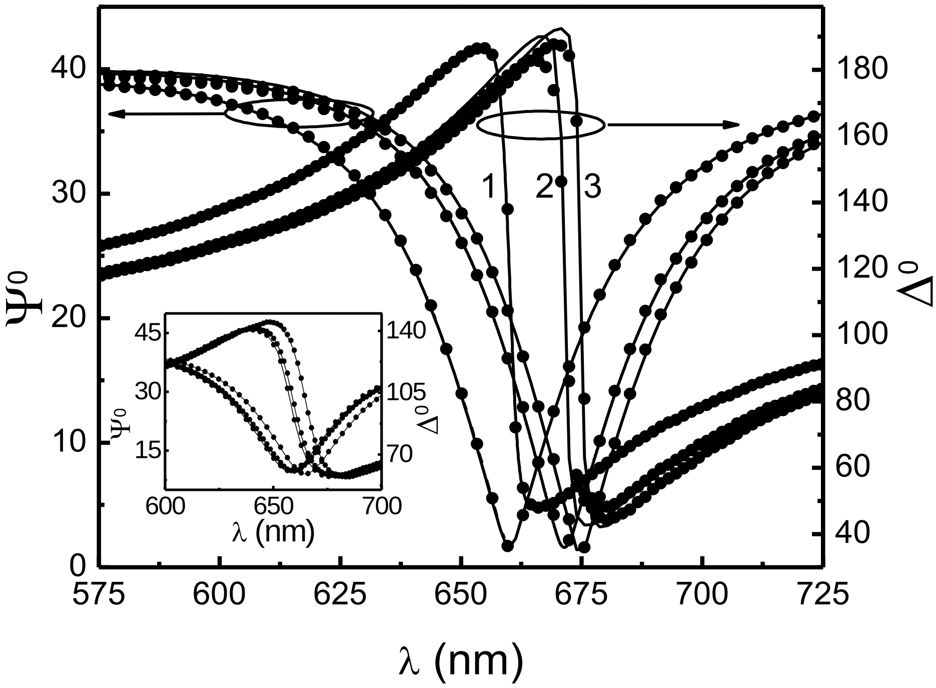

Fig. 3.13 *Experimental (points) and calculated (curves) spectra of ellipsometric parameters for sample B (oriented GCSF-R). Curve 1 represents Ψ(λ) and Δ(λ) Bk7 glass prism/Cr–Au/ 11MUA/PBS, curve 2 – after formation of EDC/NHS + ProteinG layer, curve 3 represents oriented GCSF-R monolayer formation. The inset shows similar formation steps for sample a non-oriented GCSF-R layer formation.*

During the TIRE measurements all steps of binding receptor (GCSF-R), mGCSF and dGCSF binding were recorded by injection solutions into the cell with a syringe pump. The experimental ellipsometric data was analyzed by J.A. Woollam Co., Inc., data acquisition program “Complete Ease”.

The TIRE data of non-oriented and oriented GCSF-R receptor (structure is shown in Ch.1 Figure 1.7). The immobilized structure was analysed by multi-layer model [80]. The formations of GCSF-R layers were performed using 5 μg/ml receptor and 500 μg/ml of HSA solution. Therefore, the dispersion of the refractive index and layer thickness of 6 nm was obtained using a pure HSA layer from 500 μg/ml of HSA solution. The Cauchy dispersion function $n = A + B/\lambda^2 + C/\lambda^4$ [7] was used to describe the refractive index of HSA layer. The values of the Cauchy function coefficients A=1.386±0.01, B=0.012±1.1×10^{-3} μm^2, C=0 (Figure 3.14 Curve 1) and layer thickness d=6 nm were determined from regression analysis of the data of a pure HSA layer using the multilayer model.

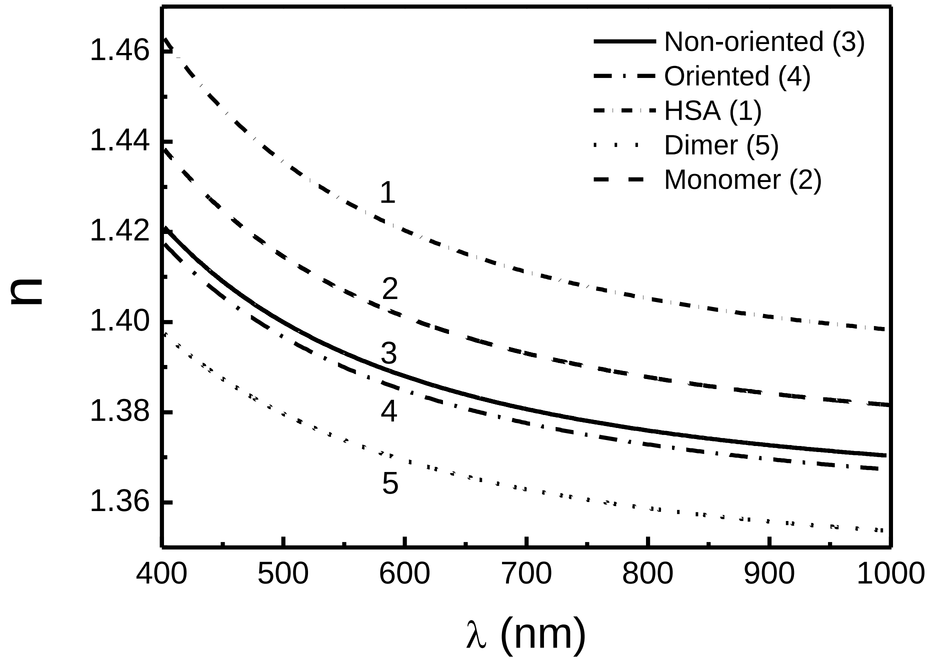

Fig. 3.14 *Spectra of refractive index of studied biomolecular layers obtained by Cauchy function and Bruggeman effective media approximation for HSA and other formed layers, respectively.*

It should be noted that the model gives an effective refractive index value with close-packing of molecules. The obtained value of thickness (d=6 nm) is lower than the average value of HSA dimensions and is closer to the smallest dimension of 3.9 nm. The value of the fitted parameter d indicates that the dominating orientation of HSA molecules is that of maximum surface contact.

The oriented and non-oriented GCSF-R monolayers were supposed to be composed of receptor, HSA and buffer solution. In both cases we assume the formation of monolayers only, due to the specific interactions determined between the surface and protein [107]. The composition of GCSF-R layers was estimated in the Bruggeman effective media approximation (EMA) with the parameters obtained for pure HSA layer. From the fitting procedure it followed that the oriented GCSF-R layer was composed of 0.6GCSF-R+0.4PBS and 0.65GCSF-R+0.35PBS for non-oriented GCSF-R layer. The larger values of refractive index in the case of the non-oriented GCSF-R layer indicates increased overall binding [96] and, as a result, that more HSA molecules are attached to the surface compared to the oriented GCSF-R layer (Figure 3.14 Curves 3, 4). In the case of non-oriented GCSF-R, the layer was assumed to be composed of close packed receptors and HSA molecules, meanwhile for oriented immobilization, the layer was more sparse, because it is mainly composed of receptor which extends more into buffer solution. The relatively smaller value of refractive index in this case shows minuscule contributions of HSA molecule in oriented GCSF-R layer. Meanwhile, the contribution of HSA molecules to the refractive index of the non-oriented GCSF-R layer was vast, because the layer possessed very little GCSF binding capacity due to the fact that HSA directly competed with GCSF-R for surface binding sites.

In the case of both (oriented and non-oriented) GCSF-R monolayers, the thickness of the pure HSA layer was used (d=6 nm) as a fixed parameter of layer thickness in regression analysis, meanwhile all changes in the optical response of ellipsometric parameters were modelled as changes of refractive index values in time. Thus, similar conditions were accepted for the calculation of dynamics of ellipsometric parameters Ψ (λ, t) and Δ (λ, t) for both oriented and non-oriented GCSF-R receptors monolayers formation. The relative changes of effective refractive index allow the calculation of the formation (fill factor) of GCSF-R monolayer on the surface from which the kinetic were derived.

The analysis of dynamic TIRE data of samples with non-oriented and oriented GCSF-R layers has been performed by a reverse dynamic fitting procedure starting from the values obtained for completely formed GCSF-R layers. As noted above, the Bruggeman EMA has been used for kinetic data analysis as well as for completely formed monolayers of receptor. For *in-situ* data, the value of the effective refractive index was in between that of maximally adsorbed GCSF-R and buffer solution. Thus the change of effective refractive index over time was transformed to the change of fill factor of GCSF-R layers. It was assumed that the intrinsic refractive indices of HSA, GCSF-R, mGCSF and dGCSF are the same, as they all are proteins with similar composition. Thus, it enables to analyze the effective refractive index changes of layers composed of different proteins. In order to evaluate the association and dissociation constants for oriented and non-oriented GCSF-R receptor interaction, the generalized Langmuir equation, which takes into account the residence time effect, [18,108] was applied (see formula 3.2 and 3.3 from section 3.2.3). Using the models that fit best with experimental data, we obtained the following characteristic association, dissociation and residence times 20.4 s, 22.9 s, 126.1 s for non-oriented and 24.2 s, 26.8 s and 246.9 s for oriented GCSF-R. It is clearly seen that association and dissociation times are similar for oriented and non-oriented immobilization of GCSF-R receptors meanwhile the residence time is 2 times longer for oriented GCSF-R receptor. The application of Langmuir equation which accounts for the residence allowed to reveal the time differences of oriented and non-oriented GCSF-R monolayer formation. The comparison of affinity constants of oriented and non-oriented GCSF-R indicated that the oriented association of GCSF-R is two orders of magnitude higher (Table 3.2).

Table 3.2 *Affinity constants of oriented and non-oriented GCSF-R, mGCSF, dGCSF.*

GCSF	k_a (s^{-1} M^{-1})	k_d (s^{-1})	K_a (M^{-1})	K_d (M)	k_r (s^{-1})
Sample A (non-oriented receptor)	6.6×10^3	4.4×10^{-2}	1.5×10^5	6.58×10^{-6}	7.93×10^{-3}
Sample B (oriented receptor)	1.1×10^6	3.7×10^{-2}	2.9×10^7	3.47×10^{-8}	4.05×10^{-3}
mGCSF	5.6×10^5	1×10^{-1}	5.6×10^6	1.78×10^{-7}	
dGCSF	9.8×10^5	5.2×10^{-2}	1.9×10^7	5.25×10^{-8}	1.84×10^{-1}

This implies that the layer of protein G facilitates increased binding of the GCSF-R compared to the layer of EDC/NHS, due to the nature of the interaction [96] specificity. Therefore in further studies of the binding kinetics of monomeric and dimeric GCSF protein only the oriented GCSF-R sensor was used.

3.3.2 GCSF monomer and dimer dynamic adsorption study

In order to demonstrate the capability of the spectroscopic dynamic TIRE method, the kinetic interactions between the mGCSF, dGCSF molecules and the immobilized oriented GCSF-R monolayer were studied. Dynamics of effective refractive index of mGCSF and dGCSF monolayer formation on GCSF-R oriented monolayer is shown in Figure 3.15.

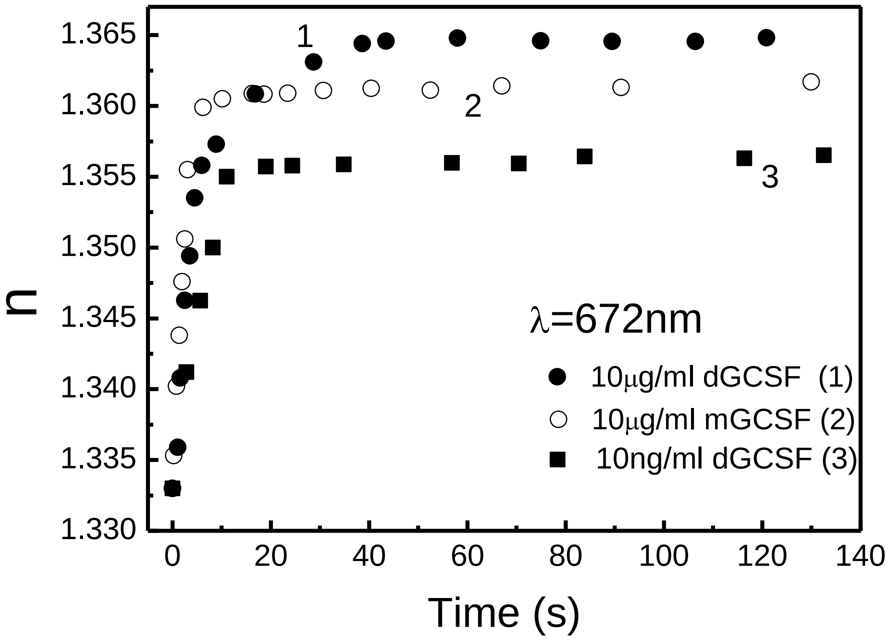

Fig. 3.15 *Dynamics of refractive index (n) of mGCSF and dGCSF monolayer formation on GCSF-R oriented monolayer, curve 1 – 10 μg/ml of dGCSF, curve 2 - 10 μg/ml of mGCSF, curve 3 – 10 ng/ml of dGCSF.*

Curves 1 and 2 indicate dGCSF and mGCSF kinetics at 10 μg/ml concentrations in PBS respectively. Curve 3 shows the dGCSF effective refractive index dynamics when concentration was 10 ng/ml in PBS. In Figure 3.15 (Curves 1 and 3) it is clear that the change of refractive index for 10 μg/ml and 10 ng/ml concentrations of dGCSF differs only about 25 %. The obtained effective refractive index values of dGCSF at 10 ng/ml and 10 μg/ml solutions Figure 3.15 (Curve 3 and 1) confirmed the assumption that a 10 μg/ml concentration is enough to form a monolayer with closest-packing of dimeric protein. Thus, for both mGCSF and dGCSF, association kinetics were performed at 10 μg/ml concentration and analysed in the frame of a first pseudo order kinetic equation [109].

The obtained small differences in the values of effective refractive index (Figure 3.15 Curves 1 and 2) for dGCSF and mGCSF monolayers confirm the assumption that binding processes of dimeric and monomeric GCSF have different mechanisms.

In the case of mGCSF binding kinetics, a standard Langmuir equation which takes into account only association and dissociation processes should be applied [109]. The obtained affinity constants for mGCSF when association and dissociation times were 3.3 s and 10 s are presented in Table 3.2 For dGCSF association, the kinetics is described with a two-step association process. The first step is the reversible association of one end of the dimer to the receptor active site. The rate of association (k_a) during this step can be represented by the characteristic time (τ_a) and (τ_d) for the rate of dissociation (k_d). The second step is the non-reversible binding of the second side of the dimer to another receptor active site, which we call residence. The residence rate (k_r) can be transformed into residence time (τ_r). This second step really corresponds to the residence time effect and could be described by the same kinetic equations as presented in [18]. The solution are formulas (3.4) and (3.5) from section 3.2.3. The first step association time τ_a= 4.3 s, dissociation time τ_d= 19.4 s and second step of association residence time τ_r= 5.4 s.

It is reasonable to assume that first step of dGCSF association is very similar to mGCSF association; meanwhile, the second association step is a characteristic kinetic feature of dGCSF. The total binding time of dGCSF molecules is about three times longer than in the case of mGCSF and the dissociation time is twice longer for dGCSF.

Due to the application of different kinetic models for mGCSF and dGCSF binding, the affinity constants K_a describe slightly different processes. For the association kinetics of mGCSF, a standard Langmuir equation with one-step association and dissociation process has been applied [109] and the affinity constant (K_a = 5.6×10^6 M^{-1}) describes the direct attachment of monomer molecule to the sensing surface. Meanwhile, for dGCSF we have interpreted the molecule's association kinetics in the frame of a two-step association process. Therefore, the affinity constant (K_a = 1.9×10^7 M^{-1}) of dGCSF describes the rate of the first step of binding only when one side of dimer is attached to the active side of receptor, so it is only a partial description of kinetics. The residence constant describes the kinetics of the binding of the second side of the dimer which is the rate limiting step of the interaction.

Conclusions: section 3.3

The spectroscopic dynamic TIRE method has been used for characterization of *in-situ* interactions of monomeric and dimeric granulocyte colony stimulating factor with its receptor immobilized on thin gold layer. TIRE in spectroscopic dynamic acquisition mode is able to reveal minuscule differences in association and dissociation times through the more precise determination of the refractive index dispersion and elimination of signal non-linearity using regression analysis of spectroscopic ellipsometry data. These differences in the dynamics of the refractive indices of mGCSF and dGCSF allow us to recognize that diverse kinetic models need to be applied to differentiate the kinetic characteristics of similar molecules.

3.4 Structural and optical properties of Al_2O_3/ZnO nanolaminates synthesized by atomic layer deposition (ALD) method

Introduction. In order to tune the optical properties of the ZnO/Al_2O_3 nanolaminates it is necessary to know how these properties depend on preparation conditions for separate components. The investigation of optical properties of Al-doped ZnO showed the increase of band gap as a function of Al doping concentration varying from 3.28 to 3.7. [109,110]. This blue shift of band gap has been attributed to the Al doping of ZnO layers (Burstein−Moss effect) as well as to the quantum confinement effects. [110, 111]. It was demonstrated [111] that Al_2O_3 buffer layer led to an increase of the near band edge emission (NBE) and decrease of a deep level emission (DLE). The ratio of NBE/DLE intensities was above. The DLE quenching of the ZnO films deposited on Al_2O_3 buffer layer was attributed to the decrease of oxygen vacancies concentration on the interfacial layer. The proposed model supposed that the oxygen atoms are removed from the amorphous Al_2O_3 layer and occupy the oxygen vacancies at the initial stage of the growth of ZnO films. This lead to the improvement of film crystallization [112]. Recently, the enhancement of the third-order optical nonlinearity in ZnO/Al_2O_3 nanolaminates fabricated by ALD was demonstrated [112].

In the present section the structural and optical properties of ZnO/Al_2O_3 nanolaminates, fabricated by ALD method is reported. Single layer parameters (thickness, grain size, refractive index, extinction coefficient, and band gap) were calculated. The mechanism of nanolaminates formation and penetration of Al into ZnO layer is proposed.

3.4.1 Optical properties of Al_2O_3, ZnO and Al_2O_3/ZnO films

Transmittance. The transmittance spectra of Al_2O_3/ZnO nanolaminates are shown in Figure 3.16 a. All measured samples were transparent in 550-1100 nm range of wavelenghts. The absorption edge of the samples was found in the region from 370 to 410 nm. Blue shift of absorption edge was observed particularly with the decrease of nanolaminate bilayer thickness. The band gap value of the samples was calculated considering that Al_2O_3 was totally transparent and the observed absorption edge was related to ZnO layers. ZnO is known as a semiconductor with direct optical transitions. Therefore, the absorption coefficient (α) can be described by the following equation: [113].

$$\alpha = \frac{(h\nu - E_g)^2}{h\nu} \quad ; \qquad (3.6)$$

Here $h\nu$ and E_g are a photon energy and a band gap values, respectively. Absorption coefficient α is related to the transmittance of the sample T as:

$$\alpha \cdot d = \ln\left(\frac{1}{T}\right); \qquad (3.7)$$

where *d* is a thickness of the sample.

In order to simplify the calculation of the band gap values of the nanolaminates the optical density *OD* ($OD = \alpha \times d$) was used. Considering equation 3.6 and equation 3.7, the plot $(OD \times h\nu)^2$ *vs. hν* was obtained (Figure 3.16). Band gap values E_g were graphically calculated in linear part of the absorption edge with respect to equation 3.6 (Figure 3.16 b). The results are summarized in table 3.3.

Table 3.3 *Band gap of Al_2O_3/ZnO nanolaminates with different bilayer thicknesses and ZnO single thin film of 50 nm thickness.*

Nanolaminate	***E*g (eV) from transmittance**	***E*g (eV) from ellipsometry**
Al_2O_3/ZnO 50 (2/2 nm)	3.41	3.45
Al_2O_3/ZnO 10 (10/10 nm)	3.3	3.36
Al_2O_3/ZnO 2 (50/50 nm)	3.28	3.31
ZnO (50 nm)	3.24	3.25

As it can be seen, the band gap increases with the decrease of the bilayer thickness in the nanolaminates. The obtained E_g values can be affected by structural defects (interstitials, vacancies, etc.) and impurities. The observed blue shift could be determined by three physical phenomena: [114,115] (i) quantum confinement effect of small nanograins, (ii) doping of ZnO by Al and (iii) the improvement of crystalline quality of the single layer.

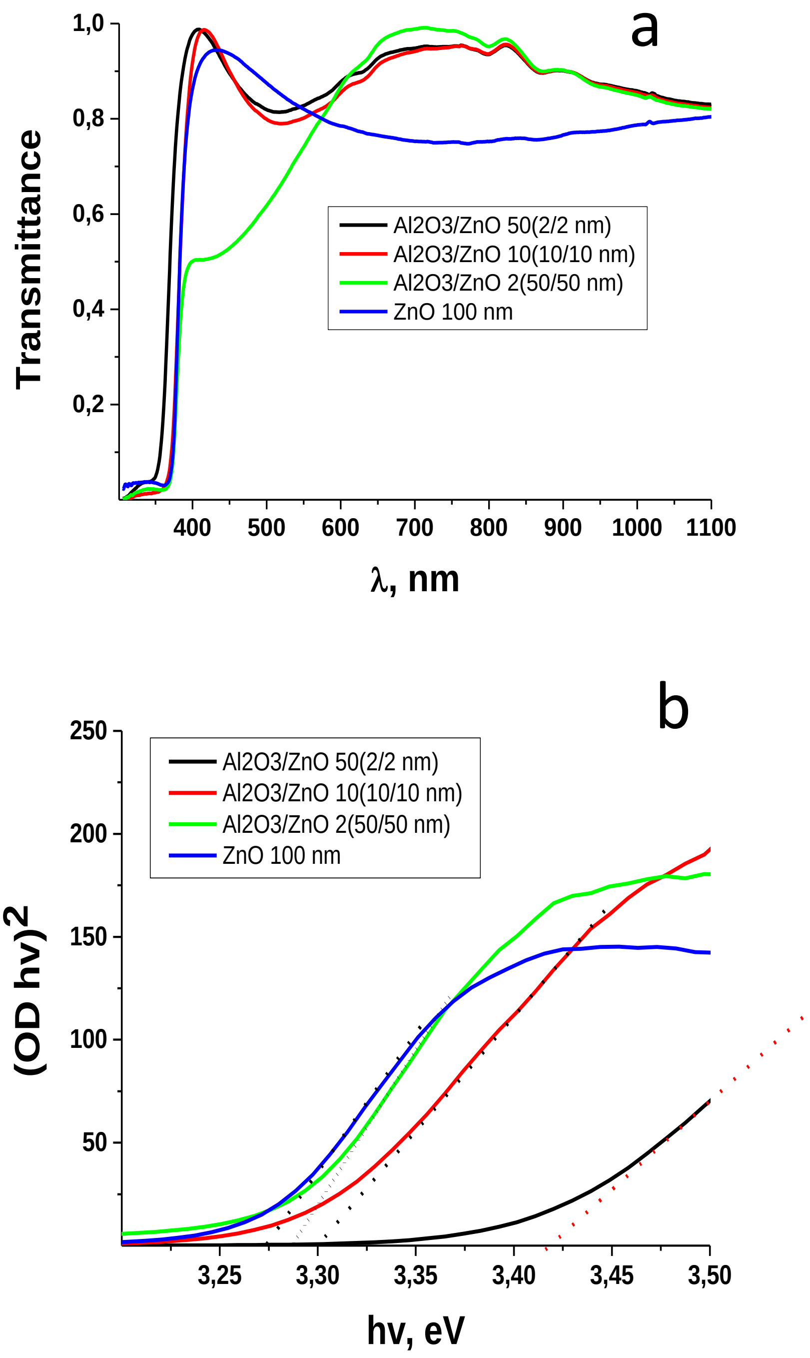

Fig. 3.16 *The transmittance spectra (a) and band gap (b) of single ZnO thin film and* Al_2O_3*/ZnO nanolaminates with different bilayer thickness.*

It was reported in [59,60] that pure ZnO single layer sample (thickness 50 nm) consists of nanocrystallites with 6 nm of grain size and a band gap (E_g) of this layer was about 3.24 eV. Also it was showed that E_g value increased when amorphous film became nanocrystalline [60].

As it was mentioned before, the Al_2O_3 layer stimulates ZnO growth and improves the crystallinity of the films. However, the grain size of Al_2O_3/ZnO 2 (50/50 nm) nanolaminates was twice higher if compared with 50 nm thick layer of ZnO. Considering this fact, it is reasonable to suppose that the blue shift, which is related to the size effects, can occur only for nanolaminates with bilayer thickness of 4 nm. For other samples, which were based on 20 and 100 nm thick bilayers, the doping by Al and improvement of the crystalline structure are the most plausible explanations for observed blue shift [110, 111].

Spectroscopic ellipsometry. This technique has been applied for the investigation of the thickness and the optical constants (refractive index and extinction coefficients) of single ZnO and Al_2O_3 layers as well as the evaluation of nanolaminates (Figure 3.17). The regression analysis was performed applying different types of models. ZnO layer was characterised using Psemi-MO and two Gausian oscillators from "Complete Ease" software. For characterisation of Al_2O_3 layers Cauchy dispersion function was selected. It is commonly used for transparent materials such as dielectrics and semiconductors. Firstly, optical constants and layer thickness of single Al_2O_3 and ZnO layers deposited on Si substrate were obtained. It was done by fixing the thickness value and fitting the dispersion function. The values of Cauchy function used for Al_2O_3 characterisation coefficients $A = 1.716$, $B=2.36\times10^{-2}$ and $C=1.57\times10^{-3}$ and a thickness of layer ($d = 40.81$nm) were determined from regression analysis. This optical constant value is close to that reported in [116] on α -$A1_2O_3$ lattice belongs to the trigonal crystal system. The single layer of ZnO optical constants and layer thickness ($d = 48.63$nm) was obtained from regression analysis with following Psemi-Mo oscillator values: Amp1 = 2.542, Br1=0.0798, Eo1=3.288, WR1=2.2419, PR1=0.631, AR1=0.542, O2R1=-0.565, Gaussians oscillator values were: Amp2 = 2.53, Br2 = 2.53, En2 =6.47, Amp3=0.265, Br3=0.46, En3=0.885. The calculated optical constants of ZnO nanolayers prepared using ALD is in good agreement with ZnO having hexagonal crystals structure [117].

In order to study the optical response of ellipsometric parameters of multilayer system (nanolaminates) composed of Al_2O_3 and ZnO layers deposited by ALD method during regression analysis, the thicknesses of layers were fixed parameters, meanwhile coefficients in optical dispersion functions were free fitting values. As noted above, the obtained optical constants for single Al_2O_3 and ZnO layers were used as a starting point for the regression analysis based evaluation of ZnO/Al_2O_3 nanolaminates.

For the Al_2O_3/ZnO 50 (2/2 nm) nanolaminate, the Bruggeman effective media approach was used for regression analysis. Firstly, the total thickness was obtained in a range from 400 nm to 1000 nm. After that the coefficients of optical constants functions were fitted in spectral range from 300 to 1000 nm to evaluate the peculiarity in UV range. Bruggeman effective media approximation model gives possibility to evaluate the percentage of materials from which the layer consists and usually is used for the evaluation of polycrystalline materials. After the fitting of experimental curves using effective media model ("Complete Ease" software), it was calculated that the part of Al_2O_3 takes 54.9 % and ZnO 45.1 % of total volume. It has to be noted that due to the roughness of the interface between layers, the ultrathin (about 2 nm) layers fluctuations can be of the same order as the thickness of this layer. It can be seen from XRD measurements that thickness of amorphous layers is below 2 nm. This means that such nanolaminates are more close to the dispersed system than to the regular one. Thus, the effective medium approach could be an enough good tool for calculation of the effective refractive index. Since the exact shape of such fluctuations is unknown, the Bruggeman approach is most preferable because it is better to use it in the case of absent of any independent information about microstructure, film roughness and intermixed layer effects [118,119]. However the investigation of nanolaminates using He-ion microscope reported elsewhere had demonstrated layered structure of the total film [56, 57]. In order to estimate the error which could be generated due to this anisotropic structure the linear approach of effective medium and Hashin – Shtrikman limit [56] with known volume fractions of the components (55%/45%) was used. This estimation showed that the difference between dielectric constants along and perpendicular to the nanolaminate structures is only 0.1%. This demonstrates that choice of Bruggeman effective medium approach is able to give enough accurate results. The main parameters of single ZnO and Al_2O_3 layers (refractive index n and extinction coefficient k) were calculated from ellipsometry measurements. It was found that Al_2O_3 was transparent in the whole UV and Vis range of the wavelength (Figure 3.17 A). It has to be noted that ellipsometry allows to obtain optical constants n (real part of refractive index) and k (imaginary part of refractive index). This was used in the present work: n *vs*. wavelength was plotted to analyze correlation with the structural properties. However, no drastic changes in n values were observed when n, sqrt($n^2 - k^2$) and sqrt($n^2 + k^2$) was ploted in the UV-Vis range.

ZnO single layer demonstrated absorption peak in the range from 360 nm to 410 nm (Figure 3.17 B). It is known that extinction coefficient k and absorption coefficient α is related as: [120]

$$\alpha = \frac{4 \cdot \pi \cdot k}{\lambda}; \qquad (3.8)$$

Where λ is a wavelength. Using equations 3.7 and 3.8 the band gap values of ZnO single layer were calculated (Table 3.3). The E_g values were similar to the ones, obtained by transmittance spectroscopy (see Figure 3.17 B). It was found that average refractive index of ZnO single layer in nanolaminates was higher than that for the single ZnO films. No drastic changes in refractive index of ZnO in nanolaminates were observed in the range from 450 to 700 nm wavelength. The peak between 350 and 400 nm corresponds to the band gap transition of ZnO [121].Blue shift of the peaks in dispersion curves $n = f(\lambda)$ were observed with the decrease of the single ZnO layer thickness in nanolaminates due to grain size decrease, doping by Al or the improvement of the crystalline quality [122]. The observed blue shift peak is in good correlation with the calculated band bap values.

It is known that doping of ZnO by Al resulted in changes of optical properties, such as band gap and refractive index [122,123] and that refractive index of ZnO doped by Al decreased with the concentration ratio of Al-dopant [123, 124]. The observed results of refractive index of ZnO showed the

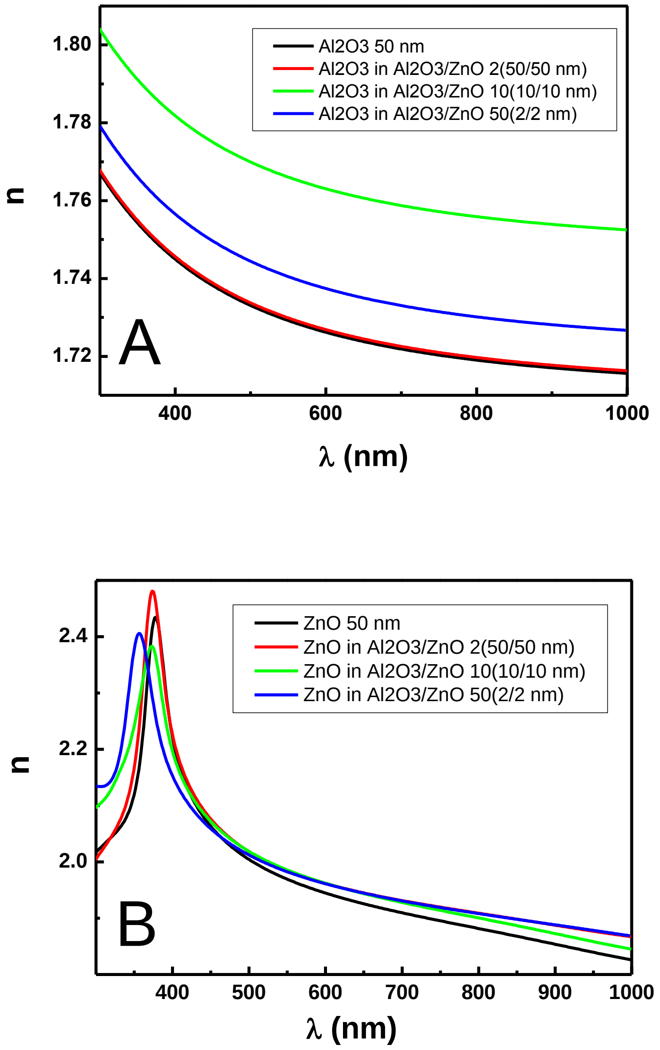

Fig. 3.17 *A) Refractive index (real part) of single Al_2O_3 film and Al_2O_3 in Al_2O_3/ZnO nanolaminates with different bilayer thicknesses. B) Refractive index (real part) of single ZnO film and ZnO in Al_2O_3/ZnO nanolaminates with different bilayer thicknesses.*

increase of refractive index in comparison to single ZnO films. Recently, it was demonstrated that 50 nm ZnO film on Si was barely nanocrystalline with average grain size about 6 nm [116]. It was considered that shift of the refractive index is related to the packing density of the film: [123,124,125] as the packing density increases, the *n* value increases [123,125,126]. In fact the packaging density (density per volume) is related to the microstructure of the films. The higher is this density the less moisture/voids are inside ZnO thin film. ZnO has a columnar microstructure and a columnar growth is proved. During the deposition of ZnO on Al_2O_3 the lateral growth can take place. The deviation from the columnar growth can change then the microstructure and the packing density changes. This induce an increase of refractive index as reported by Krishna *et al.* [126]. According to the XRD analysis, the larger grain size in nanolaminates increased with the bilayers thickness. It might be considered that no significant doping occurred in ZnO single layers, but the increase of refractive index of ZnO was due to improved crystalline properties. Thus, the Al doping at the ZnO/Al_2O_3 interface did not make an influence to the refractive index of ZnO layers.

The refractive index of Al_2O_3 single layer in nanolaminates increased in comparison to single layer of Al_2O_3, deposited on Si (Figure 3.17 B). This layer had amorphous structure [56]. In the present work Al_2O_3 also had amorphous nature as no XRD peaks, related to this material were observed. This result is not fully understood yet, however, it could result of the improvement of amorphous Al_2O_3 structure, similar to ZnO, which resulted in the increase of the refractive index and/or the Zn incorporation at the ZnO/Al_2O_3 interface.

Photoluminescence. The photoluminescence spectra of nanolaminates are shown in Figure 3.18, demonstrating UV and Vis emission bands, usually observed in ZnO nanostructures. The UV peak corresponds to free exciton emission and the Vis peak is observed due to defect level emission [112]. The intensity of UV peak increased with the increase of the bilayer thickness in the nanolaminates. The intensity of the Vis band does not follow the same tendency. The ratio of UV/Vis emission could be a parameter of the crystalline structure quality of ZnO inside the nanolaminates [127,128].

The low intensity of UV in Al_2O_3/ZnO 50 (2/2 nm) could be effected by high surface-to-volume ratio of the nanocrystalline ZnO. It was shown [129] that in ZnO quantum dots the UV/Vis ratio increased with the quantum dot (QD) radius. The low intensity of UV emission of QD could be attributed to the domination of the surface defect irradiative recombination and the separation of photogenerated charges between volume and surface of QD [130]. The PL spectra of the nanolaminates were analyzed by Origin 7.0 software by splitting the spectra on separate peaks with the Gaussian fitting. The obtained data is presented in the table 3.4.

Table 3.4. *Peak positions of ZnO single thin film and Al_2O_3/ZnO nanolaminates with different bilayer thicknesses.*

Al_2O_3/ZnO 50 (2/2 nm)	**Al_2O_3/ZnO 10 (10/10 nm)**	**Al_2O_3/ZnO 2 (50/50 nm)**	**ZnO (50 nm)**
425.3	380	378	382
560.5	389	386	391
653.1	414	417	406
-	566	552	518
-	660	637	619

Excitonic peaks at 377-378 nm and phonon replicas at 386-388 nm correlate well with the previously published results [131,132]. Peaks at 413-425 nm could be induced by neutral Zn vacancies and surface defects [132, 133]. Peaks at 536-565 nm and 635-656 nm correspond to oxygen vacancies and the interstitial oxygen [53]. It was mentioned that UV/Vis intensity of nanolaminates did not increase monotonically with the increase of the single layer thickness (Figure 3.18). It could be affected by structural changes appearing during the layer growth and doping by Al. In [114] it was demonstrated that Al^{3+} ions could substitute Zn^{2+} and therefore Zn vacancies are formed. These vacances increased the visible PL band. Additionally, Al doping results in the increase of the electron concentration what could stimulate the defect-based luminescence [114]. Doping by Al also stimulated the formation of surface defects, which could be a luminescence centers as well [114].

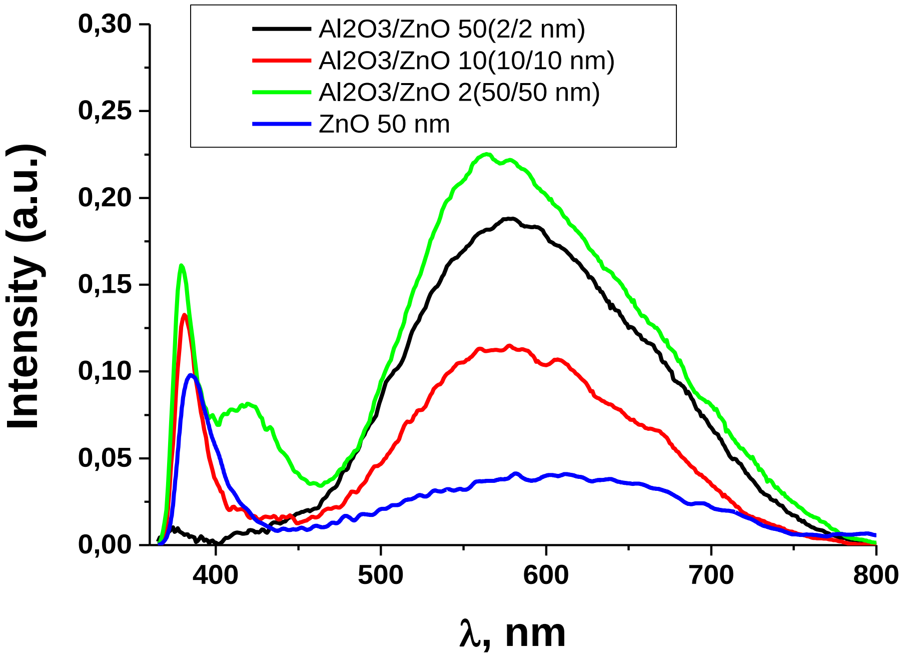

Fig. 3.18 *Photoluminesacnce spectra of 50 nm thick single ZnO film and* Al_2O_3*/ZnO nanolaminates with different bilayer thicknesses.*

Additional defects at Al_2O_3/ZnO interface could be formed, what is confirmed by relatively strong peak at 413 nm (Figure 3.18). It was shown that peaks at 413-426 nm were related to neutral Zn vacancies and Zn interstitials

[133,134,135]. Because no doping by Al was approved with ellipsometry and XRD measurements, the increase of the peak intensity could be the result of higher concentration of Zn vacancies and Zn interstitials at Al_2O_3/ZnO interface, as it is described above.

The obtained nanolaminates are biocompatible and suitable for surface modification. At room temperature, enhanced photoluminescence of Al_2O_3/ZnO 50 (2/2 nm) could be exploited as a platform for the development of new optical sensors and biosensors.

Conclusion: section 3.4

In conclusion, optical and structural properties of Al_2O_3/ZnO nanolaminates, deposited by ALD are reported. The ALD methods allow the tailoring of structural and optical parameters of the nanolaminates, including single layer thickness, grain size, band gap and PL. From analysis of optical and structural properties, it was determined that during the synthesis, the formed ZnO single layer in the nanolaminates was not doped by Al. The possible mechanism of nanolaminate formation implies that Al diffused into the interface of ZnO/Al_2O_3 bilayer forming defect states what increased visible band of PL. Blue shift of band gap and excitonic peak position of ZnO single layers were explained by quantum confinement effect and the improvement of crystalline quality of ZnO layer. The advanced properties of the nanolaminates such as biocompatibility, easy surface modification and enhanced photoluminescence at room temperature could provide good capacity for the development of nanolaminates based optical sensors and biosensors.

General conclusions

1. The analysis of the ellipsometric parameters obtained by the total internal reflection method (TIRE) has shown that the layer prepared from the antibody against BLV by indirect immobilization via a 11-MUA self-assembled monolayer of mercaptoundecanoic acid and EDC-NH-antibody linking groups can interact with a 2.5 times higher amount of the BLV antigen layer when compared to the randomly oriented intact antibody layer prepared by direct immobilization onto a Au thin film surface. For this reason, it can be concluded that the fragmented antibody layer deposited onto a nanometer thick Au film can be very suitable for the design of BLV immune-sensors.
2. For BLV antigen sensing, it is preferable to use the ellipsometric parameter Δ whose analytical sensitivity is 5.89 times better when compared to the sensitivity for the Ψ parameter. This demonstrates that the application of the ellipso-metric method for BLV sensing is preferable compared to the measurement of SPR, which in fact, measures the parameter Ψ.
3. The application of TIRE for the *in-situ* study of the immobilization of fragmented and intact antibodies against BLV and the antibodies interaction with the BLV antigen glycoprotein *gp*51 shows that the sensitivities of Ψ (t) and Δ (t) were nonlinear and different at different stages of the formation of the bio-molecular layer. The Δ (t) shows a larger sensitivity at the initial phase of the process, while Ψ (t) is less sensitive at the initial phase. Therefore, this fact should be taken into account during the evaluation of the formation of the biomolecular layer formation kinetics.
4. Analysis based on the partial reversibility model has shown that the residence time effect has to be taken into consideration in both cases: (i) when determining the affinity constants of the fragmented and intact antibodies against BLV in the immobilization kinetics study and (ii) when characterizing the immobilized antibodies against BLV interaction with the BLV antigen. In the case of the fragmented antibody interaction with the gold layer, the residence time was relatively short (≈25 times) when compared with that

obtained for the interaction of the intact antibodies with the 11-MUA-based self-assembled monolayer. In contrast, the residence time of the BLV antigen interaction with the fragmented antibody against BLV monolayer was longer (≈ 8 times) than that calculated for the BLV antigen interaction with the intact antibody layer.

5. The preparation of the immune-sensor using the BLV fragmented antibody based sensing layer is faster than that using the intact BLV antibody-based layer. The preparation of the sensor based on the intact antibody based layer takes a minimum 1.5min. However, due to the slower association of the fragmented BLV antibody-based layer with the BLV antigen, this kind of layer is more preferable for multi-fold use immune-sensors and even for implantable sensors, while the intact antibody-based layer with its faster association with the antigen, is more suitable for the development of immune-sensors with inhanced selectivity and sensitivity.
6. The application of the spectroscopic dynamic TIRE method for the characterization of the *in-situ* interactions of the monomeric and dimeric granulocyte colony stimulating factor with its receptor immobilized onto a thin gold layer demonstrated that this method in its spectroscopic dynamic acquisition mode is able to reveal minuscule differences of the association and dissociation times. This can be realized through the precise determination of the refractive index dispersion and the elimination of signal non-linearity using regression analysis of the spectroscopic ellipsometry data.
7. From the analysis of these optical and structural properties, it was determined that during the synthesis of the Al_2O_3/ZnO nanolaminates prepared by atomic layer deposition methods, the ZnO single layer was not doped by Al, which, most probably, diffused into the interface of the ZnO/Al_2O_3 bilayer, forming defect states which increased the visible band of the photoluminescence. This blue shift of the band gap and the excitonic peak position of the ZnO single layers can be due to the quantum confinement effect and the improvement of the crystalline quality of the ZnO layer. The improved properties of the nanolaminates such as biocompatibility, easy surface modification and

enhanced photoluminescence at room temperature can provide an added capabilities for the development of nanolaminates based optical biosensors.

Literature

[1] R.H. Muller, J.C. Farmer „Fast, self-compensating spectral-scanning ellipsometer“ *Rev. Sci. Instrum.*, 55 , 371. (1984).

[2] Hsu-Ting Huang, L.Fred, Jr. Terry, Erratum to “Spectroscopic ellipsometry and reflectometry from gratings (Scatterometry) for critical dimension measurement and in situ, real-time process monitoring’’ *Thin Solid Films,* 468, 339–346, (2004).

[3] H. Arwin „Spectroscopic ellipsometry and biology: recent developments and challenges“, *Thin Solid Films,* 313-314, 764-774, (1998).

[4] T.Sandstrom, M. Stenberg & H. Nygren, „Visual detection of organic monomolecular films by interference colors“, *Appl. Optics* , 24, 472–479, (1985).

[5] R. Ostroff, D.Hopkins, A.B. Haeberli, W. Baouchi & B. Polisky, „Thin film biosensor for rapid visual detection of nucleic acid targets“. *Clin. Chem.* 45, 1659–1664, (1999).

[6] R. Jenison, S. Yang, A. Haeberli, and B. Polisky, „Interference-based detection of nucleic acid targets on optically coated silicon“ , *Nature Publishing Group,* http://biotech.nature.com., (2001).

[7] H. Fujiwara, „Spectroscopic Ellipsometry Principles and application“, *Wiley,* (2007).

[8] H. G. Tompkins, „Handbook of ellipsometry“, *Springer,* 129, (2005).

[9] D. De Sousa Meneses, M. Malki, & P. Echegut, „Structure and lattice dynamics of binary lead silicate glasses investigated by infrared spectroscopy“ *J. Non-Cryst. Solids* 352, 769, (2006) .

[10] K.E. Peiponen and E. M. Vartiainen, „*KRAMERS-KRONIG* relations in optical *DATA INVERSION“Phys. Rev. B,* 44, (15), 8301-8303, (1991).

[11] G. Mie. „Betreige zur optik truber medien speziell koloidaller metalosungen“. *Ann Phys.,* 25, 377-445, (1908).

[12] D. E. Aspnes, „Optical properties of thin films“. *Thin Solid Films,* 89, 249–262, (1982).

[13] G. A. Niklasson, C. G. Granqvist, and O. Hunderi, „Effective medium models for the optical properties of inhomogeneous materials“, *Appl. Opt.*, 20, 26–30, (1981).

[14] D. A. G. Bruggeman, „Berechnung serschiedener physicalischer konstanten von heterogenen substanzen“, *Ann. Phys.* (Leipzig), 24, 636-679, (1935).

[15] J. Homola, S.S. Yee, G. Gauglitz, „Surface plasmon resonance sensors: review“, *Sensors and Actuators B – Chemical*, 54, 3-15, (1999).

[16] P.B. Johnson, R.W. Christy, „Optical-Constants of Noble-Metals“, *Phys. Rev. B,* 6, 4370–4379, (1972).

[17] C.G. Granqvist, „Transparent conductors as solar energy materials: A panoramic review“, *Sol. En. Mat. and Sol. Cells*, 91, 1529–1598, (2007).

[18] J.Talbot, “Time dependent desorption: A memory function approach”, *Adsorption*, 2, 89–94, (1996).

[19] M.J. Mura-Galelli , J.C Voegel , S. Behr, E.F. Bres, P. Schaaf, „Adsorption/desorption of human serum albumin on hydroxyapatite: a critical analysis of the Langmuir model“, *Proc Natl Acad Sci U S A.*, 88, (13), 5557-6190, (1991).

[20] T.E. Miller, “Killing and Lysis of Gram-negative Bacteria Through The Synergistic Effect of Hydrogen Peroxide, Ascorbic Acid, and Lysozyme", *J. Bacteriol.*, 98, (3), 949–955, (1969).

[21] N. Gillet, A. Florins, M. Boxus1, C. Burteau, A. Nigro, F. Vandermeers, H. Balon, A.B. Bouzar, J. Defoiche, A. Burny, M. Reichert, R. Kettmann and L. Willems ” Mechanisms of leukemogenesis induced by bovine leukemia virus: prospects for novel anti-retroviral therapies in human“. RETROVIROL., 4, 18, (2007).

[22] J.G. Santos, M.Voemel, R.Struck, U.Hombert, D.R.Naessel, C.Wegener, „Neuroarchitecture of peptidergic systems in the larval ventral ganglion of Drosophila melanogaster“, *PLoS ONE*, 2, (8), (2007).

[23] P.Kerkhofs, J-S. Gatot, K. Knapen, M. Mammerickx, A. Burny, D. Portetelle, L. Willems and R. Kettmann, “Long-term protection against bovine leukemia virus replication in cattle and sheep”, *J Gen Virol April.*, 81, 4, 957-963, (2000).

[24] A. Ramanaviciene, A. Ramanavicius, “Molecularly imprinted polypyrrole-based synthetic receptor for direct detection of bovine leukemia virus glycoproteins”, *Biosens Bioelectron.*, 15, 20, (6), 1076-82, (2004).

[25] B. Kurtinaitiene, D. Ambrozaite, V. Laurinavicius, A. Ramanaviciene, A. Ramanavicius “Amperometric immunosensor for diagnosis of BLV infection”, *Biosens Bioelectron.*,15, 23, (10), 1547-54, (2008).

[26] A. Ramanavicius, A. Finkelsteinas, H. Cesiulis, A. Ramanaviciene, “Electrochemical impedance spectroscopy of polypyrrole based electrochemical immunosensor”, *Bioelectrochemistry*. 79, (1), 11-6, (2010).

[27] A. Ramanavičienė, G. Stalnionis, A. Ramanavičius, “Piezoelectric affinity biosensor for diagnosing of bovine leukemia”, *Biologija*, 1, 33–35, (2004).

[28] L.V. Pyrohova , M.F. Starodub , V.P. Artiukh , L.I. Nahaieva , H.I. Dobrosol, “Express diagnostics of bovine leucosis by immune sensor based on surface plasmon resonance”, *Ukr Biokhim Zh.*, 3, 88-92, (2002).

[29] L.V. Pyrohova, M.F. Starodub , L.I. Nahaeva, “Detection of the level of antibodies against bovine leucosis virus in the cow milk by immune sensor”, *Ukr Biokhim Zh*. Mar-Apr, 77, 2, 166-8, (2005).

[30] J. Baniukevic, J.Kirlyte, A. Ramanavicius, A.Ramanaviciene, “Comparison of oriented and random antibody immobilization techniques on the efficiency of immunosensor”, *Proc. En.*, 47, 837 – 840, (2012).

[31] A.M. Cohen, K.M. Zsebo, H. Inoue, D. Hines, „*In vivo* stimulation of granulopoiesis by recombinant human granulocyte colony-stimulating factor“. *Proc. Natl. Acad. Sci. U. S. A.*, 84, 2484-2488, (1987).

[32] V. Caggiano, R.V. Weiss, T.S. Rickert, W.T. Linde-Zwirble, „Incidence, cost, and mortality of neutropenia hospitalization associated with chemotherapy“, *Cancer*, 103, 1916, (2005).

[33] M.A. Foote, G. Morstyn, “Granulocyte colony-stimulating factor: biology and clinical potential, in: R.K Oldham, R.O. Dillman (Eds.)”, *Prin. Canc. Biother.*, 569-580, (2009).

[34] B.Huggett, J. Hodgson, R.Lähteenmäki, “Public biotech 2010-the numbers”, *Nat Biotechnol.*, 29, 7, 585-591, (2011).

[35] B.I. Lord, L.B. Woolford, G. Molineux, “Kinetics of Neutrophil Production in Normal and Neutropenic Animals during the Response to Filgrastim (r-metHu G-CSF) or Filgrastim SD/01 (PEG-r-metHu G-CSF)”, *Clin Cancer Res.*, 7, 2085-2090, (2001).

[36] M. Yamasaki, N. Konishi, K. Yamaguchi, S. Itoh, Y. Yokoo, “Purification and characterization of recombinant human granulocyte colony-stimulating factor (rhG-CSF) derivatives: KW-2228 and other derivatives”, *Biosci Biotechnol Biochem.*, 62, 8, 1528-1534, (1998).

[37] S. Jevševar, M. Kunstelj, V.G. Porekar, “Pegylation of therapeutic proteins”, *Biotechnology Journal.*, 5, 113-128, (2010).

[38] F. Campabadal, J.M. Rafi, M. Zabala, O. Beldarrain, „Electrical characteristics of metal-insulator-semiconductor structures with atomic layer deposited Al2O3, HfO2, and nanolaminates on different silicon substrates“, *J. Vac. Scie. and Tech. B.*, 23, (2011).

[39] T.J. Park, J.H. Kim, J.H. Jang, C-K. Lee, K.D. Na, S.Y. Lee, H-S. Jung, M. Kim, S. Han, C.S. Hwang, „Reduction of electrical defects in atomic layer deposited HfO2 films by Al doping“, *Chemistry of Materials*, 22, 4175–4184, (2010).

[40] Y.W. Chen, M. Liu, T. Kaneko, P.C. McIntyre, „Atomic layer deposited hafnium oxide gate dielectrics for charge-based biosensors“, *Electrochemical and Solid State Letters*, 13 G29–G32 (2010).

[41] S. Logothetidis, A. Laskarakis, S. Kassavetis , S. Lousinian, C. Gravalidis, G. Kiriakidis, „Optical and structural properties of ZnO for transparent electronics“, *Thin Solid Films*, 516, 1345–1349, (2008).

[42] P.P. Sahay, R.K. Nath, „Al-doped ZnO thin films as methanol sensors „*Sens. Actuators B*, 134,, 654 (2008).

[43] T. Shuler, M.A. Aegerter, „Optical, electrical and structural properties of sol gel ZnO:Al coatings„ *Thin Solid Films*, 351, 125, (1999).

[44] Y. Natsume, H. Sakata, „Zinc oxide films prepared by sol-gel spin-coating „ *Thin Solid Films*, 372, 30, (2000).

[45] Y. Zhou, P.J. Kelly, A. Postill, O. Abu-Zeid, A.A. Alnajjar, „The characteristics of aluminium-doped zinc oxide films prepared by pulsed magnetron sputtering from powder targets“, *Thin Solid Films*, 447, 33, (2004).

[46] Z. Serbetcø, H.M. El-Nasserb, Fahrettin Yakuphanogluc, „Photoluminescence and refractive index dispersion properties of ZnO nanofibers grown by sol–gel method“, *Spectrochimica Acta Part* A., 86, 405–409, (2012).

[47] Banerjee, P.; Lee, W.-J.; Bae, K.-R.; Lee, S. B.; Rubloff, G. W. *Journal of Applied Physics*, 108, (4), (2010).

[48] L.Karvonen, A.Säynätjoki, Y.Chen, H.Jussila, J.Rönn, M.Ruoho, T.Alasaarela, S.Kujala, R.A. Norwood, N. Peyghambarian, K. Kieu, S. Honkanen, „Enhancement of the third-order optical nonlinearity in ZnO/Al2O3 nanolaminates fabricated by atomic layer deposition” *Applied Physics Letters*, 103, (3), (2013).

[49] R. Ostroff, D.Hopkins, A.B. Haeberli, W. Baouchi & B. Polisky, „Thin film biosensor for rapid visual detection of nucleic acid targets“, *Clin. Chem.* 45, 1659–1664, (1999).

[50] W.M. Albers, S. Auer, H. Helle, T. Munter, I. Vikholm-Lundin, „Functional characterisation of Fab_-fragments self-assembled onto hydrophilic gold surfaces“, *Colloid Surface B.*, 68, 193–199, (2009).

[51] E. Mistiniene, J.H. Pesliakas, M. Pleckaityte, G. Zvirblis, „Patent application No.WO2013022328“(A1), (2013).

[52] J. Elias, I. Utke, S. Yoon, M. Bechelany, A. Weidenkaff, J. Michler, L.Philippe, „Electrochemical Growth of ZnO Nanowires on Atomic Layer Deposition Coated Polystyrene Sphere Templates“, *Electrochim. Acta*, 110, 387−392, (2013).

[53] J. A. R.Marquez, C. M. B Rodriguez, C. M. Herrera, E. R. Rosas, O. Z. Angel, O. T. Pozos, „Effect of Surface Morphology of ZnO Electrodeposited on Photocatalytic Oxidation of Methylene Blue Dye Part I: Analytical Study“, *Int. J. Electrochem. Sci.*, 6 (9), 4059− 4069, (2011).

[54] A. J. Reddy, M. K. Kokila, H. Nagabhushana, J. L. Rao, C. Shivakumara, B. M. Nagabhushana,; R. P. S. Chakradhar, „Combustion Synthesis, Characterization, and Raman Studies of ZnO Nanopowders“, *Spectrochim. Acta, Part A,* 81, (1), 53−58, (2011).

[55] U. Holzwarth, N. Gibson, „The Scherrer Equation versus the “Debye-Scherrer Equation“, *Nat. Nanotechnol.*, 6, (9), 534−534, (2011).

[56] R. Raghavan, M. Bechelany, M. Parlinska, D. Frey, W. M. Mook, A. Beyer, J. Michler, I. Utke, „Nanocrystalline-to-Amorphous Transition in Nanolaminates Grown by Low Temperature Atomic Layer Deposition and Related Mechanical Properties“, *Appl. Phys. Lett.*, 100 (19), 191912, (2012).

[57] N. P. Dasgupta, S. Neubert, W. Lee, O. Trejo, J.-R. Lee, F. B. Prinz, „Atomic Layer Deposition of Al-Doped ZnO Films: Effect of Grain Orientation on Conductivity“, *Chem. Mater.*, 22, (16), 4769−4775, (2010).

[58] J. W. Elam, Z. A. Sechrist, S. M. George, „ZnO/Al2O3 Nanolaminates Fabricated by Atomic Layer Deposition: Growth and Surface Roughness Measurements“, *Thin Solid Films*, 414, (1), 43−55, (2002).

[59] A. Abou Chaaya, R. Viter, M. Bechelany, Z. Alute, D. Erts, A. Zalesskaya, K. Kovalevskis, V. Rouessac, V. Smyntyna, P. Miele, „Evolution

of Microstructure and Related Optical Properties of ZnO Grown by Atomic Layer Deposition“, *Beilstein J. Nanotechnol.*, 4, 690−698, (2013).

[60] T. Wang, H. Wu, C. Chen, C. Liu, „Growth, Optical, and Electrical Properties of Nonpolar M-Plane ZnO on p-Si Substrates with Al2O3 Buffer Layers“, *Appl. Phys. Lett.*, 100, (1), 011901, (2012).

[61] A. Suchodolskis, A. Stirke, A. Timonina, A. Ramanaviciene, A. Ramanavicius, „Baker's yeast transformation studies by atomic force microscopy“, *Adv. Sci. Lett.*, 4 , 171–173, (2011).

[62] P.B. Johnson, R.W. Christy, „Optical Constants of the Noble Metals“, *Phys. Rev. B* 6, 4370, (1972).

[63] Z. Balevicius, V. Vaicikauskas, G. J. Babonas, „The role of surface roughness in total internal reflection ellipsometry of hybrid systems“, *Appl. Surf. Sci.*, 256, 640, (2009).

[64] A. Kausaite-Minkstimiene, A. Ramanaviciene, A. Ramanavicius, „Surface plasmon resonance biosensor for direct detection of antibodies against human growth hormone“, *Analyst*, 134, 2051–2057, (2009).

[65] R. Iwata, R. Satoh, Y. Iwasaki, K. Akiyoshi, „Covalent immobilization of antibody fragments on well-defined polymer brushes via site-directed method“, *Colloid Surface B.,* 62, 288–298, (2008).

[66] C.A. Betty, „Highly sensitive capacitive immunosensor based on porous siliconpolyaniline structure: bias dependence on specificity“, *Biosens. Bioelectron.*, 25, 338–343, (2009).

[67] Z. Matharu, A. J. Bandodkar, G. Sumana, P. R. Solanki, E.M.I.M. Ekanayake, K. Kaneto, V. Gupta, B. D. Malhotra, „Low density lipoprotein detection based on antibody immobilized self-assembled monolayer: investigations of kinetic and thermodynamic properties“, *J. Phys. Chem. B,* 113, 14405–14412, (2009).

[68] K. Bonroy, F. Frederix, G. Reekmans, E. Dewolf, R. De Palma, G. Borghs, P. Declerck, B.J. Goddeeris, „Comparison of random and oriented

immobilisation of antibody fragments on mixed self-assembled monolayers“, *J. Immunol. Methods* , 312, 167–181, (2006).

[69] Y.M. Bae, B.K. Oh, W. Lee, W.H. Lee, J.W. Choi, „Study on orientation of immunoglobulin G on protein G layer“, *Biosens. Bioelectron.*, 21, 103-110, (2005).

[70] T. M. Spitznagel, D. S. Clark, „Surface-density and orientation effects on immobilized antibodies and antibody fragments“, *Biotechnology.*, 11, 825–829, (1993).

[71] Z. Balevicius, R. Drevinskas, M. Dapkus, G. J. Babonas, A. Ramanaviciene, A. Ramanavicius, „Total internal reflection ellipsometry of metal–organic compound structures modified with gold nanoparticles“, *Thin Solid Films,* 519, 2959–2962, (2011).

[72] A. Kausaite-Minkstimiene, A. Ramanaviciene, J. Kirlyte, A. Ramanavicius, „A comparative study of random and oriented antibody immobilization techniques on the binding capacity of immunosensor“, *Anal. Chem.*, 82, 6401–6408, (2010).

[73] A.A. Karyakin, G.V. Presnova, M.Y. Rubtsova, A.M. Egorov, „Oriented immobilization of antibodies onto the gold surfaces via their native thiol groups“, *Anal. Chem.*, 72, 3805–3811, (2000).

[74] I. Vikholm-Lundin, „Immunosensing based on site-directed immobilization of antibody fragments and polymers that reduce nonspecific binding“, *Langmuir*, 21, 6473–6477, (2005).

[75] I. Vikholm, „Self-assembly of antibody fragments and polymers onto gold for immunosensing“, *Sens. Actuators B.*, 106, 311–316, (2005).

[76] Y.G. Lee, K.S. Chang, „Application of a flow type quartz crystal microbalance immunosensor for real time determination of cattle bovine ephemeral fever virus in liquid“, *Talanta*, 65, 1335–1342, (2005).

[77] H. Arwin, M. Poksinski, K. Johansen, „Total internal reflection ellipsometry: principlesand applications“, *Appl. Opt.*, 43, 3028–3036, (2004).

[78] A.V. Nabok, A. Tsargorodskaya, A. Holloway, N. F. Starodub, O. Gojster, „Registration of T-2 mycotoxin with total internal reflection ellipsometry and QCM impedance methods“, *Biosens. Bioelectron.*, 22, 885–890, (2007).

[79] S. D’Elia, N. Scaramuzza, F. Ciuchi, C. Versace, G. Strangi, R. Bartolino, „Ellipsometry investigation of the effects of annealing temperature on the optical properties of indium tin oxide thin films studied by Drude–Lorentz model“, *Appl.Surf. Sci.*, 255, 7203–7211, (2009).

[80] H. Liang, H. Miranto, N. Granqvist, J.W. Sadowski, T. Viitala, B. Wang, M. Yliperttula, „Surface plasmon resonance instrument as a refractometer for liquids and ultrathin films“, *Sens. Actuators B.*, 149, 212–220, (2010).

[81] H. Bagci, F. Kohen, U. Kuscuoglu, E.A. Bayer, M. Wilchek, „Monoclonal antibodies simulate avidin in the recognition of biotin“, *FEBS Lett.*, 322, 47–50, (1993).

[82] H. G. Thompkins, E. A. Irene, „Handbook of Ellipsometry“, *Springer-Verlag*, Berlin, Heidelberg, (2005).

[83] H. Arwin, „Optical properties of thin layers of bovine serum albumin, gammaglobulin, and hemoglobin“, *Appl. Spectrosc.*, 40, 313–318, (1986).

[84] A. Ramanaviciene, V. Snitka, R. Mieliauskiene, R. Kazlauskas, A. Ramanavicius, „AFM study of complement system assembly initiated by antigen–antibody complex“, *Cent. Eur. J. Chem.*, 4, 194–206, (2006).

[85] J. S. H. Armstrong, M. J. E. Budka, K. C. Morrison, M. Hasson, „Preparation and properties of serum and plasma proteins. XII. The refractive properties of the proteins of human plasma and certain purified fractions“, *J. Am. Chem. Soc.*, 69, 1747–1753, (1947).

[86] H. G. Rubahn, H. Sitter, G. Horowitz, K. Al-Shamery, „Interface Controlled Organic Thin Films“, *Springer-Verlag*, Berlin, Heidelberg, (2009).

[87] C. D. Bain, E. B. Troughton, Y.-T. Tao, J. Evall, G. M. Whitesides, R. G. Nuzzo, „Formation of monolayer films by the spontaneous assembly of

organic thiols from solution onto gold“, *J. Am. Chem. Soc*., 111, 321–335, (1989).

[88] E. L. Smith, C. A. Alves, J. W. Anderegg, M. D. Porter, L. M. Siperko, „Deposition of metal overlayers at end-group-functionalized thiolate monolayers adsorbed at Au. 1. Surface and interfacial chemical characterization of deposited Cu overlayers at carboxylic acid-terminated structures“, *Langmuir*, 8, 2707–2714, (1992).

[89] M. Sastry, „A note on the use of ellipsometry for studying the kinetics of formation of self-assembled monolayers“, *Bull. Mater. Sci*., 23, 159–163, (2000).

[90] M. D. Porter, T. B. Bright, D. L. Allara, C. E. D. Chidsey, „Spontaneously organized molecular assemblies. 4. Structural characterization of n-alkyl thiol monolayers on gold by optical ellipsometry, infrared spectroscopy, and electrochemistry“, *J.Am. Chem. Soc*., 109, 3559–3568, (1987).

[91] M. Poksinski, H. Arwin, „Protein monolayers monitored by internal reflection ellipsometry“, *Thin Solid Films*, 455, 716–721, (2004).

[92] X. Jin, Z. Ma, J. Talbot, N.-H.L. Wang, „A model for the adsorption equilibria of solutes with multiple adsorption orientations“, *Langmuir*, 15, 2321–3333, (1999).

[93] A. Nabok, A. Tsargorodskaya, M. K. Mustafa, I. Szekacs, N. F. Starodub, A. Szekacs, „Detection of low molecular weight toxins using an optical phase method of ellipsometry“, *Sens. Actuators B*., 154, 232–237, (2011).

[94] N. C. H. Le, V. Gubala, R. P. Gandhiraman, C. Coyle, S. Daniels, D. E. Williams, „Total internal reflection ellipsometry as a label-free assessment method for optimization of the reactive surface of bioassay devices based on a functionalized cycloolefin polymer“. *Anal. and Bioanal. Chem*., 398, 1927–1936, (2010).

[95] Z. Balevicius, A. Ramanaviciene, I. Baleviciute, A. Makaraviciute, L. Mikoliunaite, A. Ramanavicius,“ Evaluation of intact- and fragmented-

antibody based immunosensors by total internal reflection ellipsometry“ *Sens. and Actuators B.*, 160, 555–562, (2011).

[96] S. Y. Wu, H. P. Ho, W. C. Law, Chinlon Lin and S. K. Kong, “Highly Sensitive Differential Phase-Sensitive Surface Plasmon Resonance Biosensor Based on the Mach– Zehnder Configuration,” *Optics Letters*, 29, No. 20, 2378-2380, (2004).

[97] P. P. Markowicz, W. C. Law, A. Baev, P. N. Prasad, S. Patskovsky, and A. Kabashin, “Phase-sensitive time-modulated surface plasmon resonance polarimetry for wide dynamic range biosensing,” *Opt. Express* , 15, (4), 1745–1754, (2007).

[98] A. V. Kabashin, S. Patskovsky, A. N. Grigorenko, „Phase and amplitude sensitivities in surface plasmon resonance bio and chemical sensing“, *Optics Express*, 17, 21191–21204, (2009).

[99] A. Nabok, A. Tsargorodskaya, „The method of total internal reflection ellipsometry for thin film characterisation and sensing“, *Thin Solid Films*, 516, 8993–9001, (2008).

[100] V. Kriechbaumer, A. Nabok, M. K. Mustafa, A. Rukaiah, A. Tsargorodskaya, D. P. Smith, B. M. Abell, „Analysis of Protein Interactions at Native Chloroplast Membranes by Ellipsometry“, *PloS ONE*, 7, 1–7, (2012).

[101] N. R. Pradeep, A. A. Muhammad, “Theory of 'selectivity' of label-free nanobiosensors: a geometro-physical perspective“, *J. of App. Phys.*, 107, (6), p.064701-1-064701-6, (2010).

[102] D. Goyal, A. Subramanian,”In-situ protein adsorption study on biofunctionalized surfaces using spectroscopic ellipsometry”, *Thin Solid Films*, 518, 2186–2193, (2010).

[103] V.Kriechbaumer, “Study of Receptor-Chaperone Interactions Using the Optical Technique of Spectroscopic Ellipsometry” , *Biophysical Journal*, 101, 504–511, (2011).

[104] M. K. Mustafa, A. Nabok, D. Parkinson, I. E. Tothill, F. Salam, A. Tsargorodskaya, „Detection of β-amyloid peptide (1–16) and amyloid precursor protein (APP_{770}) using spectroscopic ellipsometry and QCM techniques: A step forward towards Alzheimers disease diagnostics“, *Biosens. and Bioel.*, 26, 1332–1336, (2010).

[105] A. Nabok, A. Tsargorodskaya, F. Davis, S. P. J. Higson, "The study of genomic DNA adsorption and subsequent interactions using total internal reflection ellipsometry", *Biosens. and Bioel.*, 23, 377–383, (2007).

[106] A. Ramanaviciene, D.Virzonis, G.Vanagas, A. Ramanavicius, „Capacitive micromachined ultrasound transducer (cMUT) for immunosensor design“, *Analyst*, 135, 1531–1534, (2010).

[107] A. Makaraviciute, A. Ramanaviciene, „Site-Directed Antibody Immobilization Techniques for Immunosensors A Review“, *Biosensors and Bioelectron.*, 50, 460-471, (2013).

[108] I. Baleviciute, Z. Balevicius, A, Makaraviciute, A. Ramanaviciene, A. Ramanavicius, „Study of antibody/antigen binding kinetics by total internal reflection ellipsometry“, *Biosensors and Bioelectron*. 39, 170-176, (2013).

[109] P.Banerjee, W.-J. Lee, K.-R.Bae, S. B. Lee, G. W. Rubloff, "Structural, Electrical, and Optical Properties of Atomic Layer Deposition Al-doped ZnO Films", *J. Appl. Phys.* 108, (4), 445305, (2010).

[110] H. Cheun, C. Fuentes-Hernandez, J. Shim, Y. Fang, Y. Cai, H. Li, A. K. Sigdel, J. Meyer, J. Maibach, Dindar, "Oriented Growth of Al2O3:ZnO Nanolaminates for Use as Electron-Selective Electrodes in Inverted Polymer Solar Cells", *Adv. Funct. Mater.*, 22, (7), 1531-1538, (2012).

[111] T. Wang, H. Wu, C. Chen, C. Liu, "Growth, Optical, and Electrical Properties of Nonpolar M-plane ZnO on p-Si Substrates With Al2O3 Buffer Layers", *Appl. Phys. Lett.*, 100, (1), 011901, (2012).

[112] L. Karvonen, A. Säynätjoki, Y. Chen, H. Jussila, J. Rönn, M. Ruoho, T. Alasaarela, S. Kujala, R. A .Norwood, N. Peyghambarian, "Enhancement of

the Third-order Optical Nonlinearity in ZnO/Al2O3 Nanolaminates Fabricated by Atomic Layer Deposition", *Appl. Phys. Lett.*, 103, (3), 031903, (2013).

[113] N. R. Yogamalar, A. Chandra Bose, "Absorption–emission Study of Hydrothermally Grown Al:ZnO Nanostructures", *J. Alloys Compd.*, 509, (34), 8493-8500, (2011).

[114] N. W. Wang, Y. H. Yang,; G. W. Yang, "Great Blue-shift of Luminescence of ZnO Nanoparticle Array Constructed from ZnO Quantum Dots", *Nanoscale Res. Lett.*, 6, 338, (2011).

[115] C. Charpentier, P. Prod'homme, P. R. I.Cabarrocas, "Microstructural, Optical and Electrical Properties of Annealed ZnO:Al Thin Films", *Thin Solid Films*, 531, 424-429, (2013).

[116] A. S. Barker, "Infrared Lattice Vibrations and Dielectric Dispersion in Corundum", *Phys. Rev.*, 132, (4), 1474-1481, (1963).

[117] Z.-H. Dai, R.-J. Zhang, J. Shao, Y.-M. Chen, Y.-X. Zheng, J.-D. WU, L.-Y. Chen, "Optical Properties of Zinc-oxide Films Determined Using Spectroscopic Ellipsometry with Various Dispersion Models", *J. Korean Phys. Soc.*, 55, 1227-1232, (2009).

[118] H. V. Nguyen, I. An, R. W.Collins, "Evolution of the Optical Functions of Thin-film Aluminum: A Real-time Spectroscopic Ellipsometry Study", *Phys. Rev. B: Condens. Matter.*, 47, (7), 3947-3965, (1993).

[119] J. M. Leng, J. Chen, J. Fanton, M. Senko, K. Ritz, J.Opsal, "Characterization of Titanium Nitride (TiN) Films on Various Substrates Using Spectrophotometry, Beam Profile Reflectometry, Beam Profile Ellipsometry and Spectroscopic Beam Profile Ellipsometry", *Thin Solid Films* , 313–314, (0), 308-313, (1998).

[120] F. Yakuphanoglu, S. Ilican, M. Caglar, Y.Caglar, "The Determination of the Optical Band and Optical Constants of Non-crystalline and Crystalline ZnO Thin Films Deposited by Spray Pyrolysis", *J. Optoelectron. Adv. M.*, 9, 2180 – 2185, (2007).

[121] L. Miao, S. Tanemura, L. Zhao, X. Xiao, X. T.Zhang, “Ellipsometric Studies of Optical Properties of Er-doped ZnO Thin Films Synthesized by Sol–gel Method”, *Thin Solid Films*, 543, (0), 125-129, (2013).

[122] H. Benzarouk, A. Drici, M. Mekhnache, A. Amara, M. Guerioune, J. C. Bernède, H. Bendjffal, “Effect of Different Dopant Elements (Al, Mg and Ni) on Microstructural, Optical and Electrochemical Properties of ZnO Thin Films Deposited by Spray Pyrolysis (SP)”, *Superlattices Microstruct.***,** 52, (3), 594-604, (2012).

[123] S. W.Xue, X. T.Zu, W. G. Zheng, H. X. Deng, X.Xiang, “Effects of Al Doping Concentration on Optical Parameters of ZnO : Al Thin Films by Sol-gel Technique”, *Phys. B*, 381, (1-2), 209-213, (2006).

[124] E. N. Cho, S. Park, I. Yun, “Spectroscopic Ellipsometry Modeling of ZnO Thin Films with Various O2 Partial Pressures”, *Curr. Appl. Phys.*, 12, (6), 1606-1610, (2012).

[125] Z. B. Fang, Z. J. Yan, Y. S.Tan, X. Q. Liu, Y. Y.Wang, “Influence of Post-Annealing Treatment on the Structure Properties of ZnO Films”, *Appl. Surf. Sci.***,** 241, (3–4), 303-308, (2005).

[126] M. G. Krishna, K. N. Rao, S.Mohan, “Optical Properties of Ion Assisted Deposited Zirconia Thin Films”, *J. Vac. Sci. Technol., A*, 10, (6), 3451-3455, (1992).

[127] B. J. Jin, H. S.Woo, S.Im, S. H. Bae, S. Y. Lee, “Relationship Between Photoluminescence and Electrical Properties of ZnO Thin Films Grown by Pulsed Laser Deposition”, *Appl. Surf. Sci.*, 169–170, (0), 521-524, (2001)

[128] S. Zandi, P. Kameli, H. Salamati, H. Ahmadvand, M. Hakimi, “Microstructure and Optical Properties of ZnO Nanoparticles Prepared by a Simple Method”, *Phys. B*, 406, (17), 3215-3218, (2011).

[129] N. Abrahám, I. Dékány, “Size-dependent Photoluminescence Properties of Bare ZnO and Polyethylene Imine Stabilized ZnO Nanoparticles and their Langmuir–Blodgett Films”, *Colloids Surf., A*, 364, (1–3), 26-33, (2010).

[130] T. Omata, K. Takahashi, S. Hashimoto, Y. Maeda, K. Nose, S. Otsuka-Yao-Matsuo, K. Kanaori, "UV Luminescent Organic-capped ZnO Quantum Dots Synthesized by Alkoxide Hydrolysis with Dilute Water", *J. Colloid Interface Sci.*, 355, (2), 274-281, (2011).

[131] L. Cui, G.-G. Wang, H.-Y. Zhang, R. Sun, X.-P. Kuang, J.-C. Han, "Effect of Film Thickness and Annealing Temperature on the Structural and Optical Properties of ZnO Thin Films Deposited on Sapphire (0001) Substrates by Sol–gel", *Ceram. Int.*, 39, (3), 3261-3268, (2013).

[132] A. B.Djurišić, Y. H.Leung, "Optical Properties of ZnO Nanostructures", *Small,* 2, (8-9), 944-961, (2006).

[133] M. Willander, O. Nur, J. R. Sadaf, M. I. Qadir, S. Zaman, A.Zainelabdin, N.Bano, I.Hussain, "Luminescence from Zinc Oxide Nanostructures and Polymers and their Hybrid Devices", *Materials,* 3, (4), 2643-2667, (2010).

[134] H. Chen, J. Ding, W. Guo, F. Shi, Y. Li, "Violet–blue–green Emission and Shift in Mg-doped ZnO films with Different Ratios of Oxygen to Argon Gas Flow", *Appl. Surf. Sci.*, 258, (24), 9913-9917, (2012).

[135] A. Z. Liang, X. Yu, B. Lei, P. Liu, W. Mai, "Novel Blue-violet Photoluminescence from Sputtered ZnO Thin Films", *J. Alloys Compd.*, 509, (17), 5437-5440, (2011).

SANTRAUKA (abstract in Lithuanian)

Įvadas. Jame aprašomas darbo aktualumas, tikslas, uždaviniai, pateikiami ginamieji teiginiai ir mokslinis darbo naujumas.

1. **Skyrius. Literatūros apžvalga.** Apžvelgiamas elipsometrijos metodas, poliarizuotos šviesos sąvoka, poliarizacijos būsenos, aprašomas plonų sluoksnių optinių modelių kūrimas ir jų taikymas elipsometrinių matavimų aprašymui, nustatant sluoksnių storį ir lūžio rodiklį. Pateikiami įvairūs dielektrinės funkcijos artiniai, aprašomas paviršiaus plazmonų rezonanso reiškinys ir matematiniai modeliai, skirti biomolekulių saveikos kinetikų analizei. Šiame skyriuje glaustai pateikiamos ir žinios apie galvijų leukemijos virusą bei jo aptikimo metodus, o taip pat aprašomos granuliocitų kolonijas stimuliuojančio faktoriaus ir nanolaminatų savybės.
2. **Skyrius. Metodika.** Šiame skyriuje aprašyti disertacinio darbo metu naudoti metodai ir bandinių paruošimo technologijos. Galvijų leukemijos virusui (GLV) aptikti skirto sensoriaus formavimas, granuliocitų kolonijas stimuliuojančio faktoriaus receptoriaus, monomero ir dimero sluoksnių formavimo eiga, Al_2O_3/ZnO nanolaminatų sluoksnių formavimas naudojant atominių sluoksnių nusodinimo metodą. Pateiktos atominių jėgų mikroskopijos matavimo sąlygos. Aprašomi įvairių tipų elipsometrai, naudoti šiame darbe, baltymų kinetikų matavimo celė ir rentgeno spindulių difrakcijos matavimo sąlygos. Aprašomas bandinių charakterizavimas minėtomis metodikomis, aukso lustų modifikavimas antikūnų prieš GLV fragmentais, savitvarkiu monosluoksniu ir „neskaldytais” antikūnais prieš GLV. Paip pat pateikiamas skenuojančiu elektroniniu mikroskopu atliktas nanolaminatų sluoksnių atvaizdavimas ir storio įvertinimas.
3. **Skyrius. Skirtas imunojutiklių iš „skaldytų” ir neskaldytų antikūnų tyrimui visiško vidaus atspindžio elipsometrija [1*].** Jame pažymėta, jog elipsometrinių parametrų kinetikos tyrimai parodė, kad „skaldyti”, kryptingai

ant aukso įmobilizuoti antikūnai prieš GLV sąveikauja su 2.5 karto didesne GVL antigeno paviršine mase, nei „neskaldyti”, nekryptingai įmobilizuoti antikūnai. Didelis šio metodo jautrumas ir pritaikytas daugiasluoksnis optinis leidžia įvertinti antikūnų – antigeno sluoksnių struktūrą. Naudojant visiško vidaus atspindžio elipsometrijos metodą buvo patvirtinta, kad „skaldyti” antikūnai ant aukso įmobilizuoti kryptingai. Apskaičiuotas elipsometrinio parametro Δ (λ) jautrumas buvo 5.89 didesnis nei parametro Ψ (λ), kuris yra proporcingas paviršiaus plazmonų rezonansu paremtų jutiklių matavimuose. Jutiklio, suformuoto iš „skaldytų”, kryptingai orientuotų antikūnų signalas buvo kokybiškesnis nei sluoksnio, suformuoto iš „neskaldytų”, nekryptingai orientuotų antikūnų.

4. **Skyrius. Antigeno – antikūno sąveikos kinetikos tyrimas visiško vidaus atspindžio elipsometrija [2*].** Optinis elipsometrinių parametrų atsakas parodė, kad parametrų jautrumas skiriasi priklausomai nuo monosluoksnio formavimosi stadijos. Parametras Δ didesnį jautrumą rodo pradinėje reakcijos stadijoje, Ψ – galinėje. Tai turi būti įskaityta aprašant sąveikos kinetikas, išmatuotas visiško vidaus atspindžio elipsometrija. Taikant apibendrintą Longmiuro lygtį, buvo nustatyta, kad negrįžtamos imobilizacijos efektas yra reikšmingas (1) „skaldytų“ ir „neskaldytų” antikūnų afiniškumo konstantų nustatymui; (2) antikūnų sąveikos su antigenu tyrimui. „Skaldytų” antikūnų imobilizacijos ant aukso atveju, negrįžtamos imobilizacijo laikas *t* buvo trumpesnis, negu „neskaldytų” antikūnų imobilizacijos ant 11-MUR savitvarkio monosluoksnio. Negrįžtamos imobilizacijos laikas antigeno sąveikos su „skaldytais” antikūnais atveju buvo ilgesnis, negu su „neskaldytais”.
5. **Receptoriaus-ligando sąveikos tyrimas *in-situ* visiško vidaus atspindžio elipsometrija [3*].** Panaudojant spektroskopinės elipsometrijos, sustiprintos paviršiaus plazmonų rezonasu, metodą buvo tiriama receptoriaus-ligando sąveikos kinetika bangų ruože nuo 300 nm iki 1000 nm. Duomenys buvo

analizuojami taikant daugiasluoksnį optinį modelį. Buvo pademonstruota galimybė, taikant spektroskopinės elipsometrijos, sustiprintos paviršiaus plazmonų rezonansu, tyrinėti monomerinio (mGKSF) ir dimerinio (dGKSF) granuliocitų kolonijas stimuliuojančio faktoriaus sąveikos su receptoriumi (GKSF-R), kinetiką. Spektroskopinės elipsometrijos, sustiprintos paviršiaus plazmonų rezonansu, metodas gali išskirti nežymius skirtumus tarp asociacijos ir disociacijos laiko, dėl tikslaus lūžio rodiklio nustatymo galimybės ir signalo netiesiškumo įvertinimo. Šie mGKSF ir dGKSF lūžio rodiklio skirtumai leidžia taikyti įvairius kinetinius modelius, reikalingus parodyti skirtumus tarp panašių molekulių sąveikos mechanizmų su receptoriumi. Skirtumai tarp monomerinio ir dimerinio GKSF rodo skirtingus reakcijos mechanizmus. Nustatant afiniškumo konstantas mGKSF kinetika buvo analizuojama taikant standartinę Longmiuro lygtį o dGKSF kinetika − taikant apibendrintą Longmiuro lygtį. Afiniškumo konstantos K_a reikšmė monomerinio GKSF atveju ($K_a = 5.6\times10^6$ M^{-1}), charakerizuoja tiesioginę asociaciją ant paviršiaus, tuo tarpu dimerinio dGKSF atveju ($K_a = 1.9\times10^7$ M^{-1}) − vienos dimero dalies asociacija. Koeficientas k_r parodo antros dimero dalies sąveikos su receptoriumi spartą.

6. **Nanolaminatų, sudarytų iš Al_2O_3/ZnO, pagamintų ASN metodu, optinių savybių tyrimas [5*].** Šiame skyriuje aprašomi nanolaminatų optinio pralaidumo, spektrinės elipsometrijos, fotoliumescensijos optiniai tyrimai. Nanolaminatų iš Al_2O_3/ZnO pralaidumo spektrai parodė, kad visi tirti bandiniai buvo skaidrūs nuo 550 nm iki 1100 nm. Sugerties kraštas buvo stebimas nuo 370 nm iki 410 nm bangų ruože. “Mėlynasis” šio krašto poslinkis buvo stebimas mažėjant nanolaminato bisluoksnio storiui. Draustinės juostos vertės buvo apskaičiuotos darant prielaidą, kad Al_2O_3 buvo skaidrus visame spektro ruože, o sugerties kraštas buvo stebimas dėl ZnO sluoksnių. Panaudojant spektrinę elipsometriją buvo nustatyta, kad Al_2O_3 buvo skaidrus visame UV ir regimosios šviesos spektro ruože, o ZnO sluoksnis turi sugerties smailę spektro ruože nuo 360 iki 410 nm. Nustatyta, kad vidutinė ZnO sluoksnio lūžio

rodiklio vertė nanolaminate buvo didesnė negu atskirai auginto sluoksnio. „Mėlynasis“ smailės poslinkis lūžio rodiklio dispersijos kreivėse buvo stebimas mažėjant ZnO sluoksnio storiui nanolaminatuose ir sutapo su informacija, gauta iš pralaidumo matavimų. Nanolaminatų fotoliuminescencijos spektruose, parodytos UV ir regimosios šviesos emisijos juostos ZnO nanostruktūrose. UV smailė atitinka eksitoninius perėjimus, o regimojo spektro smailė atitinka defektų lygmenį. UV smailės intensyvumas išauga didėjant bisluoksnio storiui nanolaminatuose, tačiau regimosios srities smailė elgiasi kitaip.

Apibendrinimas ir galutinės išvados. Pateikiamas rezultatų apibendrinimas ir bendros išvados.

Literatūros sąrašas. Pateikiami kitų autorių darbai, kuriais buvo remtasi, rengiant disertacinį darbą.